UNIVERSITAT POLITÈCNICA DE CATALUNYA BARCELONATECH

Multiscale techniques in turbulence: application to geophysical fluids and operational oceanography

Verónica U. Nieves Calatrava

MULTISCALE TECHNIQUES IN TURBULENCE: APPLICATION TO GEOPHYSICAL FLUIDS AND OPERATIONAL OCEANOGRAPHY

Verónica U. Nieves Calatrava - 2008

UNIVERSITAT POLITÈCNICA
DE CATALUNYA

INSTITUT DE CIÈNCIES
DEL MAR DE BARCELONA
(C.S.I.C.)

APPLIED PHYSICS PROGRAM

MULTISCALE TECHNIQUES IN TURBULENCE: APPLICATION TO GEOPHYSICAL FLUIDS AND OPERATIONAL OCEANOGRAPHY

Verónica U. Nieves Calatrava

Thesis report for the European Doctor Degree, Applied Physics specialization, Universitat Politècnica de Catalunya, under the supervision of Dr. Antonio Turiel Martínez, Institut de Ciències del Mar (C.S.I.C.).

Barcelona, 2008

UNIVERSITAT POLITÈCNICA
DE CATALUNYA
BARCELONATECH

A petició de l'autora, i amb l'autorització de l'Escola de Doctorat, hom retira les pàgines d'agraïments

At the request of the author, and with the permission of the Doctoral School, the acknowledgments have been removed

Maig 2020

Ibergekumene tsores iz gut tsu dertseylin.
Troubles overcome are good to tell.
Yiddish proverb

Contents

CHAPTER 1

Introduction

Turbulent flows are of major interest for scientists and engineers, playing an essential role in fluid dynamics. Even though a precise definition of turbulence does not exist, it is generally assumed that turbulence is a flow regime characterized by instabilities at large Reynolds numbers. The *Reynolds number* is a measure of the ratio of inertial forces to viscous forces. In the ocean, Reynolds number are of the order of 10^6, and so *ocean dynamics is strongly nonlinear involving a large spectra of processes* across all space and time scales. However, the ocean seems to be very active at around 30-300 Km, which is known as *mesoscale*. A schematic diagram of the spatial and temporal scales of various oceanic phenomena is shown in Figure 1.1.

Instabilities in the ocean explain the meandering nature of oceanic currents, which can isolate and shed *eddies* when the meanders reach large amplitudes [3]. Examples of such flows are high- and low-pressure systems that are formed in the Gulf Stream area (see Figure 1.2). These systems have been related to *coherent structures*, which are a combination of the geometrical and dynamical properties of the flow, i.e., regions containing most of the surviving vorticity [56, 47]. As it occurs in the ocean, a turbulent flow self-organizes into a collection of coherent structures [91, 140]. The smaller eddies are exposed to the strain-rate field of these coherent structures [123]. In recent studies, coherent structures not only have been identified with *vortices*, but also their presence has been connected with *non-Gaussian Probability Density Functions* (PDFs) of velocity fields from the ocean [17, 40, 54, 51, 139]. In addition to this characteristic, a near Gaussian component is expected for the background flow. These statistical distributions of ocean velocity fields have similar characteristics to the ones of numerical simulations of *bidimensional turbulence*.

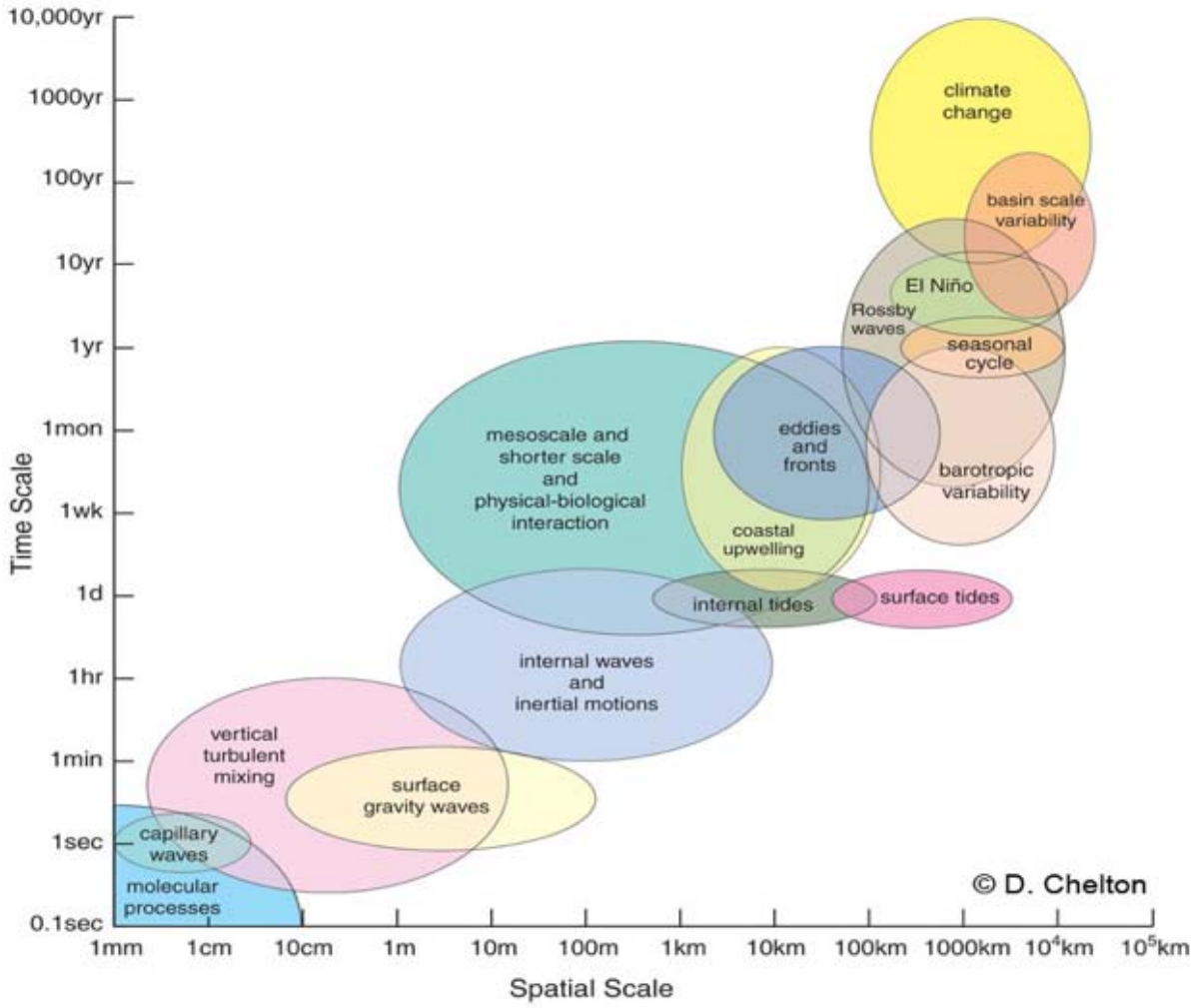

Fig. 1.1: Physical processes vary over a continuum of space and time scales [21].

In general, dynamics of geophysical flows at mid-latitudes and at mesoscale fits well in the *quasi-geostrophic approximation* [111]: horizontal motions are in balance with the pressure gradient force. As soon as the horizontal extension of the motion reaches few kilometers, oceanic turbulence can be considered nearly bidimensional. Under these circumstances, two processes related to the flow energy and enstrophy can take place: the *enstrophy cascade process* and the *inverse energy cascade*. Both of them explain the presence and the long-lived character of the observed coherent structures. *Energy* is the eddy kinetic energy, and *enstrophy* is a quantity expressed in terms of flow vorticity that gives an idea about the tendency of the system to maintain the maximum number of vortices. This kind of "rotational energy" is observed to remain locked in mesoscale scales of oceanic flows, where eddies are very active, and it is relatively immune from the smaller scales [108]. However, for a large Reynolds number the enstrophy decreases through the

dissipation of vorticity filaments that are generated by close interaction of eddies. These filaments are stretched to ever-smaller scales, until they reach scales small enough to be affected by viscosity. In fact, *turbulent flows are always dissipative* [11, 123], and eddies encompass a wide range of scales: from centimeters, where molecular viscosity mainly contributes dissipating energy, to kilometers. As a result of vortex-stretching mechanism and viscous dissipation of energy, there are energy transfers between all motion length scales. The complete process is known as enstrophy cascade process, which has been important in the conceptual development of turbulence [37]. Analogously, there exists also an inverse energy cascade that drives energy from smaller scales toward larger scales. Nevertheless, the inverse cascade in the ocean becomes ineffective beyond a length scale called Rhines scale, which is at most about hundreds of kilometers.

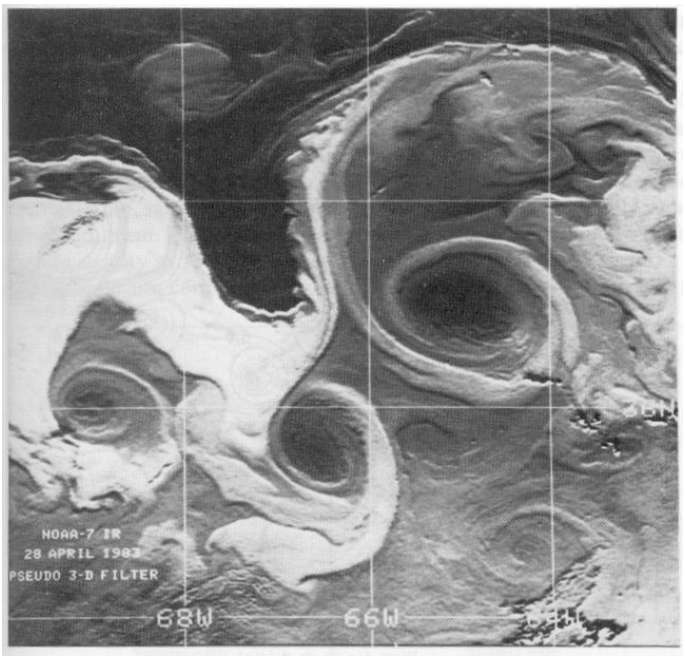

Fig. 1.2: Infrared satellite picture from Gulf Stream (NOAA). Meandering activity and well defined eddies are visible. The size of the domain is about 600 km square. Image from [3].

Understanding how inertial forces tend to produce random eddies and other velocity fluctuations is fundamental in oceanography. Many studies of physical-biological interaction are associated with coherent structures in the open ocean and coastal regions. Due to their long lifetimes and spatial extent, coherent structures strongly influence the exchange of heat, nutrients, etc. between different locations and scales. Traditionally in turbulence, the evolution of the combined effect of ocean stratification and Earth rotation has been assessed by the Navier-Stokes equations or Direct Numerical Simulation (DNS). All spatio-temporal scales of a turbulent flow are resolved without averaging or approximating; the main errors come from numerical discretization. In the ocean, this idea is as easy in theory as an extremely tough task in practice due to the com-

putational cost involved. In view of the computational needs that exceed the current super-computational architectures, oceanic turbulence cannot be exclusively described from computational predictions. The *combination of experimental data together with mathematical models* is convenient to deal with such a complex problem. Based on this idea, turbulence can also be faced through semi-deterministic methods, e.g., Unsteady Reynolds Averaged Navier-Stokes equations (URANS) or Large Eddy Simulation (LES). These methods rely on the observation that, from all spatio-temporal range of scales existing in a turbulent flow, great scales are the most effective in the transport of properties, while small scales are weaker. In spite of this, this kind of simulation is still very demanding regarding computational resources and calculation time.

There are other strategies that adopt the same core concept as URANS or LES. They are based either on (i) the statistical properties of the *velocity fluctuations* or on (ii) the idea of a system of interacting *coherent structures*. Both methods also suggests some sort of filtering operation that would low-pass the equations of interest and suppress the higher frequency motions - lower frequency variability in the sea [101, 3]. The success of a low-pass filtering procedure depends in part on the existence of a "spectral gap" in the energy spectrum. This concept is illustrated in Figure 1.3.

In the spatial Fourier decomposition, a signal f depending on the space $\vec{x}$ is smoothed at the length scale of $l = K^{-1}$, i.e., scale of the filtering, in the following way:

$$f(\vec{x}) \;=\; f_K^{<}(\vec{x}) \;+\; f_K^{>}(\vec{x}) \tag{1.1}$$

with $f_K^{<}(\vec{x}) \;\equiv\; \sum_{k \leq K} \hat{f}_k \, e^{\,i\,\vec{k}\,.\,\vec{x}}$ and $f_K^{>}(\vec{x}) \;\equiv\; \sum_{k > K} \hat{f}_k \, e^{\,i\,\vec{k}\,.\,\vec{x}}$.

The (spatial) *energy spectrum* is defined by using the same concept, where the signal is a random velocity field $\vec{v}$ and $v_K^{<}$ the low-pass filtered velocity field - containing information at a wave number less or equal to K:

$$E(k) \;\equiv\; \frac{d}{dk}\,\epsilon(k) \tag{1.2}$$

where $\epsilon(K) \;\equiv\; \frac{1}{2}\,\langle [v_K^{<}(\vec{x})]^2 \rangle$

It is important to keep in mind that a certain eddy size l is related to a certain wave number k. Each eddy can be understood as some disturbance containing energy in the vicinity of k. However, eddies cannot be thought as identities due to the interactions with each other. An eddy is associated to many Fourier coefficients. Therefore, the contribution of an eddy to the spectrum is a broad spike. Moreover, the basis functions

of a Fourier transform are localized in wave number space, but not in the physical space. Thus, more sophisticated transforms such as wavelet transforms are needed to decompose the velocity field. The coefficients of the wavelet transform allow tracking the size and location of features of a signal, e.g., intense vortices.

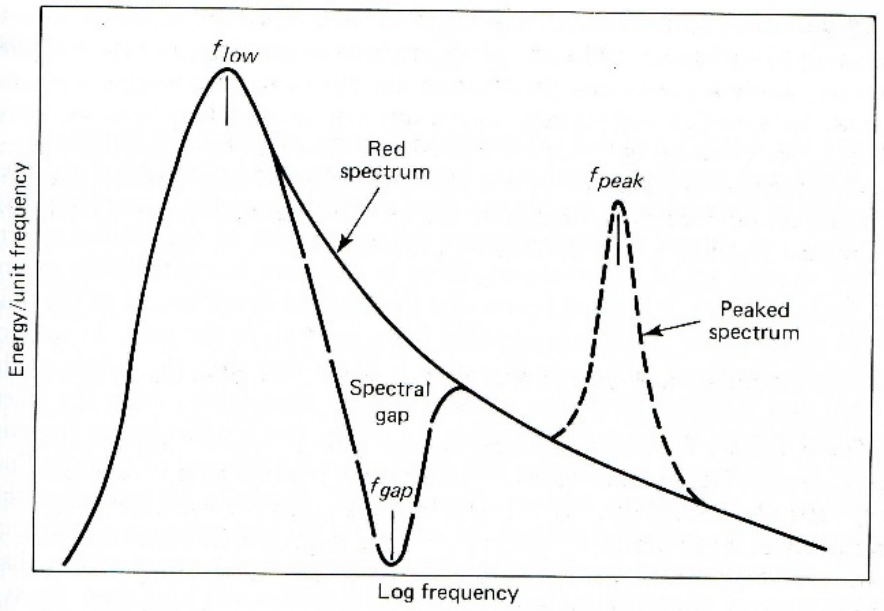

Fig. 1.3: Three types of energy spectra for oceanic motions [3]. Solid line: typical "red" spectrum showing monotonic increase toward lower frequencies up to the spectral maximum at f_{low}. Dashed line: spectrum showing a gap at f_{gap}, which divides slow from fast motions. Dotted line: spectrum showing a peak response at f_{peak}, characterizing narrowband processes such as tides and swell.

Some filtering-based models and techniques are shortly reviewed next:

i) The statistical branch was initially introduced in 1941 by Kolmogorov and settled the foundations of the modern *theory of turbulence* [62, 61]. This approach makes use of probabilistic tools to decompose a turbulent flow into mean, and fluctuating quantities. The fluctuating part is represented by velocity increments $\delta v(\vec{x}, \vec{l}) \equiv v(\vec{x}) - v(\vec{x} + \vec{l})$. Kolmogorov found that the moments of the velocity increments at *the smallest scales are universal*, i.e., independent of the particular flow under consideration. This theory implied far-reaching consequences, but their predictions were not observed until many years later, e.g., [65]. In fact, the scaling properties of these rapidly varying portions of a turbulent flow could not be analyzed locally until recent years at mesoscale. *Singularity Analysis* (SA) is a novel technique that encourages the local analysis of turbulent flows by detecting spatial transitions in velocity or any advected passive scalar field [132, 129]. *Advection* refers to the

transport of some property of the ocean, e.g., sea surface temperature, submitted to the velocity field. The key difference between SA and Kolmogorov's theory is that these quantities (and hence flow dynamics) can be now estimated point-by-point. In addition, SA track transitions independent of their amplitude, so even subtle structures can be detected. Notice that *one of the long-standing challenges in oceanography is an accurate estimation of the velocity field*. For the first time, instantaneous fields of sea surface currents have been recently inferred, e.g., from satellite scalar variables, by using SA [132, 129]. In the ocean, however, SA-derived maps had not been validated, and this was one purpose of my research.

ii) *Coherent Vortex Extraction* (CVE) is a technique that selects *the most dynamically relevant structures* from the vorticity field [33, 35, 34, 13, 128]. Similar to the traditional picture, CVE uses spectral analysis of the turbulent motion, but supported by a refined multiscale (*local wavelet-based*) method. Wavelets bases are local and so the spatial localization of vortices does not become uncertain. Furthermore, wavelets allow to represent complex signals without fixing the observation scale [83]. CVE role lies on a flow patterns description considering vortices as the dominant part of flow evolution, which correspond to only few degrees of freedom. The vorticity field is partitioned into two parts: the self-structured component (coherent part), and the background energy (incoherent part). The first is characterized by the greatest amplitudes; the second is the remaining flow. However, the inhomogeneous character of ocean turbulence is not contemplated, e.g., the contribution due to the interaction of structures is neglected. Thus, CVE deserved improvement particularly on satellite data. Further research within my PhD shed light on this issue.

1.1 My research

SA and CVE techniques, and different kinds of satellite products were employed to carry out five studies that are reported herein. All of them have been developed through the multifractal properties of oceanic flows.

The use of satellite data was motivated by the fact that remote detection has contributed to the acquisition of oceanographic information in a greater scope than in-situ observations. Field measurements require a costly effort because of the technology sometimes needed, e.g., instruments specially designed with particular materials for specific purposes. An intrinsic-yet-costly difficulty is the maintenance of a ship in an operative way and the crew support. Additionally, in-situ sampling is scarce and spatio-temporal disperse; yet it is the most precise. On the contrary, satellite data offers a synoptic view of extensive areas with high temporal reiteration despite the initial cost that the sen-

sor design, construction and launching involve. However, satellite data are exclusively limited to the sea surface, and there are many physical processes that occur on spatial scales that are not fully resolved by the satellite sensors. Even so, it has been possible to prove straightforwardly the existence of eddies and other structures from almost global coverage images, instead of inferring them from incomplete and non-simultaneous field measurements. The long data record provides the first opportunity for operational applications to predict mesoscale ocean circulation.

During my research SA has been applied to satellite images with the aim to provide a new perspective of mesoscale ocean dynamics, and a verification of the existence of a cascade process. According to theory [1, 129], it is known that the scaling properties (scaling exponents) of spatial differences of a given magnitude, e.g., satellite-derived scalars, are related to relevant dynamical information. Each value of singularity exponent should be associated to a group of streamlines, as singularity manifolds are dragged by the flow [55]. It has been shown that singularity fields provide a detailed description of the global oceanic circulation scheme. This is under the assumption of strong advection, although this does not need to be the most important effect. Two key points needed further investigation, and both of them have been analyzed in the course of my PhD:

- Validation of streamlines with geostrophic velocity fields derived from altimetry.
- Comparison of singularity maps derived from different satellite data.

Another major development of my research concerns an improved procedure for CVE [128]. The standard criterion threshold that was used in CVE to separate a flow into coherent and incoherent parts is based on its global properties [27]. However, the particularities of the flow at each point have to be considered because they contain an important part of the most energetic structures needed to describe ocean dynamics. Throughout my work CVE has been modified after demonstrating various aspects of the linkages between the different scales of satellite information and hence of oceanography, i.e., the cascade process in ocean turbulence:

- Introduction of the multifractal properties of satellite variables in an iterative procedure on CVE by means of a cascade-based description.

This research led to the following publications (see Chapters 2-6 or [136, 137, 131, 98, 99]):

i) Tracking oceanic currents by singularity analysis of MicroWave Sea Surface Temperature images.

ii) Obtaining and monitoring of global oceanic circulation patterns by multifractal analysis of MicroWave Sea Surface Temperature images.

iii) Técnicas multifractales para la extracción de la función de corriente a partir de imágenes de la superficie del mar.

iv) Common turbulent signature in sea surface temperature and chlorophyll maps.

v) Analysis of ocean turbulence using adaptive CVE on altimetry maps.

In Chapter 7, a discussion is included. Conclusions are detailed in Chapter 8.

1.2 Materials and methods

1.2.1 Kolmogorov's theory and MMF

Kolmogorov found that the hydrodynamic equations for incompressible fluids show a scaling symmetry at infinite Reynolds number [62, 61]. Kolmogorov also defined a range of scales for which this symmetry is valid: the inertial range. The symmetry is not conserved for large scales where turbulence is generated and for dissipative scales where molecular viscosity is important.

In this framework, turbulent flows are analyzed using its statistical moments S_p given by

$$S_p(l) \;=\; \langle \epsilon_l^p \rangle \tag{1.3}$$

Typical choices for ϵ_l are linear increments of the modulus of the velocity along a given direction, $\epsilon_l(\vec{x}) \;=\; |v(\vec{x}) - v(\vec{x}+\vec{l})|$ or local energy dissipation on balls of radius l, $\epsilon_l(\vec{x}) \;=\; \sum_{ij} \int_{B_l(\vec{x})} d\vec{x} \;\; (\partial_i v_j(\vec{x}\,) \;+\; \partial_j v_i(\vec{x}\,))^2$.

In the inertial range, the statistical moments are scale invariant with respect to the scale scope l at any order p. This is manifested in a power-law scaling function:

$$S_p(l) \;\propto\; l^{\tau_p} \quad ; \quad l \ll 1 \tag{1.4}$$

where $\tau_p \;=\; H\,p \;+\; \beta$, H and β coefficients derived from ϵ_l properties.

Kolmogorov gave the first theoretical explanation that supports such a statistical formalism - also referred to as Canonical Multifractal Formalism (CMF) [138] - to explain the concept of an injection mechanism for Fully Developed Turbulence (FDT). Nevertheless, it is known that the linear scaling predicted by Kolmogorov is not accomplished experimentally. Experimental results show "anomalous scaling" for τ_p [2, 105, 6]. This phenomenon is related to strong fluctuations of the energy flow in the cascade, i.e., energy dissipation is intermittent.

The first to propose an explanation for dissipation-range intermittency was Kraichnan [64]. He showed that fluctuations are tremendously amplified in the dissipation range. He also stressed that dissipation-range intermittency does not imply inconsistency with $K41$. Other attempts to properly fit intermittency within turbulence were made by Mandelbrot from 1968 on [84]. According to his model (*the β-model*), with each step in the cascade process the eddies become less and less space filling in a scale-invariat fashion. Mandelbrot defined such basic structures with self-similar properties as fractals, as they only occupy a fraction of the total volume (fractal Hausdorff dimension) [85]: "A fractal is a shape made of parts similar to the whole in some way". This means that in nature several objects are composed of parts that look like the whole, see Figure 1.4. This model led Parisi & Frisch to find that there are multiple fractal components with different dimensions: *the multifractal model* in terms of velocity increments [105]. Multifractality was also defined in terms of fluctuations of the local energy dissipation based on Obukhov's and Kolmogorov's contributions in 1962 [102, 63]. With these reformulations the idea of a *multiplicative cascade* was introduced to explain this complex picture of multiscaling exponents.

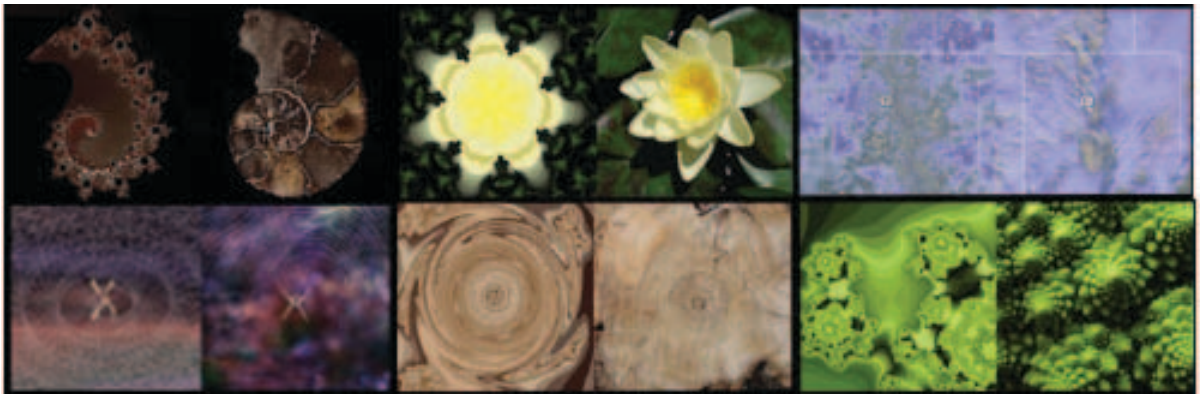

Fig. 1.4: From left to right and from top to bottom: Ammonite, Water Lily, Colorado Snow, Spider Web, Rings of a Cottonwood Tree, and Brassica Oleracea. Image from: http://scienceblogs.com/chaoticutopia/2007/01/friday_fractal_nostalgia.php

The fractal dimension associated to a scaling exponent h is calculated for each statistical moment. Then, the fractal manifold (the set of fractal components) is defined as the Singularity Spectrum (SS):

$$D(h) \;=\; \inf_{p} \{ph \,+\, d \,-\, \tau_p\} \tag{1.5}$$

It has been used that $\rho_l(h) \;\propto\; l^{d-D(h)}$, whose exponent is related to the usual Hölder exponent. $\rho_l(h)$ is the distribution of scaling exponents h at a given scale l, d represents the domain space dimension. Hence $\tau_p \;=\; \inf_{h} \{ph \,+\, d \,-\, D(h)\}$ [32].

SS should correspond to a convex function of h (multiplicative cascade), see Figure 1.5.

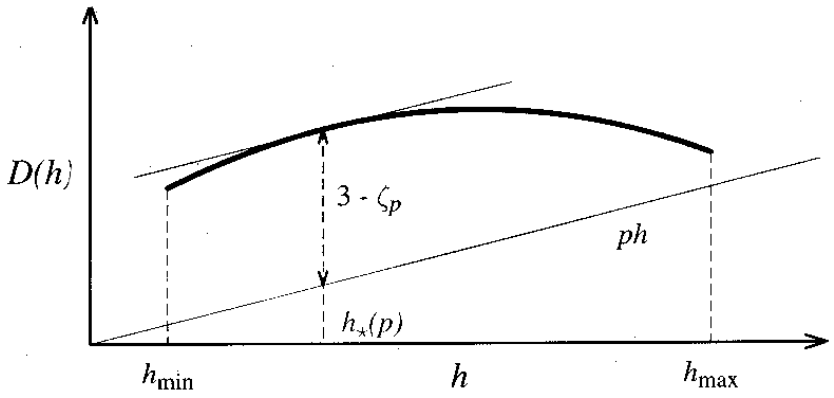

Fig. 1.5: Geometrical construction of the fractal dimensions.

In the recent years it has been shown that the value of the local scaling exponent $h(\vec{x})$ of a given turbulent signal s could be calculated point-by-point $\vec{x}$. Singularity Analysis is a signal processing technique that makes possible this analysis [132, 129]. SA classifies the points in a given turbulent flow according to the value of its local singularity exponent. Singularity exponents are a measure of the degree of regularity or irregularity of the function at each point. Therefore, maps of singularity exponents provide information about the geometrical properties of the flow, which is related to its underlying physics [129, 127, 55]. Examining scaling theory considering the local properties of the flow is also known as Microcanonical Multifractal Formalism (MMF) [138].

Importantly, MMF is a new field of fluid dynamics that complements theory and experimentation to describe turbulent flows. This is possible through the following equation that links the statistical properties of a FDT flow with the geometrical ones:

$$\frac{1}{l}|s(\vec{x}+\vec{l}) - s(\vec{x})| \ \sim \ l^{h(\vec{x})} \tag{1.6}$$

where $h(\vec{x})$ is the local singularity exponent given the field $s(\vec{x})$ at the point $\vec{x}$ and resolution scale l for any vector $\vec{l}$ small enough.

The family of dimensions is again characterized by the multifractal spectrum [5] (Equation (1.5)). However, SS is calculated now from the distribution of the scaling exponents associated to each point $\vec{x}$:

$$D(h) \ = \ d \ - \ \frac{\log\left(\frac{\rho_l(h)}{\max\ \rho_l(h)}\right)}{\log l} \tag{1.7}$$

where d is the signal domain dimension ($d = 2$), $\rho_l(h)$ is the empirical histogram of singularities at scale l.

Three requirements are fundamental to apply MMF:

i) Each fractal component is scale-invariant: for any point $\vec{x}$, Equation (1.6) is verified over a large enough range of scales l.

ii) The whole multi-fractal hierarchy is scale-invariant: the distribution of singularities at any valid scale l follows Equation (1.7), for the same function $D(h)$.

iii) The function $D(h)$ derived from Equation (1.7) is convex.

For an extensive discussion of this topic the reader is referred to [138, 99] and to Chapter 6.

1.2.2 MMF on satellite images

One of the aims of my PhD research was to demonstrate that techniques developed in the frame of MMF like SA could also be applied to satellite images to extract information about ocean dynamics (see Figure 1.6 and [136, 98]). This is based on the idea that the flow agitation state is transmitted to the singularities observed in satellite-derived scalars in such a way that they act as tracers of fluid dynamics [1, 129]. The scaling properties of these scalar variables are more accessible than the ones of the flow. However, satellite data should be first filtered due to the fact that flow long-range correlations can affect the detection of the finest structures. For this reason, a wavelet-based method has been used. Continuous wavelet transforms have been shown to be the most adequate filter for this purpose [23, 83]. Additionally, wavelets preserve scale-invariance and hence they make possible to work with a wide range of scales. Nevertheless, the available range of scales is subjected to the resolution limits of the satellite images.

After applying wavelet transform, the tracer s is represented at the point $\vec{x}$ and scale l as

$$T_\Phi s(\vec{x}, l) \equiv \int d\vec{y}\, s(\vec{y}) \frac{1}{l^d} \Phi\left(\frac{\vec{x}-\vec{y}}{l}\right) \tag{1.8}$$

where Φ is the wavelet basis and d is the domain space dimension.

Hence the wavelet expression equivalent to Equation (1.6) is:

$$T_\Phi s(\vec{x}, l) \sim l^{h(\vec{x})} \tag{1.9}$$

A noteworthy fact is that Equation (1.9) leads to the same singularity exponents as Equation (1.6) [5, 132]. In previous works, however, it was found that Equation (1.9) has some numerical problems that can be solved by computing the modulus of the signal gradient [138]. In this way, the spatial resolution is not reduced, and the new measurable quantity still presents a multifractal behavior [132, 43]:

$$T_\Phi |\nabla s|(\vec{x}, l) \sim l^{h'(\vec{x})} \tag{1.10}$$

The exponents are related in the way: $h(\vec{x}) = h(\vec{x}) - 1$.

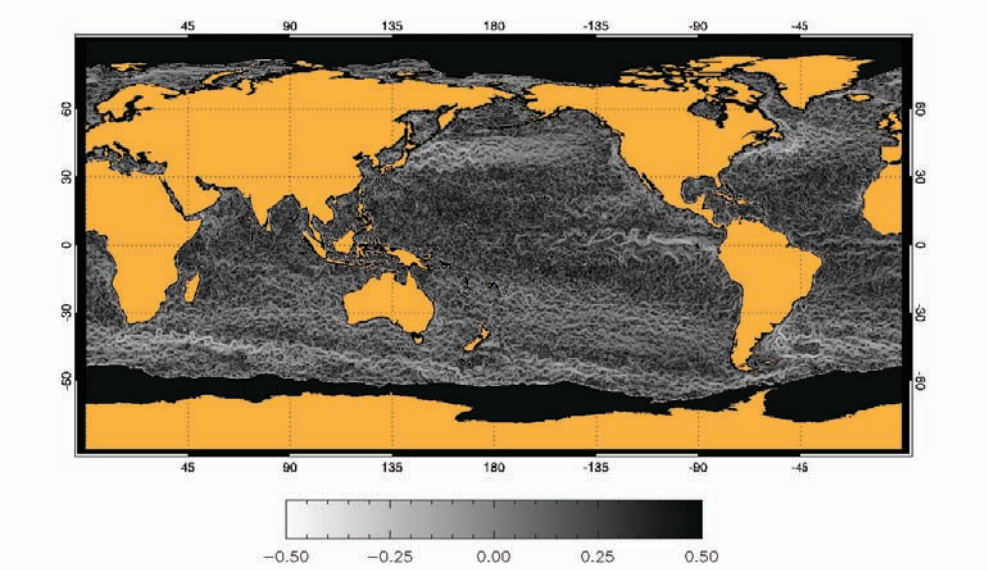

Fig. 1.6: Singularity exponents map associated to a MicroWave Sea Surface Temperature image [136].

Similar results can be obtained by using different wavelets, but not all of them perform equally well on real data. The most appropriate family of wavelets for this kind of problems is the Lorentzian one [125, 138]:

$$\Phi(\vec{x}) \;=\; \frac{1}{1+|\vec{x}|^2} \tag{1.11}$$

In some cases, it is more convenient to obtain punctual estimates of the singularity exponents h at each location on account of the limited resolution of some data and the small size of the studied areas [135, 109]. For this reason, dyadic wavelet basis have also been employed. The discrete wavelet transform has been found to be well suited to analyze intermittent signals and systems containing localized features such as intense structures [35].

The representation of the signal in a dyadic wavelet basis is given by

$$s(\vec{x}) \;=\; \sum_{r=1,2,3} \sum_{j=1}^{J} \sum_{\vec{k}} \alpha_{rj\vec{k}}\, \psi_{rj\vec{k}}(\vec{x}) \tag{1.12}$$

where $\psi_{rj\vec{k}}(\vec{x}) = 2^{-j}\psi_r(2^{-j}\vec{x} - \vec{k})$ are the mother wavelets, r is the mother wavelet orientation, 2^j is the dyadic scale (pixels), $2^j\vec{k}$ represents the spatial location with $\vec{k} = (k_1, k_2)$; and j, k_1, k_2 are integer numbers. Wavelet coefficients are obtained by projection $\alpha_{rj\vec{k}} = \langle \psi_{rj\vec{k}}, s \rangle$ [23].

In this context, Equation (1.7) reads:

$$D_{rj}(h) \;=\; d \;-\; \frac{\log\left(\frac{\rho_{rj}(h)}{\max\ \rho_{rj}(h)}\right)}{(j-J)\log 2} \tag{1.13}$$

with $\rho_{rj}(h)$ as the distribution of singularity exponents $h_{rj\vec{k}}$ for the orientation r and scale j.

The empirical estimate of the distribution of the singularity exponents at any scale can be obtained, and a convex function is expected in all cases. This would validate the hypothesis of a turbulent origin flow driving the satellite-derived scalar and the statistical symmetry prescribed by theory. Even though satellite images are often contaminated, isotropy can be found because of the local character of the singularity exponents.

Once the multifractal character of a scalar variable is verified, some concepts such as the multiplicative cascade process can be used to link the information among the different scales. Under the assumption of turbulent cascading [37], the distribution of singularity exponents derived at a given scale is in equilibrium with the distribution of exponents, as observed at any other scales:

$$\alpha_{rj\vec{k}} \;\doteq\; \eta_{rj\vec{k}}\, \alpha_{r,j+1,\left[\frac{\vec{k}}{2}\right]} \tag{1.14}$$

where $\left[\frac{\vec{k}}{2}\right]$ is the vector with components equal to the integer part of those of $\frac{\vec{k}}{2}$, and $\alpha_{r,j+1,\left[\frac{\vec{k}}{2}\right]}$ are the wavelet coefficients at the immediately coarser scale $j+1$ and about the same position as that of coefficient $\alpha_{rj\vec{k}}$.

Attention must be paid to the fact that this expression can be verified for the wavelets coefficients derived from any scalar, and for any intermediate stage. This implies that kinetic energy and/or enstrophy is distributed in such a way that it guarantees a continuous transfer between larger and smaller scales. This process is analogously valid for both downscaling and upscaling developments.

1.2.3 Coherent Vortex Extraction

In a large number of cases, the best compromise between realistic Reynolds numbers, good resolution of coherent structures, and low computational cost can be reached using a method based on a vortex extraction algorithm - Coherent Vortex Extraction - for calculating two-dimensional turbulent flows [33, 35, 34, 13], i.e. Coherent Vortex Simulation.

CVE analyzes turbulence by only using the most energetic structures from the vorticity field ω. The vorticity field is appropriate to detect areas of strong gradient, which are associated to the nonlinear interactions. In order to select the scales of interest, CVE uses a nonlinear filter - that depends on each flow realization - following a multiresolution analysis: dyadic wavelet transforms of mother wavelets $\{\psi_r\}_{r=1,2,3}$ are applied to the signal $\omega(\vec{x})$.

As in Equation (1.12), the signal is given by

$$\omega(\vec{x}) \;=\; \sum_{r=1,2,3} \sum_{j=1}^{J} \sum_{\vec{k}} \alpha_{rj\vec{k}}\, \psi_{rj\vec{k}}(\vec{x}) \tag{1.15}$$

where $\psi_{rj\vec{k}}(\vec{x}) = 2^{-j}\psi_r(2^{-j}\vec{x} - \vec{k})$, r is the mother wavelet orientation, 2^j is the dyadic scale (pixels), $2^j\vec{k}$ represents the spatial location with $\vec{k} = (k_1, k_2)$; and j, k_1, k_2 are integer numbers. $j = 1$ is the finest scale, and $j = J$ is the coarsest (integral) scale. Wavelet coefficients are obtained by projection $\alpha_{rj\vec{k}} = \langle \psi_{rj\vec{k}}, \omega \rangle$ [23].

The retained structures are selected by using the Donoho & Johnstone's criterion [27], and they are considered as the coherent contribution to the flow ω_c. The remaining flow is associated to the incoherent part ω_i (see Figure 1.7):

$$\omega \;=\; \omega_c \;+\; \omega_i \;=\; \sum_{\alpha_{rj\vec{k}} > \Theta} \alpha_{rj\vec{k}}\, \psi_{rj\vec{k}}(\vec{x}) \;+\; \sum_{\alpha_{rj\vec{k}} \leq \Theta} \alpha_{rj\vec{k}}\, \psi_{rj\vec{k}}(\vec{x}) \tag{1.16}$$

where $\Theta \;=\; 2\sqrt{ZlnN}$, Z the total enstrophy, $Z = \frac{1}{2}\langle \omega, \omega \rangle$, and N is the number of data points at the studied resolution.

This technique has been initially developed to study 2D turbulent flow simulations. Nevertheless, in a real context such as the ocean, a more complex level of physics is needed. Comparing ocean turbulence with 2D turbulence is a subject of intense research

[91, 57, 54]. However, lately it has been shown that CVE applied to altimetry maps needs some additional improvements to describe ocean dynamics [128]. CVE is not able to produce a fully incoherent part, i.e., Gaussianly distributed and spatially incoherent flow. A more efficient design of CVE on experimental data was one of the main points I have been developing during my PhD research (see [99] or Chapter 6).

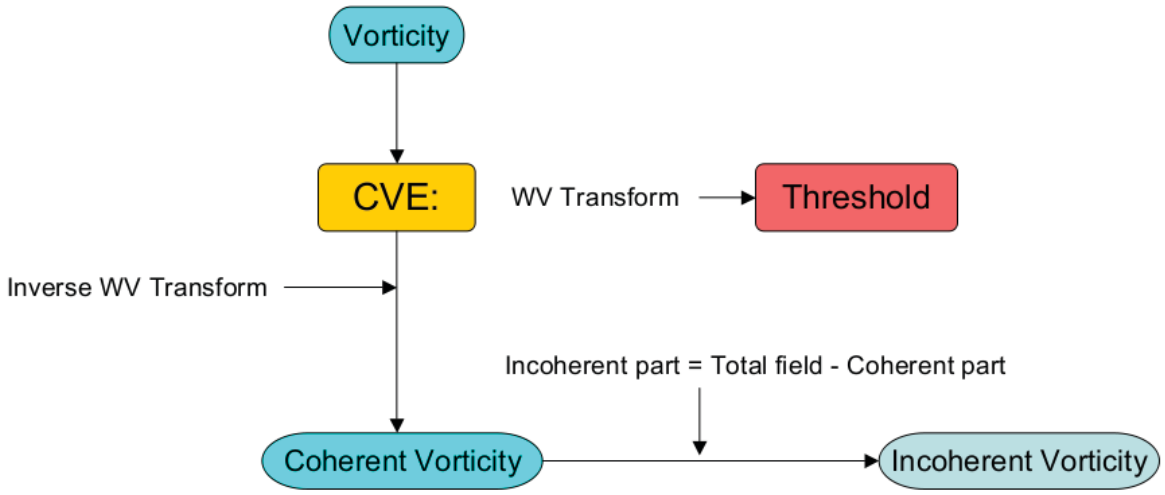

Fig. 1.7: Diagram outlining Coherent Vortex Separation.

1.2.4 Satellite products and their application in oceanography

For the studies developed during my PhD different kinds of satellite data have been used. First, velocity fields derived from Sea Level Anomaly (SLA) maps. Second, Optimally Interpolated (OI) MicroWave Sea Surface Temperature (MWSST) as well as Pathfinder (version 5.0), MODIS Terra L2, and Aqua-MODIS Sea Surface Temperature (SST) data. Finally, Chlorophyll Concentration (CC) images like SeaWiFs and Aqua-MODIS. An accurate description of all products can be found in the next chapters.

Recently, some of the above products have been steadily improved from the needs of understanding the wide variety of Earth system phenomena with better spatio-temporal resolutions. Nowadays space centers generate products that almost fulfill our goals. For instance, SST and CC data have been adapted to fit this new role. These images are not affected by environmental conditions, aerosol corruption, orbital gaps, etc. This has been possible by combining selected satellite images. Thus, these gridded merged products open the way to reanalyze all these data with the applications shown through my PhD research. In the future, how data-merging methods affect oceanic information should be carefully analyzed. Interpolation techniques applied to these data may affect the value

of the singularity exponents. This limitation has to be suitably overcome in order to select only those values that are physically meaningful. Obviously, further significant improvements to these new data will be made through better error specification, and the addition of data from other satellites/sensors. Some examples of integrated data products are described next.

The GlobColour project has been initiated by the ESA to develop a satellite-based ocean colour data service to support global carbon-cycle research and operational oceanography. In this context, a chlorophyll product has been derived from MERIS, MODIS, and SeaWiFS sensors. This product is distributed daily with a nominal resolution of 1/24 degrees (http://www.globcolour.info/products_description.html). Concerning SST, MWSST and OSTIA images are other examples of blended products that offer an improved coverage of global ocean data. MWSST data are obtained from AMSR-E and TMI images, and OSTIA system data from AMSR-E, TMI, Pathfinder, and MODIS images. MWSSTs are updated several times daily in NRT at 25 km resolution. OSTIA images are mainly sponsored by Met Office and ESA, and produced daily at a resolution of 1/20 degrees. For more information http://www.remss.com/sst/microwave_oi_sst_data_description.html, and http://ghrsst-pp.metoffice.com/pages/latest_analysis/ostia.html, respectively.

In Figures 1.8 and 1.9 there are some examples of the mentioned products, i.e., altimetry data, SST, and CC images.

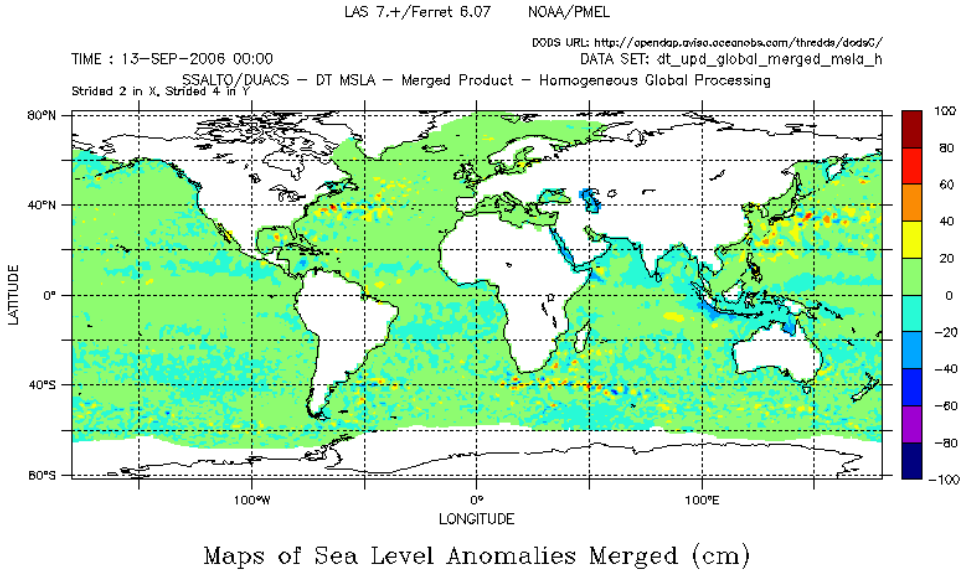

Fig. 1.8: Sea Level Anomalies Topex/Poseidon map, CLS, AVISO server.

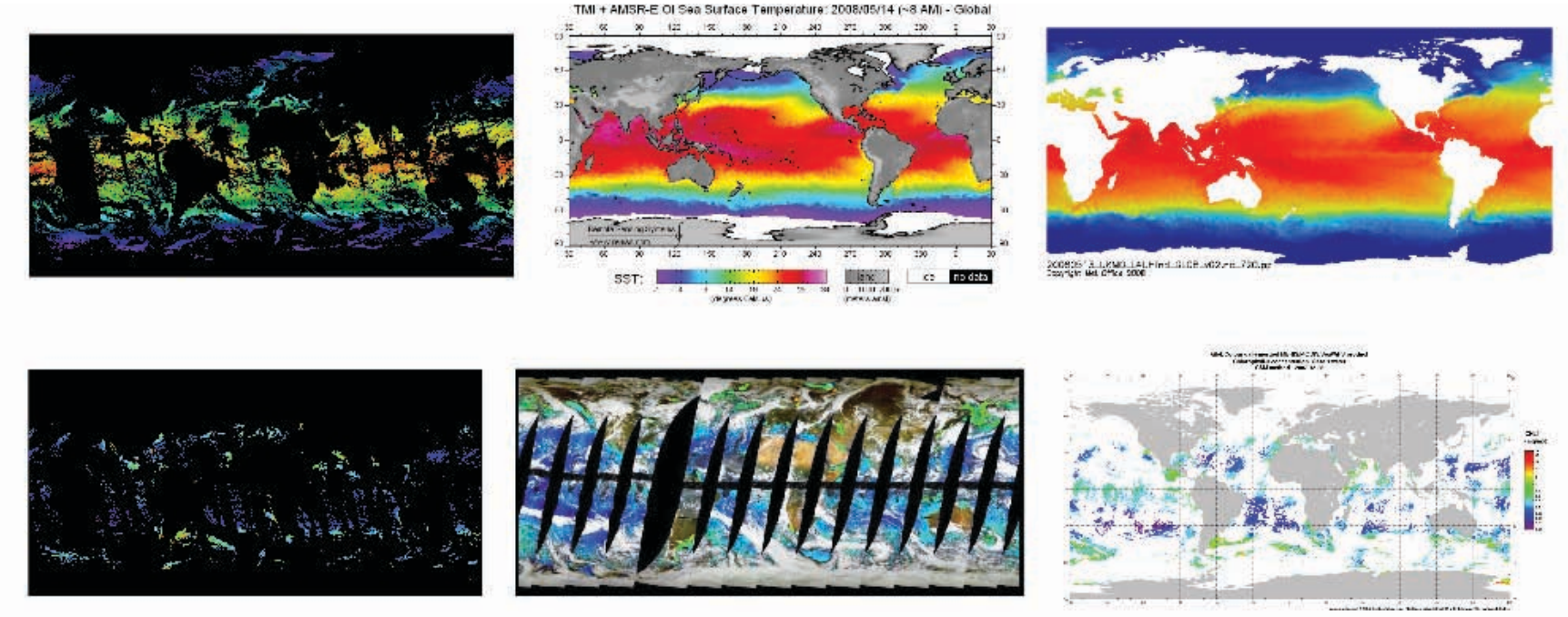

Fig. 1.9: Top: SST products. Bottom: CC data. From left to right: MODIS, MWSST, and OSTIA; MODIS, SeaWiFs, and globcolour images, respectively.

CHAPTER 2

Tracking oceanic currents by singularity analysis of Microwave Sea Surface Temperature images

The difficulty lays not so much in developing new ideas
as in escaping from old ones.
John Maynard Keynes

Tracking oceanic currents by singularity analysis of Microwave Sea Surface Temperature images

ABSTRACT

In the recent years, the power of employing singularity analysis of scalar variables to perform pattern recognition in complex images has been evidenced. This approach is particularly useful when the image under study corresponds to a scalar variable submitted to a turbulent flow because, in that case, the arrangement of singularity manifolds corresponds to the multifractal hierarchy from the underlying turbulent flow. In this paper we will show how this intimate connection between Image Processing and Physics, when applied to Microwave Sea Surface Temperature images, allows to uncover global circulation patterns in the ocean at a daily basis with the resolution of 1/4 of degree. Using this technique, details not evidenced in the non-processed image are revealed. The emerging patterns provide a description of the global oceanic currents much richer than the usual global circulation scheme; in particular, instabilities, eddy generation and filamentation are distinctly identified. A pattern extraction of this kind is useful in order to measure and track mesoscale oceanic phenomena, opening the way to many operational and reanalysis applications.

Published in *Remote Sensing of Environment,* 112 (2008) 2246-2260.

A. Turiel , J. Solé, V. Nieves, J. Ballabrera-Poy, E. García-Ladona

2.1 Introduction

Earth observation satellites are unique measurement devices, offering synoptic information over large areas at an almost constant rate, with unprecedent space and time resolutions. Besides the constraints imposed by data acquisition and processing techniques, current remotely sensed datasets offer an appropriate framework to address the complexity of ocean variability. A typical infrared image shows an ocean surface characterized by the presence of eddies, with diameters ranging from tens to hundreds of kilometers, and filamental structures reaching hundreds of kilometers in length but whose width is of the order of 10 km only, all of them interacting and evolving in time. Such complexity arises from atmosphere forcing, irregular boundaries and from the ocean intrinsic dynamics which, at these scales, is in close resemblance to a fully developed turbulent flow regime.

Statistical studies using satellite datasets have improved our knowledge on the relevant scales and characteristics of ocean properties [24, 121, 89, 26, 71]. Recent studies from altimetry and oceanic float measurements show that the statistical distributions of ocean velocity fields have similar characteristics to that of 2D turbulence, in which vortices and filaments play a major role [17, 40, 54, 139, 53]. Although coherent structures can be easily detected from geometrical properties of the velocity field, the synoptic estimation of sea velocity fields is still a key problem in oceanography. Presently, surface geostrophic horizontal velocities fields may be derived through the combination of several altimeter passes with spatial resolutions of ~ 25 km for mid-latitudes [29]. However, the smallest wavelengths that these maps are able to successfully reproduce are of order 100 km, and this strongly limits the range of phenomena that can be studied. In addition, the temporal resolution of present altimetric products is of about 10 days, which is not adequate to sample some faster oceanic processes (for instance, eddies generated by the instabilities of strong currents).

Higher-resolution, large-area maps provided by infra-red sensors have already been used for estimating velocity fields at finer time and spatial scales. This has lead to the development of different methodologies, as the widely used Maximum Cross Correlation, to infer motion from the relative translation of patterns through sequences of images [31, 38, 124, 49, 58, 22, 25, 16]. The velocity fields obtained from these sequential methodologies can be used to retrieve coherent structures and patterns. However, while the derived velocity fields have some drawbacks (e.g. sophisticated preprocessing and correction, smaller resolution than that of the original infra-red maps), they can sometimes be improved through a previous detection of structures if they are limited by sharp gradients.

A different conceptual approach to the identification of flow patterns from satellite images has recently been issued [129, 55], namely the application of singularity analysis

to SST images. Here, singularity analysis should be understood in a wide sense, as a technique to characterize the scaling properties (scaling exponents) of time or spatial differences of a given magnitude. The roots of singularity analysis lie on the multifractal properties of turbulent flows. It is naturally extended to geophysical flows by the introduction of the Multifractal Microcanonical Formalism (MMF) [132, 109, 55]. According to this formalism, the spectrum of scaling exponents of a given magnitude has a distinguished set of points, the so-called Most Singular Manifold (MSM), straightly connected with the underlying dynamics. In a wider context, the MSM is interpreted as the most informative set, from which the most relevant dynamical properties can be extracted [126, 134].

An interesting application of the MMF, relevant for ocean analysis through remote sensing, rises when the data under study correspond to the values of a tracer submitted to the action of a turbulent flow as, for instance, the SST. Using the appropriate hypotheses [1, 129], the MSM is identified with the dominant streamlines, which can be used to deduce the oceanic motion. Such an approach has been applied to the Pathfinder SST images to deduce the quasi-geostrophic streamfunction [129]. More recently, this approach has been generalized to integrate additional information about the flow dynamics [55]. Furthermore, singularity analysis can be used, in any instance, as an edge detection technique as has been recently demonstrated in the extraction of large-scale coherent ocean wave fronts from Meteosat images, even if this imagery was not specifically designed for ocean observation [130]. In this paper a new forward step is introduced as it is shown that advanced SST datasets can be used to monitor dynamical features using singularity analysis. We will see that this new satellite product, for the scope of this paper named Microwave Sea Surface Temperature (MW SST) imagery, has enough quality to allow tracking circulation patterns across uninterrupted weeks when singularity analysis is applied.

The paper is organized as follows. First, the basics of singularity analysis and the dataset are briefly introduced. Then, we show the results of the singularity analysis applied to microwave images at a global scale and for some selected regions. Finally we conclude summarizing the potential use of the singularity technique applied to MW SST images.

2.2 Singularity analysis

Singularity analysis of scalar variables was introduced in the context of wavelet analysis twenty-five years ago [80]. The goal of singularity analysis is to obtain, at each point of a given image, a dimensionless measure, known as the singularity exponent, of the degree of irregularity at that location. The singularity exponent is a continuous extension of more

classical concepts such as continuity or differentiability. In the classical formulation, the degree of regularity of a signal s at a point $\vec{x}$ is measured by the Hölder exponent, $H(\vec{x})$, of the signal at that point. Roughly speaking, the Hölder exponent is the (not necessarily integer) exponent of a pseudo-Taylor expansion of the function around $\vec{x}$, namely:

$$s(\vec{x}+\vec{r}) - s(\vec{x}) \;\approx\; \alpha(\vec{x}) r^{H(\vec{x})} \quad , \quad r \ll 1 \tag{2.1}$$

for any displacement $\vec{r}$ small enough. Notice that all the dependence on the size r of the displacement (the *scale scope* or *resolution*) is controlled by the power-law defined by the singularity exponent $H(\vec{x})$. A value of $H(\vec{x})$ equal to 1 means that the function is once differentiable; a value of 2 implies double differentiability; a value of 0 means that the function is only continuous. Values between 0 and 1 imply that the function is more regular than a continuous function but it is not so regular to allow differentiation, and so on. Negative values are also possible: they imply some degree of divergence of the function at $\vec{x}$, from simple step discontinuities to divergences up to infinity.

To obtain the singularity exponent from observations is not trivial because the presence of noise and long range correlations that distort the value of the exponent [96, 5, 4]. On the other hand, discretely sampled data must be interpolated on the continuum of scales to give rise to the correct power-law scaling in Equation (2.1) [132]. The use of wavelet projections of the data allows to circumvent both issues [83]. The wavelet projection of the function s on the wavelet Φ at a point $\vec{x}$ and with a scale scope r is defined as:

$$T_\Phi s(\vec{x}, r) \;=\; \int d\vec{y}\, s(\vec{y})\, \frac{1}{r^d} \Phi\left(\frac{\vec{x}-\vec{y}}{r}\right) \tag{2.2}$$

where d is the dimension of the signal domain ($d = 2$ for images, as they are bi-dimensional objects). According to the definition above, a wavelet projection is just the convolution of the signal with a re-sized version of the wavelet Φ, for which the parameter r regulates the actual scope. Notice that wavelet projections are *continuous wavelet transforms* (*i.e.* the point $\vec{x}$ under study and the scale parameter r varies continuously), in opposition to *discrete wavelet transforms* as the ones used in multiresolution analysis (for which Quadrature Mirror Filters as Haar or Daubechies bases are typical examples). Discrete wavelet transforms are used to produce efficient *representations* of discretized data arrays and hence their primary use is for coding. On the contrary, continuous wavelet transforms convey redundant information but are well adapted to detect transitions in the data, and hence their primary use is for *analysis*. Defining an efficient

representation of data is a more exigent task than just assessing some of its properties. Thus, additional constraints are required when wavelets are used for discrete transform coding. In opposition, wavelet analysis can be accomplished with few requirements on the wavelet Φ, and sometimes even positive wavelets (which will not be *admissible* for coding purposes [23]) can be used [132].

From a theoretical point of view, if a function s has a Hölder exponent $H(\vec{x})$ at a given point $\vec{x}$ as in Equation (2.1), and if the wavelet is such that the wavelet transforms of any polynomial of order large enough vanishes, then the wavelet transforms of the function s lead to the same exponent [5], namely:

$$T_\Phi s(\vec{x}, r) \;=\; \bar{\alpha}_\Phi(\vec{x}) r^{H(\vec{x})} \;+\; o\left(r^{H(\vec{x})}\right) \tag{2.3}$$

where the notation $o\left(r^{H(\vec{x})}\right)$ means a term which is negligible compared to $r^{H(\vec{x})}$ when r is small enough. In fact, Equation (2.3) is valid under more general circumstances than Equation (2.1); in particular, it is well adapted to filter long-range correlations and just detecting the local structure [5], to filter noise and to interpolate discretized data to the continuum of scale changes [132]. Hence, wavelet processing allows to extend the concept of Hölder exponent to the more robust one of singularity exponent. As for Hölder exponents, singularity exponents also characterize the regularity of the function at the points under study, but in a more robust (functional) way. Thus, singularity exponents are also dimensionless quantities which can be used to track transitions independent of their amplitude, so even subtle structures can be detected [130]. Wavelet-based singularity analysis of signals has represented an important step forward in the understanding of the structure of real signals of different kinds [81, 80, 82, 96, 8, 59]. However, as discussed in [135], singularity exponents obtained by the direct applications of wavelet projections of signals have a rather rough resolution when applied to real, discretized data (see examples and discussion in [125]). It has been observed that the wavelet projection of the modulus of the gradient leads to a more precise determination of the singularity exponents, with improved spatial resolution [132, 125]. The wavelet projections of the modulus of the signal gradient lead to a similar power-law scaling,

$$T_\Phi |\nabla s|(\vec{x}, r) \;=\; \alpha_\Phi(\vec{x}) r^{h(\vec{x})} \;+\; o\left(r^{h(\vec{x})}\right) \tag{2.4}$$

where the singularity exponents $h(\vec{x})$ can be trivially related with the exponents $H(\vec{x})$ in Equation (2.3): $h(\vec{x}) = H(\vec{x}) - 1$ [132, 59]. In Figure 2.1 we give an sketch of the algorithm employed for the obtaining of singularity exponents from an arbitrary signal.

The use of gradient moduli is naturally driven by the introduction of the MMF. A full discussion on MMF exceeds the scope of the present work and we will just introduce here some concepts useful for this paper (the reader is referred to [132, 125, 55] for an extensive discussion of this topic).

The MMF allows to decompose any signal as a collection of fractal sets (known as fractal components or singularity manifolds) forming a hierarchy. Each singularity manifold is associated to one and only one value of singularity exponent; that is, they are the level sets of the function $h(\vec{x})$. As the function $h(\vec{x})$ is extremely irregular because of the high intermittency of the gradient [100, 132], its level sets are highly irregular and in fact of fractal nature: this is the reason for their second name, "fractal component". The fractal dimensions of the fractal components usually range from dimension 1 associated to the most singular values (which are curve-like) to dimension 2 of smoother, less definite areas, passing through all possible intermediate values. In any instance, the observed dimensions are greater than 1 [132, 129], which is consistent with having fractal components composed by lines. Decomposing a signal as the union of the different fractal components is called a multifractal decomposition of the signal.

In all this paper, the wavelet Φ of choice is a numerical implementation of the Lorentzian wavelet,

$$\Phi(\vec{x}) \;=\; \frac{1}{1+|\vec{x}|^2} \tag{2.5}$$

As discussed in [125], this wavelet leads to a very fine spatial resolution when applied to the gradient modulus, Equation (2.4), although it tends to truncate the largest values. We correct such a truncation by introducing a finite-size numerical implementation of the wavelet (compact support wavelets never truncate singularities, see [125]). In any instance, we will apply Equation (2.4), so the singularity exponents shown in the figures are $h(\vec{x})$.

Concerning the numerical values of $h(\vec{x})$, these are always contained in the theoretical range $(-1, 2)$, as discussed in [129, 55]. The theoretical lower bound -1 is a consequence of working on finite variation signals (see discussions in [125] and in [135]). In other words, singularities below -1 would lead to images having divergences to infinity at some points (which is rather unphysical for a variable as liquid water temperature in the Earth). The theoretical upper bound $+2$ is a consequence of the existence of a theoretical lower bound of -1 and translational invariance, at least for log-Poisson models: for a general lower bound h , the upper bound h_U is $h_U = h - \log(1 - h)$ [132], $h_U(h = -1) \approx 1.7 < 2$. In practise, the singularities contained in the range (-0.5,0.5) represent

more than 90% of the all singularity exponents [129, 55]. We will use the range (-0.5,0.5) for representation purposes in the figures of this paper.

An interesting property of multifractal decomposition has to do with the relevance (in terms of information content) of the detected structures. When wavelets were introduced almost twenty ago, it was soon recognized that the points comprising the largest wavelet amplitude convey the largest part of the total information of the system [83]. In the context of the MMF, there is a distinguished set, the MSM, which plays a similar role. This set is associated to the smallest values of the singularity exponents h (which are typically negative) and comprises the most obvious contours and some other transitions [132]. In addition, an efficient deterministic algorithm for the reconstruction of signals from the values of its gradient on the MSM has been devised [126], so proving that the MSM is the most informative set.

When the signal of interest is a scalar stirred by a turbulent flow, some additional facts must be taken into account. The fractal components have strong links with the dynamics of the underlying processes; in fact, they can be identified with the different stages of energy dissipation in the energy cascade [118]. Besides, it has been shown that the statistical structure of multifractals is not modified by the chaotic stirring of mesoscale surface-ocean flows [1]. It was then proposed that singularities are advected by the flow. This was experimentally verified for the first time by [129], where the MSM obtained from Pathfinder SST images was compared with altimetry data. It was observed that there was a good correspondence between the structures evidenced by the MSM and those given by altimetry, and also that their gradients align, so at least the most singular exponents were advected by the flow. So far there is no theoretical proof stating the conditions on a scalar to have advected singularities. For the context of this paper, we will show some comparisons with independent data from altimetry satellites.

2.3 Description of the data

Our main source of data for this study are Optimally Interpolated (OI) SST images from Microwave (MW) Radiometer SSTs. Microwave OI SST data are produced by Remote Sensing Systems and sponsored by National Oceanographic Partnership Program (NOPP), the NASA Earth Science Physical Oceanography Program, and the NASA REASoN DISCOVER Project. Data are available through the following web site: http://www.remss.com.

As SST images contain irregularly spaced data (in time and space) due to orbital gaps or environmental conditions, an interpolation of the data onto a regularly sampled grid is needed to make up for this missing data. MW SST products accurately resolve some

features that could be missed due to data gaps or weather condition. This is possible by blending TMI and AMSR-E SSTs, providing nearly complete global coverage each day. Near real time OI SST products are created daily, even if no new observations exist. However, the product is 0.25 x 0.25 degree gridded, which is a coarse resolution in comparison with the standard infrared SSTs one. Processing details can be found in [110] and at the following website:

http://www.ssmi.com/sst/microwave_oi_sst_browse.html

In order to compare the results of the singularity analysis technique applied to the MW SST images, infrared images have also been used in this study. Daily Pathfinder SST data version 5.0 have been used; these data can be downloaded from the Physical Oceanography DAAC at JPL (http://podaac.jpl.nasa.gov, product number 216). This dataset is a new reanalysis of the AVHRR data stream developed by the University of Miami's Rosenstiel School of Marine and Atmospheric Science (RSMAS), the NOAA National Oceanographic Data Center (NODC) and NASA's Physical Oceanography Distributed Active Archive Center (PO.DAAC). This reprocessing uses an improved version of the Pathfinder algorithm [60] and processing steps to produce twice-daily global SST and related parameters back to 1985, at a resolution of approximately 4 km, the highest possible for a global AVHRR dataset from NOAA 7, 9, 11, and 14 polar orbiting satellites.

In addition, we have also used MODIS Terra L2 daily and weekly data, downloaded from the Goddard Earth Sciences Distributed Active Archive Center (GES-DAAC,http://daac.gsfc.nasa.gov/MODIS/). In particular, long wavelength (11-12μm) SST product (MOD28L2) that combines brightness temperatures from channels 31 and 32 has been used. No cloud mask was applied in order to have a situation as close as possible to Pathfinder data.

In order to provide a qualitative validation of the currents detected from SST maps, they are compared against altimetry-derived sea surface height maps. Given the direct relation between altimetric data and sea state dynamics, at least in the geostrophic approximation, sea level maps can be used to obtain sea surface velocity fields except at areas too close to the equator. In this study we have used Sea Level Anomaly (SLA) maps produced by Collecte Localisation Satellites (CLS) in Toulouse (France), which combine the signal of *ERS* and *TOPEX/Poseidon* (T/P) altimeters. These maps are processed including usual corrections (sea-state bias, tides, inverse barometer, etc.) and with improved ERS orbits using *TOPEX/Poseidon* as a reference [9, 72]. SLA are regularly produced by subtracting a four-year mean value (1993-1996); this allows to suppress the systematic deviations in the sea level signal due to errors in the determination of the geoid. However, proceeding in such a way the signal of permanent currents is removed from SLA maps. Permanent currents could be taken into account by adding

an accurate estimate of the Mean Dynamic Topography (MDT) to SLA. Nevertheless, available MDTs include important artifacts due to the uncertainties in the mean sea level, specially due to bathimetric features. For that reason, in spite of its limitations we have preferred to work with SLA maps.

Correcting high-frequency biases and subtracting the 4-year mean are not the only processes applied to SLA maps. Prior to the analysis, data are low-pass filtered using a 35 km median filter and a Lanczos filter with a cutoff wavelength of 42 km in order to reduce altimetric noise [70]. The repeat periods for the ERS-1 and T/P are 35 and 10 days respectively, and the cross-tracks distances are 0.7^o and 2.8^o. SLA maps are built for 10-day periods, using an improved space/time objective analysis method, which takes into account long wavelength errors, on a regular grid of 0.2×0.2 degrees [73, 10]. Thus, the use of altimetric data limits the phenomena that can be studied. On one side, the sampling periodicity of altimeters aliases frequencies below 20 days and 70 days in T/P and ERS-1 data respectively. On the other side, satellite track separation and time sampling limits the capability of altimetric maps to observe fast propagating structures or short-lived ones. Furthermore, recently it has been demonstrated that a two-satellite scenario may underestimates an important portion of the signal variance and may deform the shape of some eddies [106]. However, previous studies have demonstrated that sampling characteristics of altimetric maps are able to capture mesoscale variability, including the largest and more energetic eddies [29, 107, 69]. For the purpose of this paper, we have restricted the use of SLA maps to provide a visual assessment of the SST-derived currents.

2.4 Results and Discussion

Figure 2.2 presents a typical global MW SST image. As previously mentioned, singularity analysis aims to determine the spatial distribution of the scaling exponents of a given magnitude. Figure 2.3 shows the singularity analysis of the MW SST image mentioned above. When applied to infrared images, singularity analysis offers new information on the circulation. The singularities reveal a rich structure of filamentary and eddy-like patterns in a detailed way. Although the signature of many physical patterns in areas where strong mesoscale dynamics exist have already been evidenced using infrared SST images [129], with the application of this technique a more detailed picture emerges. Among the revealed mesoscale patterns, the main oceanic currents are clearly identified. Note that the largest singular values of scaling exponents closely map the areas with the highest surface kinetic energy [41]. Thus, the figure highlights the western boundary currents in the north as the Gulf Stream and its spreading over the North Atlantic and the Kuroshio extension over the Pacific. The analysis allows to manifest the rich internal structure of the spreading of these currents, particularly in the case of Kuroshio

extension. The traces of important currents as the Labrador and the Brazil currents are easily seen; the later is clearly apparent at the Malvinas confluence area. The South Tropical Front has a neat signature from the Malvinas to the Agulhas confluence regions and also between South Africa and Australia, with many filaments of singularities. Over the rest it appears as a wide band of dispersed faint filaments. Despite the data mask on MWSST at polar areas, clear signatures of the Antarctic Circumpolar Current (ACC) are still easily identified. The singularity analysis reveals a rich fine structure of multiple fronts, in agreement with the description by [104] on the Southern Ocean. We can distinguish in the singularity image three different regions particularly populated by singularity fronts. First, a band between $40 - 50^oS$ starting south of the Aghulhas retroflection area and extending eastward and southward reaching 50^oS south of Australia. A second band almost conected with the previous one going from south of New Zealand between $50 - 60^oS$, very close to the ice-cover mask. Finally, a very clear frontal line which could be identified with the Subantartic Front (SAF) at the Drake Passage, that finally merges with several frontal lines in the Malvinas confluence area. The rich structure of these bands containning many filamentary structures, associated to highly singular values, is in agreement with the multijet character of the ACC and the patterns reproduced in high resolution numerical simulations of the Southern Ocean [46].

Figures 2.4 and 2.5 display a zoom for the equatorial Pacific $10^oS - 10^oN$ east of the dateline and the area of the Gulf Stream between $90 - 30^oW$ and $10 - 55^oN$ respectively. These are examples of the potential use of the singularity analysis on MW SST images. Both regions are large areas with very noticeable thermal contrast and a major source of mesoscale eddies. The tropical region displays the anticyclonic wave-like patterns characteristic of the Tropical Instability Waves (TIW). The analysis capture both the El Niño and the seasonal cycle modulation of TIW, as well as its characteristic lenghtscales of these instabilities. Figure 2.5 identifies the path of the Gulf Stream with its complex, undulated shape, wave-like instabilities and several eddy-like patterns. The animated sequences of consecutive images (see the associated webpages) are examples of the ability of the method to detect and track mesoscale features worldwide when applied to the appropriate dataset. Until now, numerical modelling has been the best tool for studying the characteristics of the evolution of these structures. However, due to the pervasive effect of the large viscosity required for the stability of coarse simulations, numerical simulations require high-resolution, low-viscosity model configurations.

In a previous application of singularity analysis on infrared images [129, 55], it was argued that according to MMF the results of singularity analysis should be independent of the analyzed tracer, because the patterns are mostly a consequence of the advection by the flow. Figure 2.6 compares four different processed SST products corresponding covering the region at south of Africa between $13.5^o - 39.5^oE$ and $24^o - 46.5^oS$. The thermal signature of the Agulhas Current (AC) flowing southward along the African coast is clearly seen. The temperature contrast between warm waters carried by the

AC are clearly delineated in the AVHRR Pathfinder and daily MODIS images. In the weekly MODIS image and particularly in the MW SST the fronts appear smoothed and the structures are much more diffused mainly as a result of some aliasing in the weekly composite of MODIS and in the interpolation and lower resolution of the MW SST products. In Figure 2.7 we show the corresponding singularity analysis to illustrate that the results presented here are not particular to MW radiometers or an artifact of the processing technique, but reflect the actual dynamics acting on SST.

All four singularity analyses reveal a rich content of continuous frontal and filamentary structures over long distances delineating the trace of the AC until the retroflexion loop around 40^oS and between $15 - 20^oE$. Other subtle filamentary and eddy-like patterns which are not apparent in the original images are revealed. Singularities derived from daily SST images of AVHRR Pathfinder and L2 MODIS show similar results to what was found for the same area in previous works [55]. Although better resolved than those singularities derived from MW SST, IR images are masked at cloud cover regions which contaminate the analysis, as evidenced by the black areas at the southernmost part of both images; and also in the northeast corner where small cloud patterns in the MODIS image appears as a noisy region in the Pathfinder image. This is precisely the main drawback of these kind of images compared with the MW SST product. The problem can be partially circumvented by the use of composite products as MODIS weekly SST images. On such kind of images the most singular values still correspond to the strongest gradients seen in the daily images but the patterns and the distribution of singularity exponents are more blurred (Figure 2.7, bottom left). This is specially evident in the borders of the core of the AC which is less defined and the signal seems to be lost south of 36^oS. Also their geometry and shape have slightly changed in some cases, probably due to the frontal evolution at the week time scale. The greater uniform distribution of singularity exponents is probably a spatial aliasing of the smaller, rapidly evolving thermal features for which seven days is a too long period. In contrast, although MW SST maps are also obtained by temporal interpolation, the interpolation has a more reduced time extent and structures are less blurred.

In spite of the relatively poor resolution of MW SST maps, they seem adequate to detect and track mesoscale and large scale patterns. Although not affected by clouds, the most singular exponents from MW SST images delineate coarser structures than those of the previous images due to the limited resolution of this type of data. Nevertheless, the main features detected in Pathfinder and MODIS daily data are also detected in the MW SST image and, as it was mentioned before, the main drawback with infrared derived SST, i.e. the lack of acquisitions when clouds are present, is avoided and the structures are well defined over the entire image. Notice however that the streamlines delineated by the singularities may sometimes be interrupted because of the interpolation algorithms applied to the MW SST maps (interpolation tends to smooth the field so weakening or even eliminating some more singular values). Besides, due to the reduced resolution

streamlines become quite rough and in some instances seem to cross each other. In fact what happens is that the structures in the MW SST image appear as an averaging or smoothing of those obtained in SST infrared images.

The correspondence between singularity exponents derived from MW SST images and flow streamlines is shown Figures 2.8 and 2.9. We have used SLA maps obtained from AVISO covering the same areas as in Figures 2.5 and 2.7 . As discussed in the description of data, SLA maps have smaller spatial and temporal resolution and are more difficult to interpret, as they do not account for persistent main currents; however, SLA can be used to identify the most intense vortices and eddy-like patterns [52, 94]. As shown in the figures, there is a good correspondence between the most intense vortices in SLA maps and the structures detected by singularity analysis. As expected on both areas the SLA fails to represent adequately the Gulf Stream and the Agulhas currents while the singularity analysis show long coherent filamentary structures delineating their paths. This is evident for the Gulf Stream up to Cape Hatteras where the SLA does not indicate the presence of the current. The same happens for the Aghulhas current along the African coast and its progression to the south until 38^oS, similar to what is found by other authors [14]. Meandering parts are captured in the SLA as a sequence of cyclones and anticyclones, probably due to a temporal aliasing of the strong variability. In contrast, singularity fronts clearly show a well defined and rather continuous structure. In the Aghulhas confluent area it can be clearly seen a meandering structure towards the west, associated to the separation of South Atlantic surface waters and cold subantartic waters. Similar patterns has been detailed described from hydrographic measurements and sequences of satellite images [78, 77] and are better captured in products as MODAS-2D sea surface height fields [14, 15].

On the other hand, an inspection on the areas outside the influence of the main currents show a rather good visual correspondence between the geometry of the singularity fronts and the SLA field. As it can bee seen in the Atlantic image (Figure 2.8) the central part is populated by a rich structure of eddy-like filamentary patterns that are in good correspondence with the sea surface field.

To quantify the degree of similitude between the streamlines delineated by SLA and those derived from singularity analysis is not an easy task: as a matter of fact, we need to compare geometrical sets, not functions. We can nevertheless provide a quantitative measurement of the mutual closeness of the two types of streamlines using a quantity introduced in [129], namely the variance of SLA conditioned by the streamlines derived from the singularity exponents. We explain how to calculate it in the following.

Let us denote by F_{h_0} the level set of the singularity exponent field associated to the value h_0, namely:

$$F_{h_0} \;=\; \{\vec{x} \text{ such that } h(\vec{x}) = h_0\} \tag{2.6}$$

According to our hypothesis, F_{h_0} consists of streamlines. Notice that it is not on itself a streamline in general, but a union of streamlines,

$$F_{h_0} \;=\; \bigcup_{\alpha=1}^{N(h_0)} \mathbf{s}_{h_0}^{\alpha} \tag{2.7}$$

where the different $\mathbf{s}_{h_0}^{\alpha}$ are the singularity streamlines associated to F_{h_0}. We obtain these singularity streamlines by recursively separating the connected components of F_{h_0}. Indeed, the number of connected components $N(h_0)$ in which each level set F_{h_0} is decomposed depends on the value of h_0 and on the particular SST map from which the singularity exponents were derived.

If the streamlines of SLA and those derived from the singularity exponents coincide, the value of SLA on each singularity streamline $\mathbf{s}_{h_0}^{\alpha}$ must be constant. Hence, the variance of SLA along each one of those streamlines, denoted by $V_{h_0}^{\alpha}$, must be zero. We compute $V_{h_0}^{\alpha}$ as follows:

$$V_{h_0}^{\alpha} \;=\; \langle \mathrm{SLA}^2 \rangle_{h_0,\alpha} - \langle \mathrm{SLA} \rangle_{h_0,\alpha}^2 \tag{2.8}$$

where the symbol $\langle \mathrm{SLA}^p \rangle_{h_0,\alpha}$ means to compute the p-moment of SLA considering points on $\mathbf{s}_{h_0}^{\alpha}$ only.

So, we have computed the sum of the variances of SLA along each one of the singularity streamlines, weighting each streamline by the amount of pixels representing it. We call the result the conditional variance of SLA, CV:

$$CV \;=\; \frac{1}{N} \sum_{h_0} \sum_{\alpha}^{N(h_0)} n_{h_0}^{\alpha} V_{h_0}^{\alpha} \tag{2.9}$$

where $n_{h_0}^{\alpha}$ is the number of pixels on the streamline $\mathbf{s}_{h_0}^{\alpha}$ and $N = \sum_{h_0} \sum_{\alpha} n_{h_0}^{\alpha}$, which coincides with the total number of sea pixels in the image as the decomposition is exhaus-

tive. The conditional variance of SLA, CV, is compared to the total (or unconditioned) variance of SLA, V_{SLA}, which is calculated in the standard way. The ratio CV/V_{SLA} gives us an idea about how constant is SLA along the singularity streamlines. Of course, this ratio cannot be smaller than the known error in SLA, which is about 10% [72]; hence $CV/V_{SLA} \geq 0.10$. Taking into account that SLA maps have smaller spatial and time resolutions than those of singularity maps, we will consider that the degree of coincidence between singularity streamlines and SLA streamlines is reasonably good when the ratio is at most of the order of two instrumental errors, namely when $CV/V_{SLA} \leq 0.20$.

For the experiences shown in this work, we have considered the isolines of singularity with an experimental uncertainty $\pm\Delta h$ with $\Delta h = 0.05$ around the reference values of $h_n = -1.0, -0.9, -0.8, \ldots, 2$. We summarize our results in Table 2.1, for different regions and seasons of a single year; we also show two particular examples in Figures 2.8 and 2.9. Experiences show that conditional variance of SLA is between the 10% and the 20% of the total (unconditioned) SLA variance in all the examples we have calculated it. This indicates a reasonable correspondence between the streamlines given by the two types of maps.

2.5 Conclusion

In this paper it has been shown that the use of advanced image processing tools as wavelet singularity analysis allows to characterize the oceanic circulation patterns from Microwave Sea Surface Temperature (MW SST) images. Singularity analysis assigns a singularity exponent to each point in the image, which is a measure of the local degree of regularity or irregularity of the image at that point. Singularity exponents are dimensionless quantities which can be used to track transitions independent of their amplitude, so even subtle structures can be detected, while areas with large gradients but with slow spatial variation are not considered as singular. Due to their impact in the three dimensional structure of oceanic waters, the possibility of precisely determining the position of oceanic fronts is of the highest relevance [36]. Furthermore the analysis does not depend on the sensor, only on its resolution, accuracy and/or representativity. In this sense singularity analysis acts as a powerful tool as a frontal detector being much more objective than other proposed alternatives [116, 117, 122, 74].

Because singularities are induced by the dynamics of the underlying turbulent flow, they must be in equilibrium with it and so they are passively advected. Singularity manifolds are dragged by the flow so they delineate its streamlines at each time instant; for that reason, this technique allows to detect the main currents which are not always well reproduced by altimeter maps. Hence, singularity manifolds can be used to recognize the streamlines of main oceanic flows, so complementing other dynamic information.

Certainly, singularity analysis does not furnish a valid estimation on the velocity modulus or the flow sense, but the flow direction at each point is known with precision. Combined with some extra information (from different sensors, *in situ* data, other tracking methods or some geographical knowledge) singularity analysis has the potential of furnishing detailed velocity maps for the ocean surface. Although some attempts to reconstruct a streamfunction from singularity analysis of infrared images has already been proposed [129, 55], the results here presented show that MW SST images are ideal for the purposes of unveiling ocean streamlines at global scale: they are acquired almost weather-independently and in a daily basis, which is an appropriate acquisition rate to describe oceanic circulation at the mesoscale.

The potential of microwave SST images for operational purposes has recently been recognized, using a different approach, the Surface Quasi Geostrophy (SQG) theory [48]. According to SQG, the 3D streamfunction vector $\vec{\Psi}$ can be well approximated, at least on some regions and under appropriate conditions [114, 115], by a dominant mode obtained after assuming constant stratification and vanishing relative potential vorticity at surface. In spite of the coarse simplification, SQG velocity fields derived from microwave SST images have been shown to acceptably describe the surface velocity field (as derived from altimetry maps), at least over open-sea areas and for regions with strong SST gradients [51]. The present work shows that, under more relaxed, self-consistently verifiable conditions we could correctly describe surface streamlines at almost any location and time. Hence, a pre-processing of SST data with singularity analysis could probably help to improve the SQG streamfunction and extend its range of validity. The only objection to MW SST images is their relatively poor resolution (1/4 degree for the Level 2 dataset that we have employed in our study). Thus information obtained with singularity analysis can be of further potential use for operational purposes as data assimilation in ocean circulation models.

Singularity exponents can probably be connected with other methods employed in the characterization of ocean dynamics, as finite-size and finite-time Lyapunov exponents [139, 39]. Both types of exponents have many differences. Lyapunov exponents have dimensions (inverse of time) while singularity exponents are dimensionless. To obtain Lyapunov exponents the velocity field must be known, while singularity exponents can be derived from any quantity. Besides, Lyapunov exponents are of Lagrangian character (they are obtained letting two close points to evolve following the flow trajectories) while singularity exponents are Eulerian (in particular, they are obtained instantaneously). Nevertheless it seems that both of them can be used to delineate circulation patterns and are thus probably strongly connected; in some sense, Lyapunov exponents are some kind of time average of singularity exponents. Further work on this topic is required.

The information given by the singularity analysis can be used to improve our knowledge about some structures like current waves, filaments or eddies, which have a great

	Gulf Stream	Kuroshio	Agulhas
Longitude range	90^oW - 30^oW	120^oE to 180^oE to	13.5^oE to 36^oE
Latitude range	10^oN to 55^oN	20^oN to 70^oN	46.5^oS to 24^oS
Jan-Feb-Mar 2003			
V_{SLA}	117	154	364
CV	17	15	67
min CV	14	13	49
max CV	21	17	93
Apr-May-Jun 2003			
V_{SLA}	136	146	374
CV	18	18	64
min CV	15	14	53
max CV	23	23	84
Jul-Aug-Sep 2003			
V_{SLA}	147	175	370
CV	18	18	60
min CV	16	14	48
max CV	22	27	79
Oct-Nov-Dec 2003			
V_{SLA}	143	183	371
CV	17	17	60
min CV	14	13	47
max CV	21	21	80
2003			
V_{SLA}	136	165	370
CV	18	17	63
min CV	14	13	47
max CV	23	27	93

Table 2.1: Study on the correspondence of SLA and singularity streamlines for three different regions. Results are obtained for different seasons of the year 2003, and for the whole year. All variances (V_{SLA} and CV) are in cm^2.

impact on ocean transport processes regulating global climate (like CO_2 absorption [93]), ocean biochemistry (as the DMS production [120]) or ocean ecology (as the relation between primary production and the presence and persistence of physical structures like filaments or eddies [86, 88]). The patterns obtained by singularity analysis on MW SST images would be useful for improving our knowledge on some open problems in oceanography and climatology. The accuracy and clarity of details shown in the structure of mesoscale variability of main currents in key areas of the Earth oceans, as for instance the Equatorial zone, the North Atlantic or the Antarctic Ocean, will undoubtedly help oceanographers and climatologists. All those currents are active parts of the main oceanic gyres, which are the physical expression of the mechanisms that control Earth's global heat budget or deep-water formation. Among the phenomena that will be better described, we highlight ENSO, as the effects of current perturbations in the main oceanic gyres are strongly related to climate variability. We hope that the potentialities of this kind of images for oceanic monitoring presented in this paper will be a convincing evidence for stimulating the design of future satellite missions.

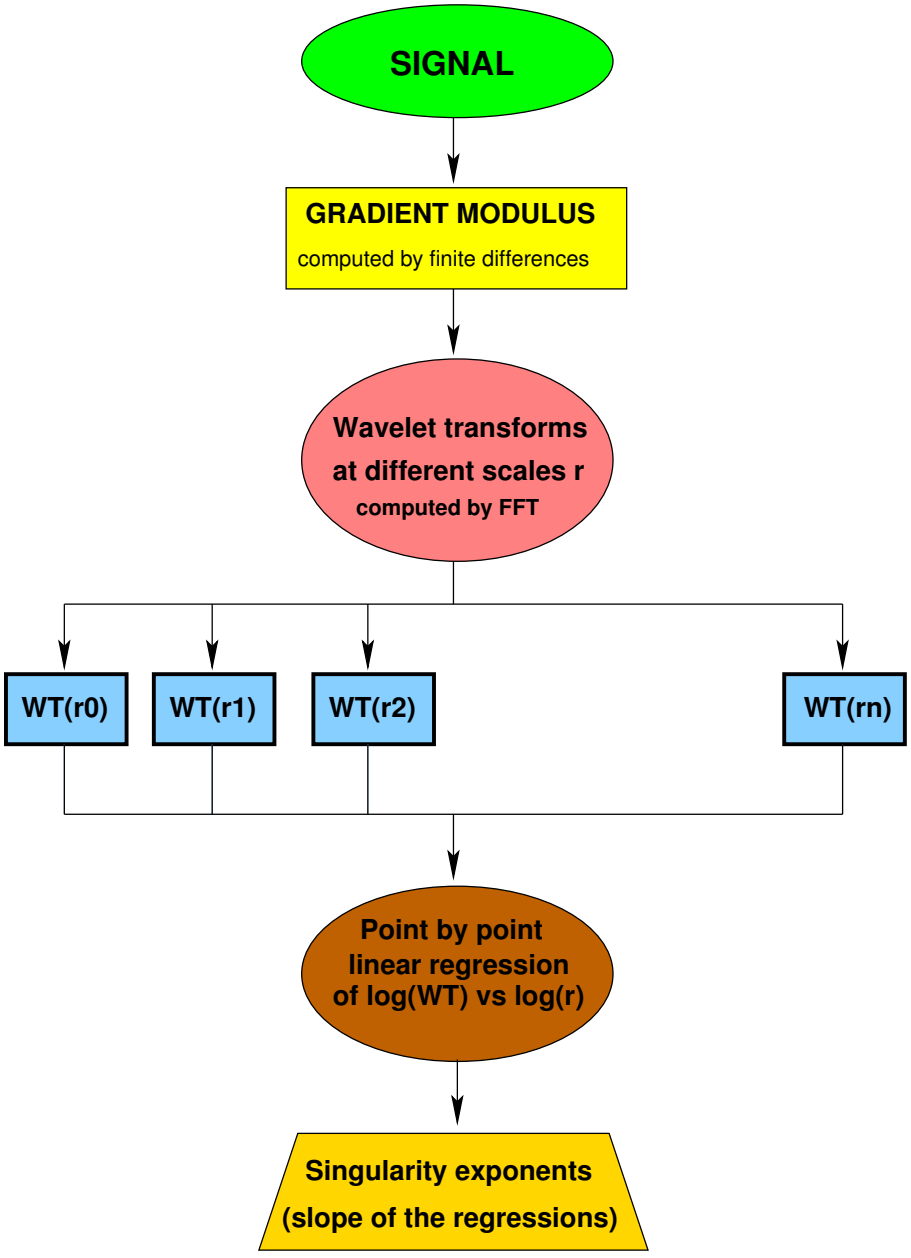

Fig. 2.1: Schematic representation of the algorithm employed to calculate the singularity exponents associated to a given signal. Although not indicated in the algorithm, the quality in the determination can be assessed by means of the regression coefficients in the last step. The scales used in the regression typically range from 1 pixel to the 10% of the total length; the number of sampled scales are typically between 7 and 20. A C program implementing this algorithm with several simple wavelets can be downloaded at http://www.icm.csic.es/oce/people/turiel/SUPP_INFO/MF-analyzer.html; please respect terms of use.

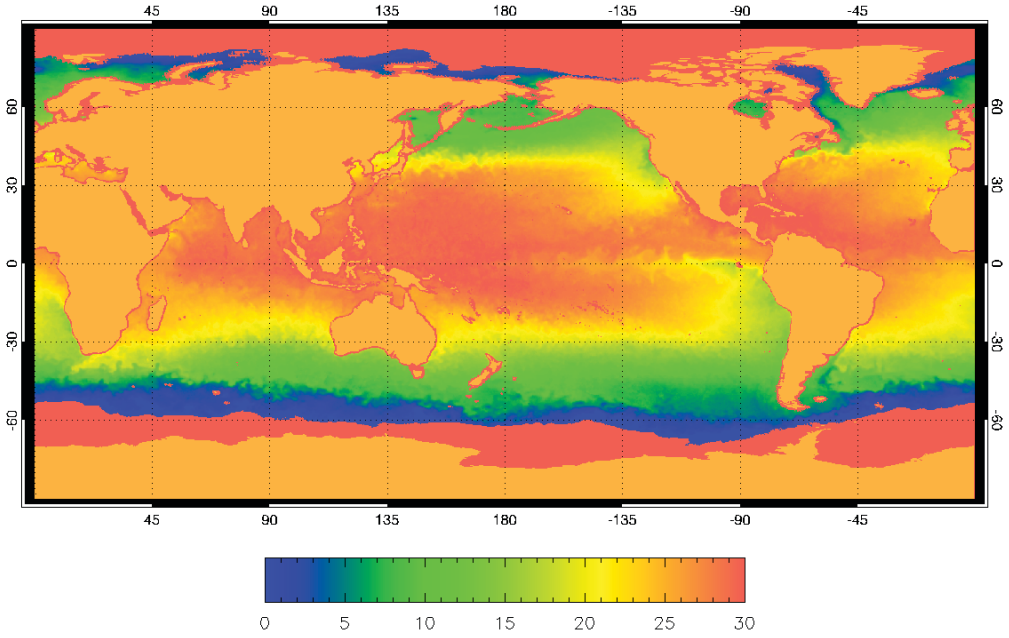

Fig. 2.2: MW SST image for October 1st, 2005. Temperatures in the color bar are expressed in Celsius degrees. Ice-covered are masked with dark orange.

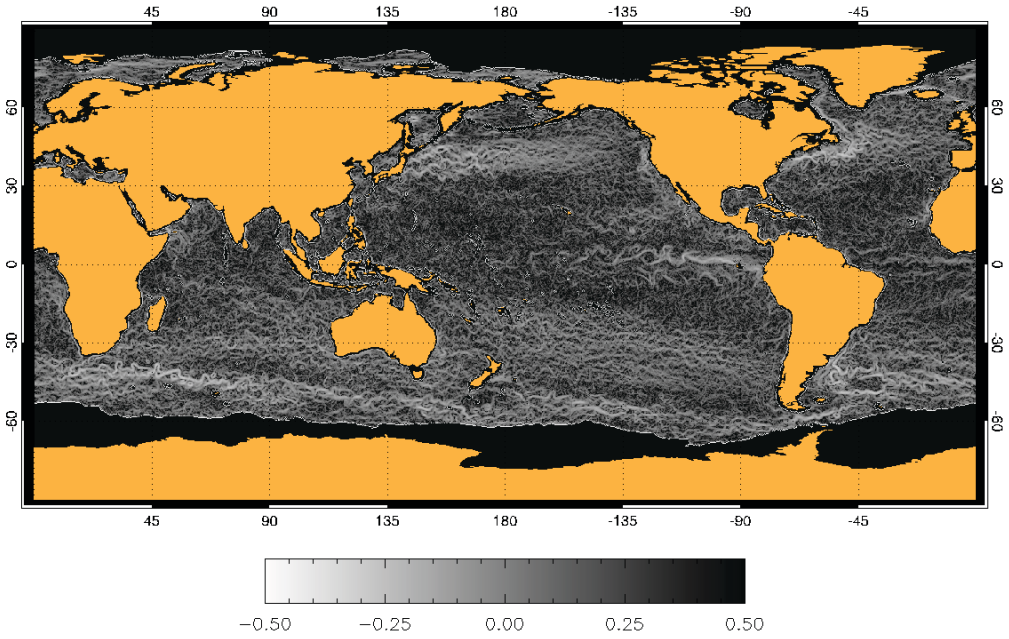

Fig. 2.3: Singularity exponents obtained from MW SST images for the whole globe. Results for October 1st, 2005 (see Figure 2.2). A full-resolution animation for the whole month is at http://www.icm.csic.es/oce/projects/imagen/mssm/.

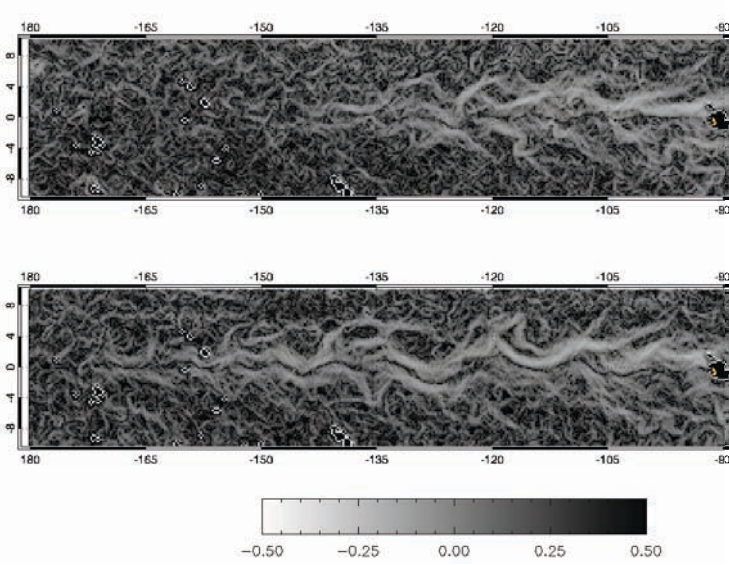

Fig. 2.4: Singularity exponents obtained from MW SST images on the Equatorial Pacific area. Results are for August 1st, 2002 (top) and August 1st, 2005 (bottom). Full-resolution animations for the whole month are at http://www.icm.csic.es/oce/projects/imagen/mssm/.

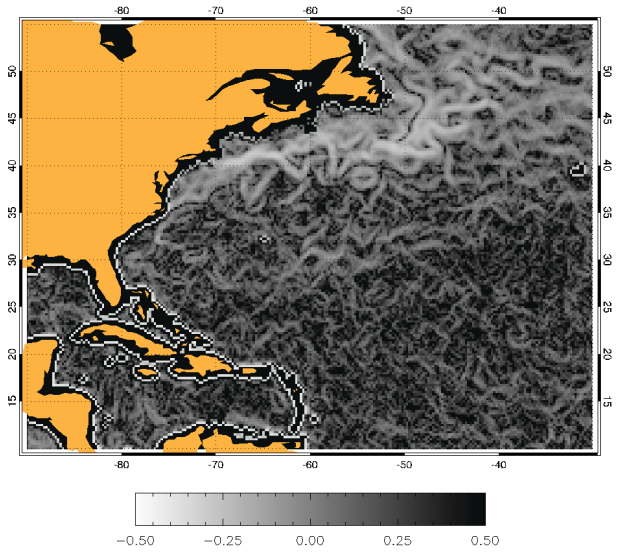

Fig. 2.5: Singularity exponents obtained from MW SST images on the Gulf Stream area. Results are for October 1st, 2005. A full-resolution animated sequence for the whole month is at http://www.icm.csic.es/oce/projects/imagen/mssm/.

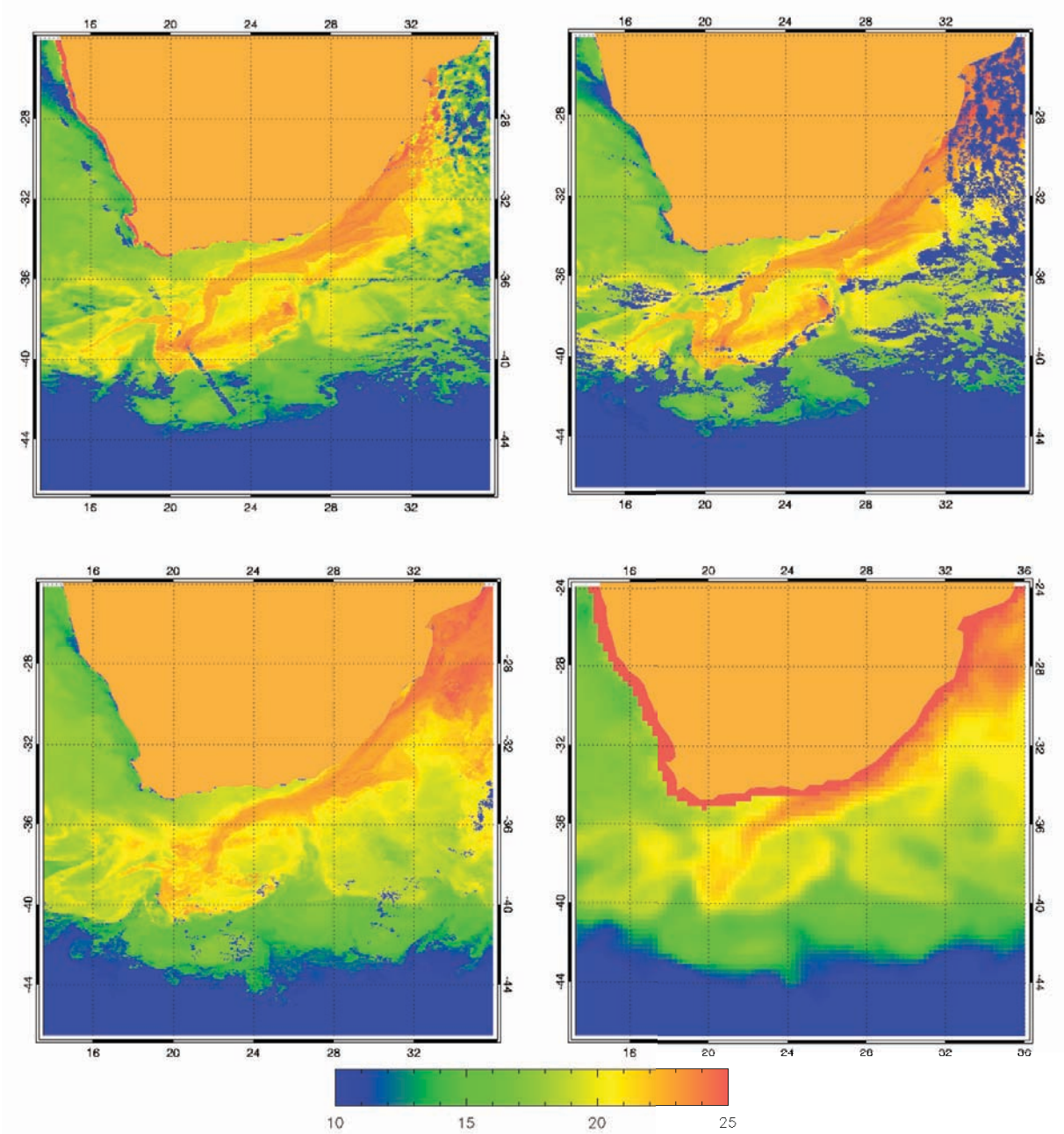

Fig. 2.6: SST images corresponding to November 26th, 2002 from several products: **Top:** AVHRR Pathfinder SST (left) and L2 MODIS daily SST (right). **Bottom:** L2 MODIS weekly SST (week going from 25 November to 2 December) (left) and MW SST (right). Temperatures in the color bar are expressed in Celsius degrees.

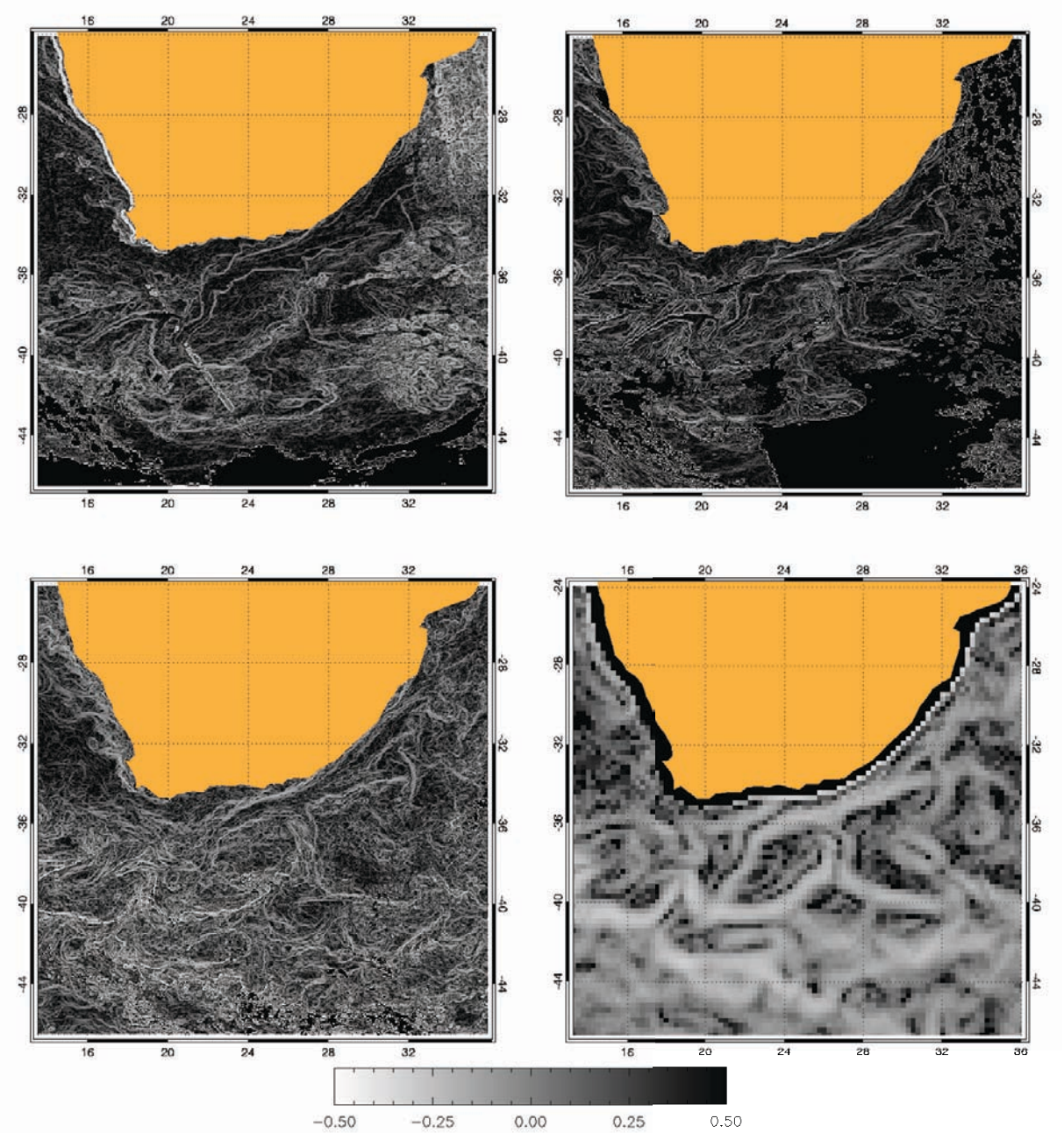

Fig. 2.7: Singularity exponents derived from SST images corresponding to November 26th, 2002.**Top:** AVHRR Pathfinder SST (left) and L2 MODIS daily SST (right). **Bottom:** L2 MODIS weekly SST (week going from 25 November to 2 December) (left) and MW SST (right).

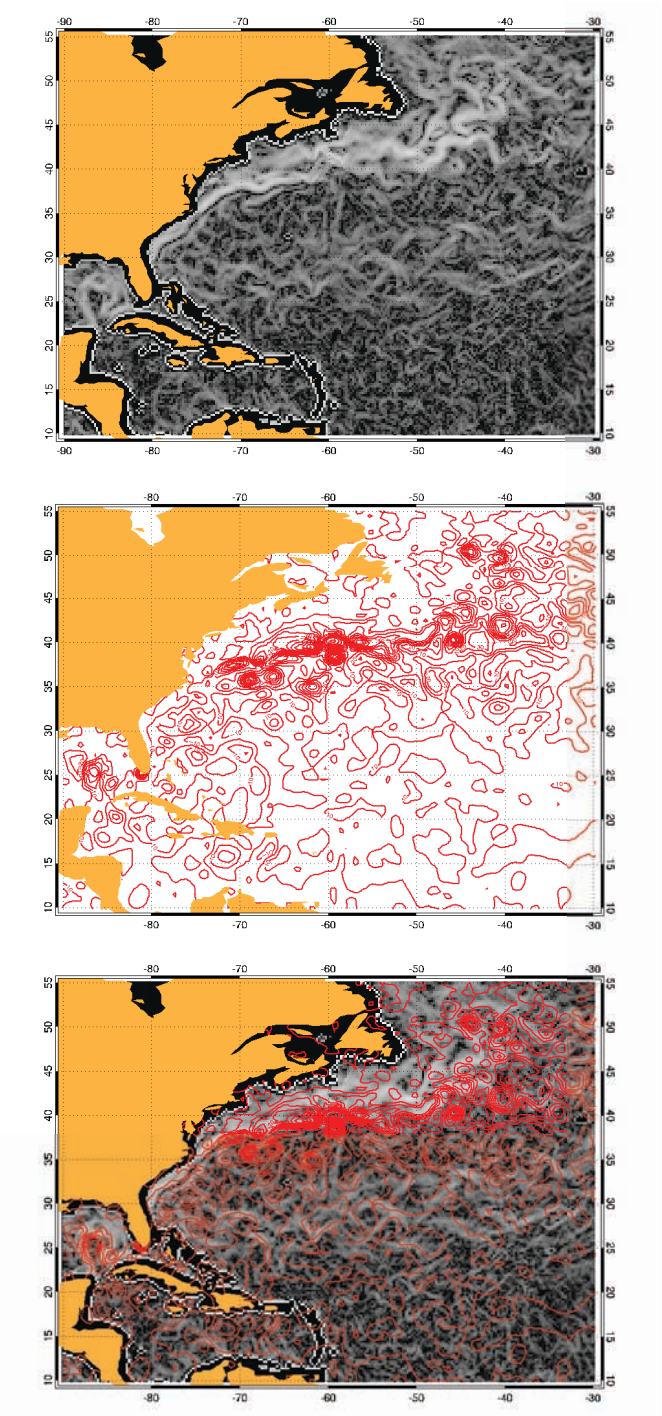

Fig. 2.8: **Top:** Singularity exponents derived from a MW SST image of the Gulf Stream area in January 1st, 2003. **Middle:** Contour levels of SLA derived for the period January 1st to January 10th, 2003. **Bottom:** Contour levels of SLA overimposed on MW SST singularity exponents. The total variance of SLA on this area and time is 108.83 cm^2; the variance of SLA conditioned to the singularity streamlines is 15.20 cm^2 (14.58% of the total variance).

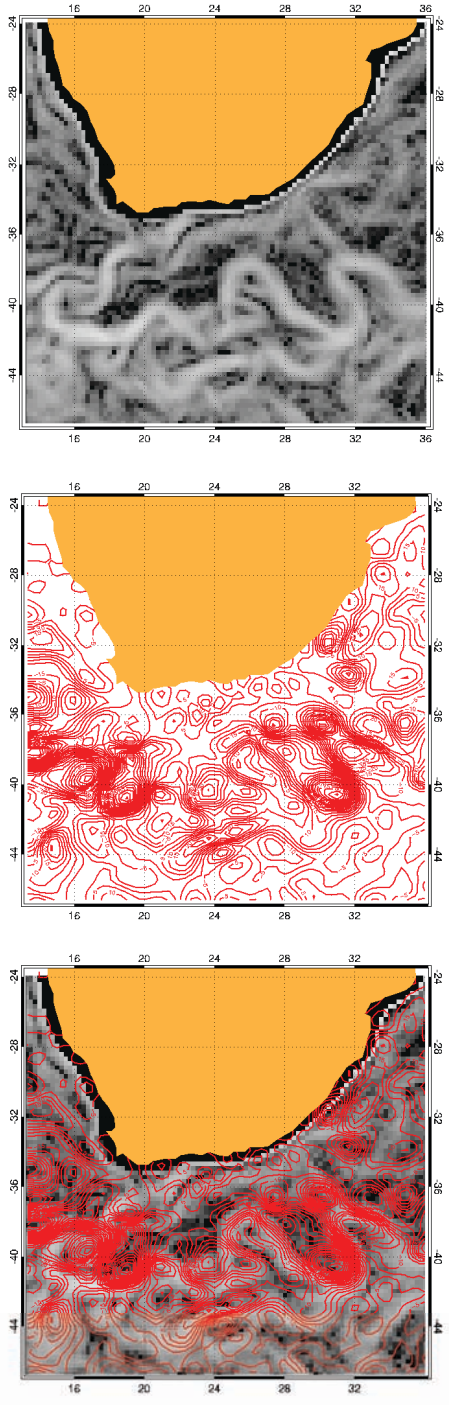

Fig. 2.9: **Top:** Singularity exponents derived from a MW SST image of the Agulhas area in July 3rd, 2002. **Middle:** Contour levels of SLA derived for the period July 3rd to July 12th, 2002. **Bottom:** Contour levels of SLA overimposed on MW SST singularity exponents. The total variance of SLA on this area and time is 287.97 cm^2; the variance of SLA conditioned to the singularity streamlines is 40.12 cm^2 (13.93% of the total variance).

CHAPTER 3

Obtaining and monitoring of global oceanic circulation patterns by multifractal analysis of MicroWave Sea Surface Temperature images

Research is to see what everybody has seen and to think what nobody else has thought.
Albert Szent-Gyorgyi

Obtaining and monitoring of global oceanic circulation patterns by multifractal analysis of MicroWave Sea Surface Temperature images

ABSTRACT

Recent advances in the theory of turbulence, with the introduction of the Microcanonical Multifractal Formalism has favored the development of new techniques for the analysis of remotely sensed data, particularly of scalars as SST. In this work we show that these techniques allow to uncover a fascinating picture in which many features of global ocean circulation patterns emerge in a distinct way. Applications include the characterization of transport, estimation of eddy-mediated mixing, the characterization of the coupling of ENSO perturbation with the equatorial instabilities and a long etc.

Published in *IGARSS, IEEE International,* 1895-1898, 10.1109/IGARSS.2007.4423195.
A. Turiel, J. Solé, V. Nieves and E. García-Ladona

3.1 Introduction

The advances in the acquisition of Sea Surface Temperature (SST) images, with the introduction of new sensors and merged/interpolated products is giving rise to an unprecedented capability for the constant monitoring of oceans at very different ranges of dynamic scales, synoptically and with very good sampling rate [95]. Data from passive MicroWave (MW) sensors are particularly useful, as nowadays Level 2 MW SST images are produced under almost any weather condition, with global coverage and daily; their main drawback lies on their relatively limited resolution.

It is well-known that SST images are composed by coherent features, which are the result of coherent circulation patterns [91]. For that reason, since long ago SST images have been used in order to derive the surface velocity field from them. However, solving the inverse problem (*i.e.*, determining which velocity field has lead to the observed temperature patterns) is extremely complex due to the non-linear interactions in the flow evolution and also because the temperature distribution is the result of an accumulated (integrated) time evolution. Nevertheless, some techniques based on tracking of SST patterns on sequences of images (the most important one being Maximum Cross Correlation, MCC) have been applied to derive sea surface velocity fields, with remarkable results [31, 30, 141]. The main drawbacks of this methodology lie on its limited resolution, in the problems caused by data gaps and in the necessity of properly identifying and tracking patterns in chaotic and complex signals such as SST. In fact, the pervading character of oceanic turbulence leads to a very complex structure in the fluctuation part (*i.e.*, after subtracting long-rage correlations) of SST field [50], which rends pattern recognition and tracking very difficult.

The Microcanonical Multifractal Formalism (MMF) [55] is a new formalism to deal with data obtained under conditions of turbulence with high Reynolds number. MMF represents the step from the more classical statistical characterization of the turbulence (by means of energy spectra, order-two correlations, etc [37]) to a new geometrical approach, in which the signal is decomposed in a hierarchy of fractal sets characterizing the different rates of turbulent dissipation - this is the reason for the name "multifractal". This decomposition is performed in a scale-invariant fashion which imitates the physical process of turbulent cascading (in turbulence, energy is injected from the largest to the smallest scales as a cascade, [100, 20, 76]) and so a good spatial resolution of oceanic structures can be attained [129, 55]. Not only that: it has been argued [16] that the multifractal structure of a scalar is preserved by flow advection, what would imply that each fractal component is at each time instant composed by streamlines. This has been checked in [129] by comparing fractal components and altimetry-derived velocity fields, finding a good correspondence. Hence, it seems that the multifractal decomposition allows recognizing the streamlines with the use of a single SST image.

The presence of data gaps is still a problem in MMF, although less critical than in pattern-tracking methodologies as MCC. The effect of gaps is local and so the perturbation does not extend far ago their locations, although they lead to artificial boundary currents which circulate around the area affected by missing data. It is hence convenient to work with different data types in order to infer the correct streamlines by comparison, or even trying to obtain signals with few missing data. This is precisely the case of MW SST, and so we have performed an study on the capabilities of MMF applied to MW SST data in order to produce steady tracking of the oceanic current lines.

3.2 Singularity analysis

Let us first start by a small introduction to the MMF techniques, and more particularly to singularity analysis, which is the fundamental ingredient to perform the multifractal decomposition. The interested reader can find more details in [132, 129, 127, 55].

The applicability of MMF relies on the existence of local scaling exponents (known as singularity exponents). The singularity exponent of a point is a scale-invariant, dimensionless measure of the degree of regularity or irregularity of the image at that location. The obtaining of singularity exponents allows to detect relevant structures in the flow organization, even subtle structures with very small amplitude [130]. To obtain the singularity exponent of a point, the image must be filtered by means of wavelet projections, in order to reduce the influence of noise and to provide a controlled continuous interpolation over some range of scales. A procedure to assign a singularity exponent to each point in the image is known as a singularity analysis, and is one of the basic ingredients in MMF.

In our case, singularity analysis is performed by a wavelet analysis of numerical estimates of the modulus of the gradient. Let $\theta(\vec{x})$ the value of SST at a point $\vec{x}$ of the image; its gradient will be denoted by $\nabla\theta(\vec{x})$. Given a wavelet Ψ, we define the wavelet projection $T_\Psi|\nabla\theta|(\vec{x},r)$ of its gradient modulus of θ at the point $\vec{x}$ and with scale r as:

$$T_\Psi|\nabla\theta|(\vec{x},r) \;=\; \int d\vec{y}\,|\nabla\theta(\vec{y})|\,\frac{1}{r^2}\Psi\left(\frac{\vec{x}-\vec{y}}{r}\right) \tag{3.1}$$

The signal θ will have a singularity exponent $h(\vec{x})$ at the point $\vec{x}$ is the following equality holds:

$$T_\Psi|\nabla\theta|(\vec{x},r) \;=\; \alpha_\Psi(\vec{x})\, r^{h(\vec{x})} \;+\; o\left(r^{h(\vec{x})}\right) \tag{3.2}$$

where the symbol "$o\left(r^{h(\vec{x})}\right)$" means a quantity which decays to zero if divided by $r^{h(\vec{x})}$ when $r \to 0$. If a signal θ admits singularity exponents at all its points we will say that this signal is multifractal [132]. The conditions which allow applying the MMF are a bit more restrictive although rather technical and not essential for the course of this paper; the interested reader can find the precise framework in [109], and the verification of its validity on SST images in [55].

The accuracy and resolution capability in the determination of the singularity exponents depends on the wavelet used. As discussed in [125], the wavelets leading to the best results are positive functions with adjusted tail decay. Notice that although properly speaking a positive function cannot be a wavelet (they do not verify the admissibility condition, [23, 83]), this fact does not prevent their use for singularity analysis (admissibility is required to represent signals, not to analyze signals).

The other ingredient in MMF is the presence of a particular arrangement of singularities in variables dominated by turbulence. When turbulence is well developed, all the variables for which the stirring by the flow is important enough develop a multifractal arrangement of singularity exponents [65, 37]. In those cases, singularity exponents are arranged in accordance with the multiplicative cascade predicted by the theory [100, 28, 20]. Besides, for those scalars for which advection is dominant enough, the singularity exponents are plainly advected by the flow, at least in a first-order approximation. For that reason, the singularity exponents on SST images allow to delineate the instantaneous streamlines of the motion.

For the experiences shown in this paper, we have used a numerical implementation of the order-1 Lorentzian wavelet (see [132, 125]). This wavelet is defined by its numerical weights and has been designed to optimize reconstruction from the most singular values [126]. The exponents are obtained by a linear regression of $\log T_\Psi|\nabla\theta|(\vec{x},r)$ vs $\log r$ for $r = 1$ to $r = 8$ pixels sampled uniformly in the logarithmic domain.

As discussed in [132, 129, 55], the values that the experimental singularity exponents can take is contained in the interval $(-1, 2)$, although a narrower range, as $(-0.5, 0.5)$ usually contains around 99% of the total values. For that reason, we are more interested in taken this range as the dynamic range for the variable $h(\vec{x})$, in order to enhance details. Besides, the smallest values (*i.e.*, those closest to -0.5) delineate sharp structures, while the greatest values (closest to 0.5) represent smooth behaviors and are associated

to areas without any distinguishable structure. Something which is a bit surprising when singularity analysis is applied is the large amount of emerging singular structures (see figures in the following). In fact, this should be expected as the exponent $h(\vec{x})$ obtained from Equation (3.2) is a measure of the sharpness or smoothness of the transition (that is, the *speed* of the change) but it is independent of its absolute amplitude (which is contained in the factor $\alpha_\Psi(\vec{x})$). So, singularity analysis always gives access to all transitions in the data, even the subtlest ones, and in the case of scalars submitted to turbulence these transitions must be the response of the scalar to the action of the flow shear, so they follow the streamlines.

3.3 Examples of application

In Figure 3.1 we present a typical MW SST image for the whole globe. Some circulation patterns are obvious by visual inspection on this image (as the Gulf Stream and Kuroshio sharp thermal signatures), but over the majority of the areas temperature appear to change rather smoothly and no pattern is recognized. On the contrary, singularity analysis of this image, Figure 3.2, reveals a complex system of currents, with strong filamentation, eddy creation and propagating waves.

Let us study in detail some specific geographical areas. In Figure 3.3 we present a MW SST image for the Gulf Stream area in the North West Atlantic basin. As mentioned above, the thermal signature of this western boundary current is plainly evident in the image, and some close eddies can be guessed. The presence of these eddies is confirmed after the application of singularity analysis, see Figure 3.4. Not only that, but many filaments spawning from the Gulf Stream and other currents lines now become evident. Such stirring patterns and filaments have great impact in biological aspects as for instance primary production [86].

A different kind of study is posed when analyzing phenomena such as the Tropical Instability Waves (TIW) in the Eastern Equatorial Pacific; see Figure 3.5.

Here, the propagation speed of TIW and their evolution can be evaluated by comparing the singularity exponents at different days. In addition, several motion modes can be recognized: observe the double wave front at about -135 degrees in Longitude in August 1st, 2005, which finally merges, interfering in a constructive way in August 15th. The resulting patterns are to Kelvin-Helmholtz instabilities, which are produced in the interface between two horizontal parallel streams of different velocities and densities; the improved detection capability furnished by singularity extraction would allow to improve our underdtanding on TIW generation and evolution.

The study of TIWs is also important in order to characterize some of the effects associated to El Niño-Southern Oscillation (ENSO): it is well-known that the presence of ENSO interferes with the generation of TIW, which become of less amplitude and smaller spatial frequency. With this technique, the phenomenon can be studied in greater detail.

3.4 Conclusion

In this paper, we have seen the potential of the Microcanonical Multifractal Formalism, and particularly of the so-called singularity analysis, for the study of oceanic processes in a steady-basis. An essential ingredient to assess these process is the use of MicroWave Sea Surface Temperature (MW SST) images as starting data, as this kind of images are less affected by cloud cover and strong weather conditions.

With this approach we can study the filamentation of the stronger jet currents, as Gulf Stream, the Kuroshio extension, the Agulhas current, the Malvines current, the Antartic Circumpolar current, etc. The analysis of the structure of the main currents has two main implications. First, the geometry of currents gives information about the way in which the energy of such currents is propagated towards small scales (i.e. if the energy is disipated mainly through vortices or waves), and what is the time sequence of such phenomena. On the other hand these currents are active parts of the main oceanic gyres, which in turn are the physical expression of the mechanisms that control, between others, the global heat budget in the Earth or the deep water formation. On the other hand, many mesoscale eddies are revealed, and the path of their evolution can be tracked; the propagation and characteristics of equatorial instabilities are also neatly evidenced. Particularly important is the possibility of precisely determine the position of oceanic fronts due to their impact in the three dimensional structure of the oceanic waters. This later point would be crucial in studying the upwelling zones, which have a great impact, for instance, in the fisheries.

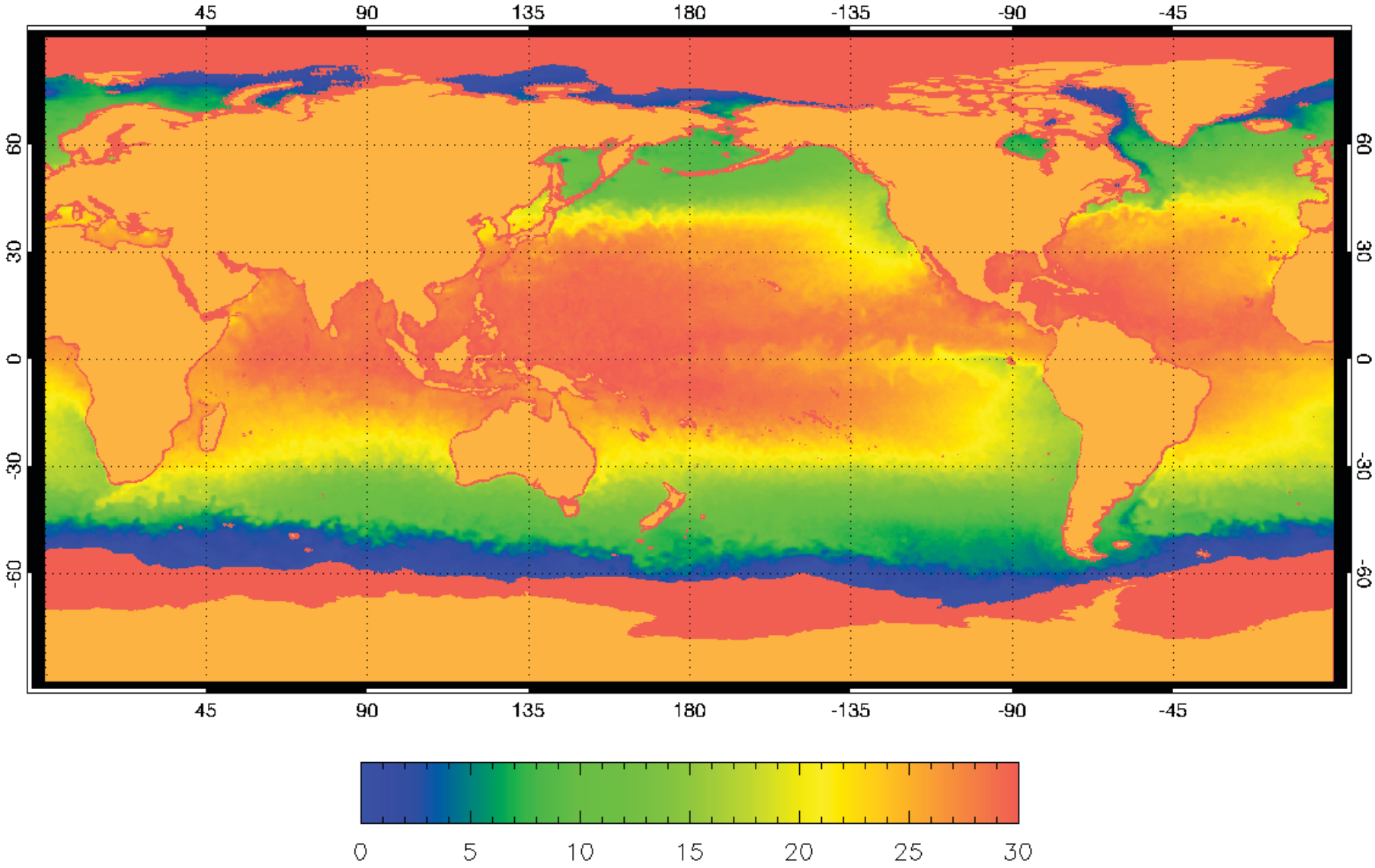

Fig. 3.1: MW SST image for October 1st, 2005 (cylindric projection). Temperatures in the color bar are expressed in Celsius degrees.

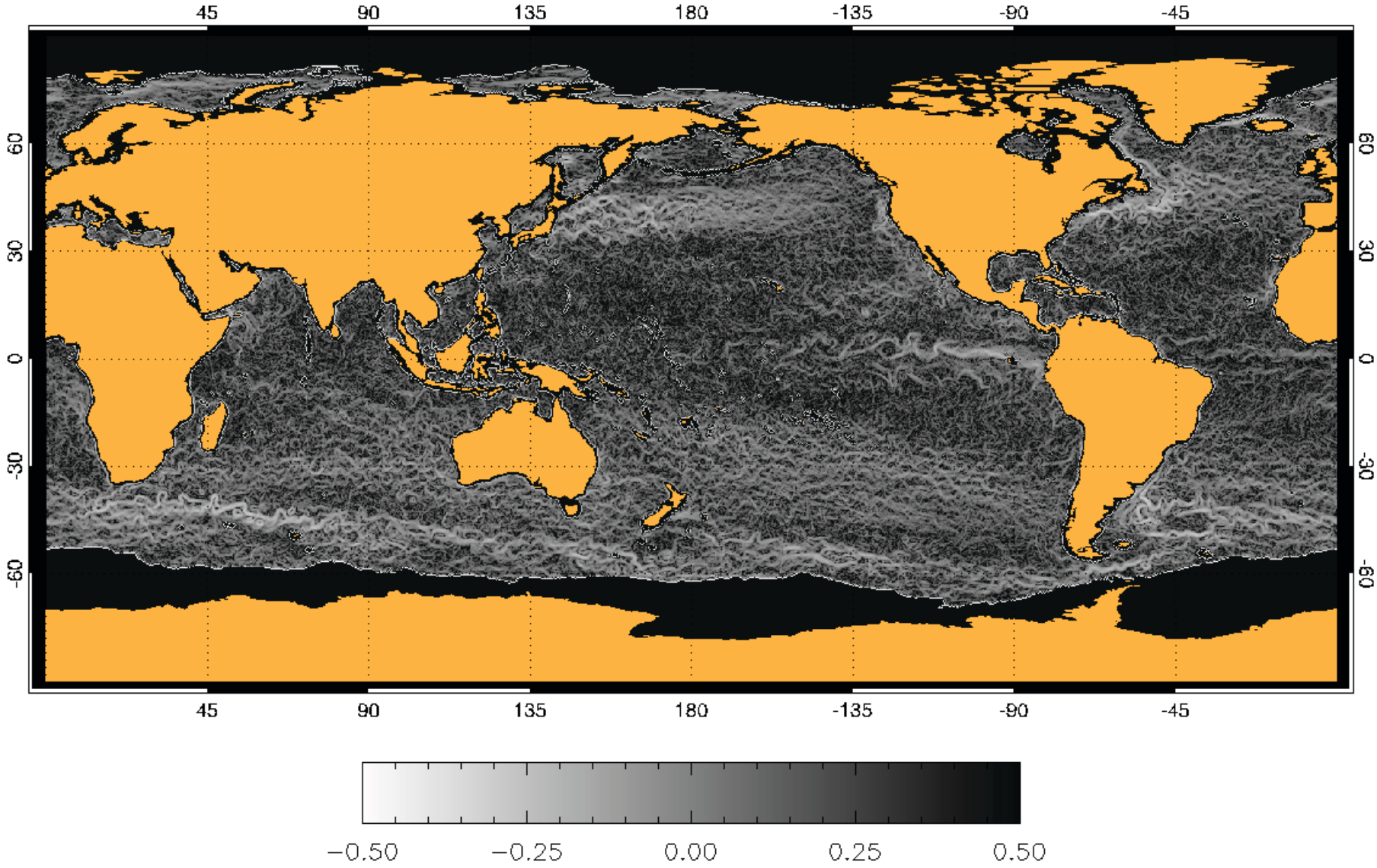

Fig. 3.2: Singularity exponents obtained from MW SST images for the whole globe. Results for October 1st, 2005.

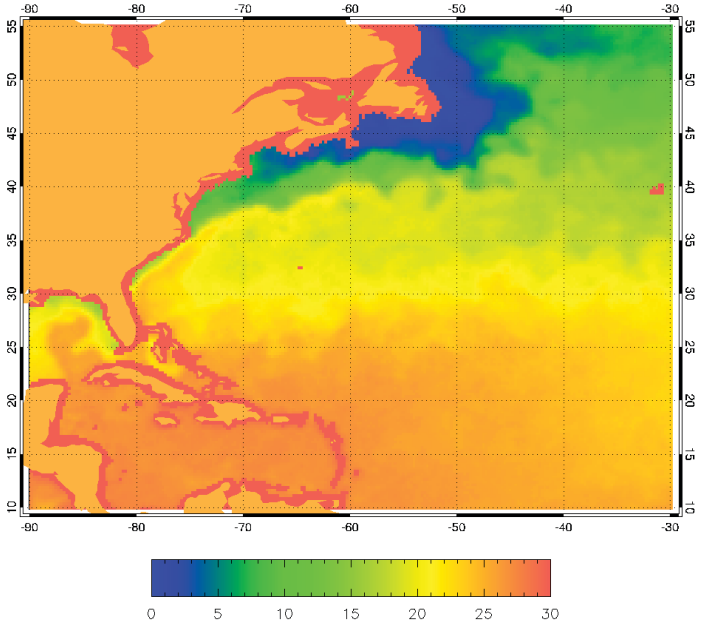

Fig. 3.3: MW SST image for February 1st, 2003 at the Gulf Stream area (cylindric projection). Temperatures in the color bar are expressed in Celsius degrees.

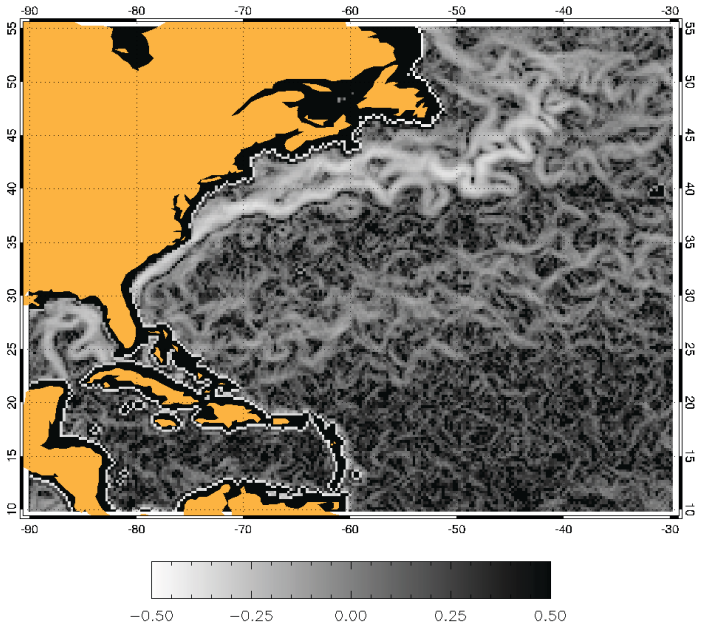

Fig. 3.4: Singularity exponents obtained from MW SST images at the Gulf Stream area. Results for February 1st, 2003.

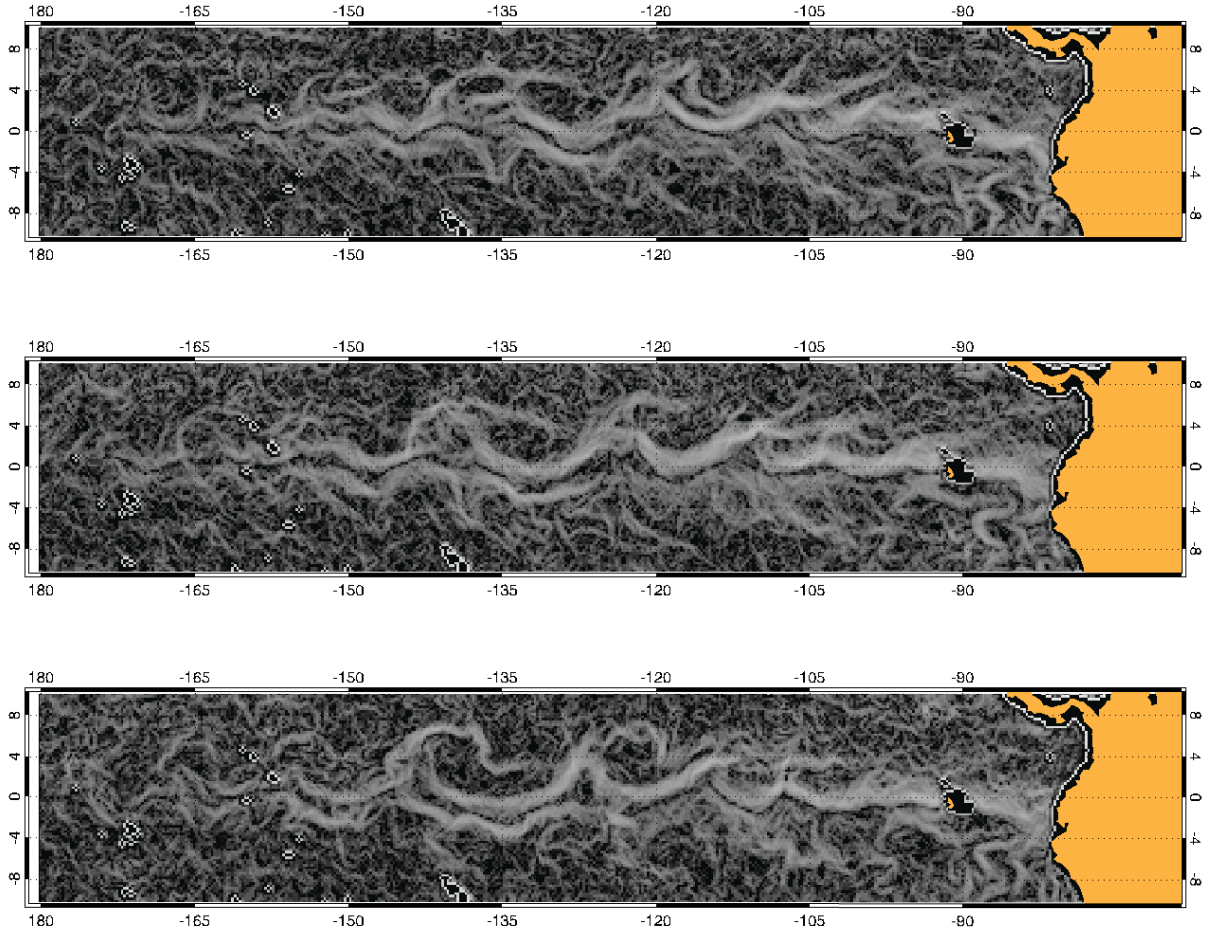

Fig. 3.5: Singularity exponents obtained from MW SST images at the Eastern Equatorial Pacific. Results for August 1st (top), 8th (middle) and 15th (bottom), 2005.

CHAPTER 4

Técnicas multifractales para la extracción de la función de corriente a partir de imágenes de la superficie del mar

Never confuse movement with action.
Ernest Hemingway

Técnicas multifractales para la extracción de la función de corriente a partir de imágenes de la superficie del mar

ABSTRACT

One of the greatest challenges in the remote sensing of the ocean is the obtention of relevant dynamical quantities from satellite images of different tracers (e.g., SST, chlorophyll concentration, etc). In this paper we will discuss how the use of new techniques on singularity analysis allow to retrieve the main instantaneous streamlines, and how these can be used, in the context of the geostrophic approximation, to deduce the associated stream function, with better spatial and temporal resolution than other methods. Besides, we will discuss some of the potential applications of this method.

Uno de los grandes retos de la teledetección oceánica es la obtención de magnitudes dinámicas relevantes a partir de imágenes de satélite de trazadores de diversos tipos (e.g. temperatura superficial, concentración de clorofila, etc). En este artículo discutimos cómo el uso de nuevas técnicas de análisis de singularidades permiten recuperar las principales líneas de corriente instantáneas, y cómo éstas pueden ser usadas, dentro de la aproximación geostrófica, para deducir la función de corriente asociada, con mejor resolución espacio-temporal que otras técnicas similares. Así mismo, discutiremos algunas otras aplicaciones potenciales de este método.

Published in *Rev. de Teled., Num.Esp.: Oceanografía y Teledetección,* ISSN: 11330953.

A. Turiel, V. Nieves y E. García-Ladona

4.1 Introducción

La obtención de imágenes de satélite adquiridas en diversos rangos de frecuencias nos permite acceder a estimaciones razonables del valor de determinadas variables intensivas (como la temperatura superficial del mar -SST-) sobre áreas determinadas por la capacidad resolutiva de la malla de captores utilizada. Estas variables proporcionan información sobre el estado termodinámico del mar, pero no dan información directa sobre el movimiento de las masas de agua. Sin embargo, la estructura y distribución de estas variables no es completamente aleatoria, sino que viene determinada por la evolución pasada y movimiento presente del océano, ya que se comportan como trazadores más o menos pasivos. Con todo, extraer el campo de velocidades a partir de estas variables es un problema inverso muy complejo e irresoluble en la práctica sin las aproximaciones convenientes. La estimación más directa del campo de velocidades es conseguida por los satélites altimétricos, los cuales nos proporcionan mediciones del nivel de elevación del mar, a partir del cual se puede deducir el campo de corrientes en la aproximación geostrófica. Sin embargo, los satélites altimétricos sólo proporcionan información a lo largo de la traza del satélite, así que se debe combinar la información de diversas trazas por medio de técnicas de análisis objetivo [72] para obtener verdaderos mapas de altimetría. Dado que las trazas son adquiridas de modo no simultáneo, los mapas así construidos sólo podrán considerarse sinópticos a escalas suficientemente grandes. En latitudes medias y con la red actual de satélites altimétricos se puede conseguir construir mapas de resolución razonable para el tamaño de la mesoescala ($\sim$ 30 Km) cada 10 días, aproximadamente. Aún cuando la resolución espacial y temporal de los mapas altimétricos es adecuada para el estudio de muchos fenómenos de interés oceanográfico, ésta dista mucho de lo que sería deseable para aplicaciones más operacionales. Hace ya más de 20 años se han propuesto múltiples aproximaciones para extraer el campo de velocidades directamente de las imágenes de trazadores. Todos los métodos se basan en el seguimiento de estructuras observables en los trazadores a través de secuencias de imágenes; citemos aquí el método MCC [31, 38] y el Optical Flow (OF) [12]. Estos métodos implican una pérdida en resolución espacial y temporal, lo que conduce a campos de velocidad resueltos sólo ligeramente mejor que los altimétricos. Recientemente, se ha propuesto un nuevo método - denominado Método de la Función de Corriente Máximo Singular, FCMS - para la evaluación de la función de corriente a partir de imágenes de trazadores [129]. Dicho método se basa en las propiedades de multifractalidad inducidas en el trazador por la estructura turbulenta del campo de velocidades subyacente. El método permite hacer una obtención muy fina de estructuras y garantiza la mejor resolución espacial y temporal posible: los campos de velocidad tienen la resolución espacial de las imágenes de partida, y son instantáneos. Sin embargo, los campos necesitan ser recalibrados localmente, ya que el método sólo proporciona velocidades adimensionalizadas. En este artículo haremos una revisión de este método y discutiremos sus aplicaciones potenciales y extensiones futuras.

4.2 Método de la función de corriente máximo singular

4.2.1 Análisis de singularidades

El análisis de singularidades se basa en que, en un fluido turbulento, todas las variables dominadas por la mecánica del fluido acaban siendo dominadas por la intermitencia. Esto implica que sus valores, aún cuando son extremadamente caóticos, han de seguir una estadística caracterizada por una distribución infinitamente divisible, con modas pequeñas y colas largas y pesadas (elevada curtosis) [28]. Esto implica, en añadidura, que la relevancia de una estructura en la organización del fluido es local y por tanto no se han de buscar umbrales globales, sino locales y adaptados al seguimiento de la cascada multiplicativa predicha por la teoría estándar de la Turbulencia Completamente Desarrollada. Esta relevancia local de cada punto viene medida por el exponente de singularidad local, $h(\vec{x})$, que se calcula por proyección de wavelets a diversas escalas. Si la señal a analizar es $s(\vec{x})$, dada una wavelet (para nosotros, función escalable) $\Phi(\vec{x})$, definimos la proyección de s sobre Φ a la escala r y el punto $x\,\epsilon\,\mathbf{R}^2$ como:

$$T_\Phi s(\vec{x},r) \;\equiv\; r^{-2}\int d\vec{y}\,\Phi\left(\frac{\vec{x}-\vec{y}}{r}\right)\;s(\vec{y}) \tag{4.1}$$

La proyección en wavelets permite hacer un zoom local - regulado por el parámetro de escala r - sobre el comportamiento de s alrededor del punto x, y por eso es útil para determinar su estructura. En sistemas dominados por la turbulencia del fluido subyacente se ha podido comprobar [37, 5] que las proyecciones en wavelet del gradiente de la señal dependen del parámetro de escala r como una ley de potencias, esto es,

$$T_\Phi|\nabla s|(\vec{x},r) \;=\; \alpha_\Phi(\vec{x})r^{h(\vec{x})} \tag{4.2}$$

El exponente de singularidad local $h(\vec{x})$, que no depende de la wavelet [5], nos permite caracterizar localmente la regularidad o irregularidad de la función en ese punto; valores menores de $h(\vec{x})$ (típicamente negativos) indican un comportamiento más irregular y singular, mientras que a medida que $h(\vec{x})$ crece la función se vuelve más suave y se aproxima más a su desarrollo de Taylor. Una señal que posee exponentes de singularidad en todos sus puntos se dice multifractal, debido a que los conjuntos asociados a cada valor del exponente se organizan como fractales de diferentes dimensiones [37]. Los escalares en el océano suelen presentar estructura multifractal (Figura 4.1).

4.2.2 Construcción de la FCMS

Indicios teóricos y experimentales de datos oceánicos [1] y resultados teóricos recientes (sin publicar) muestran que las singularidades son advectadas por el fluido. La interpretación física de esta conservación es que, cuando la turbulencia está completamente desarrollada, las singularidades $h(\vec{x})$ están en equilibrio dinámico con el campo de velocidades. Podemos usar esta propiedad para derivar un campo de velocidades $2D$, lo que puede aplicarse también en el caso del océano cuando la hipótesis cuasi-geostrófica es válida. Diseñamos a este fin un algoritmo que se basa en construir la función de corriente Ψ a partir de información sobre las líneas de corriente principales. [126] demostraron que se puede reconstruir una señal multifractal a partir de su gradiente restringido a un subconjunto fractal particular, la llamada Variedad Más Singular (VMS en lo que sigue). El algoritmo para la generación de la función de corriente (Función de Corriente Máximo Singular (FCMS), denotada por ΨM) procede en dos pasos: 1. Se calculan los exponentes de singularidad de todos los puntos, y se separan aquellos asociados al valor más singular (con cierta dispersión experimental). Esto determina la VMS (líneas de corriente principales; ver Figura 4.2). 2. Se asigna un valor consistente al gradiente de ΨM sobre la VMS. Como ΨM es una función de corriente, $\nabla \Psi M$ ha de ser perpendicular a las líneas de corriente de la VMS; pero nos falta determinar su módulo y sentido. Como carecemos de esta información dinámica, tomamos $\nabla \Psi M$ de módulo constante, adimensional, y con el mismo sentido del gradiente de la señal original, ∇s. A contiuación, reconstruímos como en [126]; ver Figura 4.3.

Esta construcción nos permite obtener una función de corriente adimensional que posee propiedades importantes; en particular, posee las mismas líneas de corriente de la función de corriente original si las singularidades son advectadas. Comparaciones directas con mapas de altimetría muestran una buena correspondencia en la mesoscala (ver Figura 4.4). Sin embargo, para poder dar un uso operacional a la FCMS, ésta ha de ser calibrada para retornar valores de velocidad con dimensiones adecuadas. Además, la hipótesis de celeridad constante sobre la VMS puede fallar localmente y, lo que se muestra como más importante en los experimentos, el sentido puede estar invertido si el gradiente del escalar original no apunta en la misma dirección del gradiente de densidad.

4.3 Extensiones y líneas futuras

4.3.1 Calibración de la FCMS

El mayor punto débil de la FCMS son las hipótesis de celeridad constante y coalineación con el gradiente de la señal. Sin embargo, si alguna información dinámica adicional está accesible es muy sencillo implementarla en la construcción: simplemente, se sustituye $\nabla\Psi M$ en la VMS por el valor apropiado y se reconstruye de la misma manera que antes. Resultados preliminares integrando datos altimétricos muestran una gran calidad y buena correspondencia con la función de corriente real [53].

4.3.2 Detección de estructuras oceánicas

El análisis de singularidades en sí mismo es una poderosa herramienta para la extracción de estructuras, dado que los exponentes $h(\vec{x})$ permiten detectar transiciones que son localmente importantes aunque sean globalmente irrelevantes; además, por construcción, estos exponentes proporcionan una medida que es invariante de escala, por lo que no se prefija el tamaño de la detección. Como un caso particular de interés oceanográfico, recientemente se ha aplicado esta técnica a imágenes del satélite MeteoSat para detectar frentes de ondas internas de varios cientos de kilómetros propagándose en mar abierto cerca de la Cresta de Mascarene [135]; ver Figura 4.5. El interés de este trabajo es que permitiría reanalizar bases de datos de imágenes buscando indicios semejantes; se ha de notar que la presencia de estos frentes de ondas internas era desconocida en la zona observada, ya que se pensaba que la cresta actuaba como un muralla y no había propagación al lado oeste.

4.4 Conclusiones

En este artículo hemos visto que la técnica del análisis de singularidades para el tratamiento de datos en teledetección oceánica es una herramienta primordial para la obtención de magnitudes físicamente significativas. El análisis de singularidades resulta especialmente apropiado ya que los datos poseen una estructura caótica determinada por la turbulencia de alto número de Reynolds del océano, y por tanto toda la teoría de turbulencia es aplicable. Es precisamente esta teoría la que predice la organización del fluido en frentes de singularidad, los cuales forman variedades materiales y por tanto conservadas por la evolución. Gracias a esas propiedades de conservación, hemos visto

que se pueden derivar fácilmente aproximaciones instantáneas de la función de corriente geostrófica. Además, el método es fácilmente escalable para integrar información dinámica adicional cuando ésta está disponible. La técnica de clasificación de singularidades, aunque adaptada para el tratamiento de variables termodinámicas donde la advección domina, es también de utilidad para el tratamiento de imagen en general, y así su enorme sensibilidad (ya que se basa en una caracterización local e independiente de la escala) la hace apropiada para detectar ondas que modulan sólo sutilmente la señal percibida por el satélite; así, hemos visto que se puede usar análisis de la singularidad para detectar ondas internas en imágenes del espectro visible.

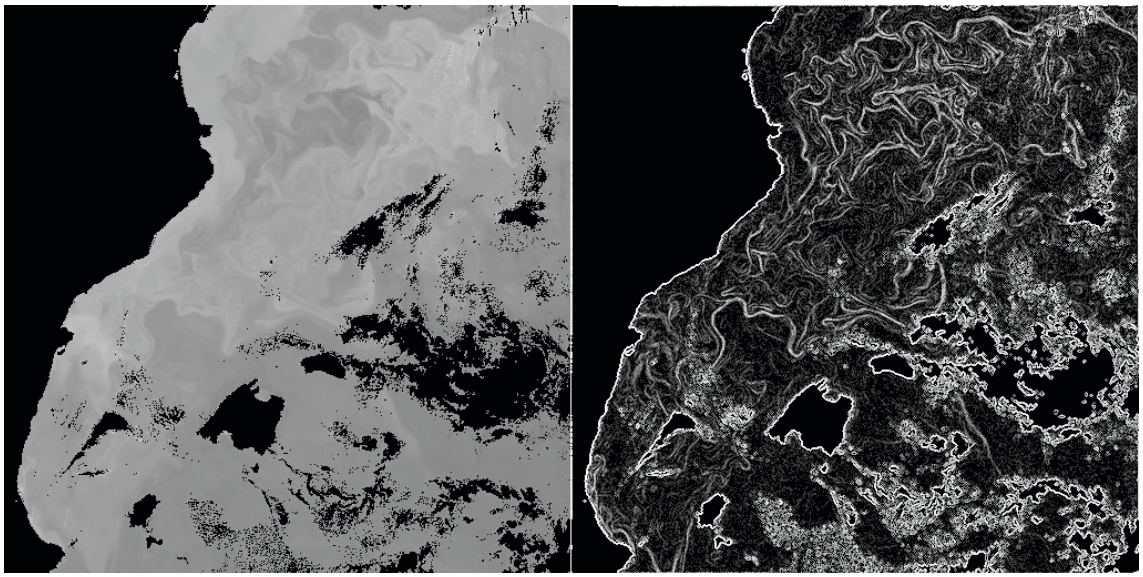

Fig. 4.1: Izquierda: Imagen de concentración de clorofila en niveles de gris en escala logarítmica, obtenida del satélite SeaWiFS (procesamiento OC4). Derecha: Singularidades locales obtenidas; los colores más brillantes corresponden a exponentes más singulares. Las líneas de costa y transiciones océano-nube son muy singulares, así como las líneas frontales; sin embargo, otras estructuras más sutiles, corrientes y meandros también aparecen destacados.

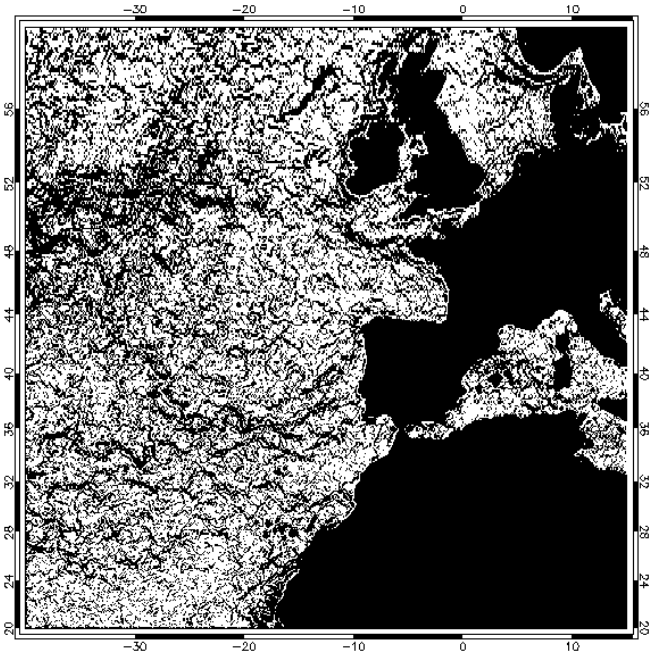

Fig. 4.2: Variedad Más Singular, derivada de una imagen de SST analizada del 14 de Abril de 2006 (Fuente: http://www.ifremer.fr/las/servlets/dataset).

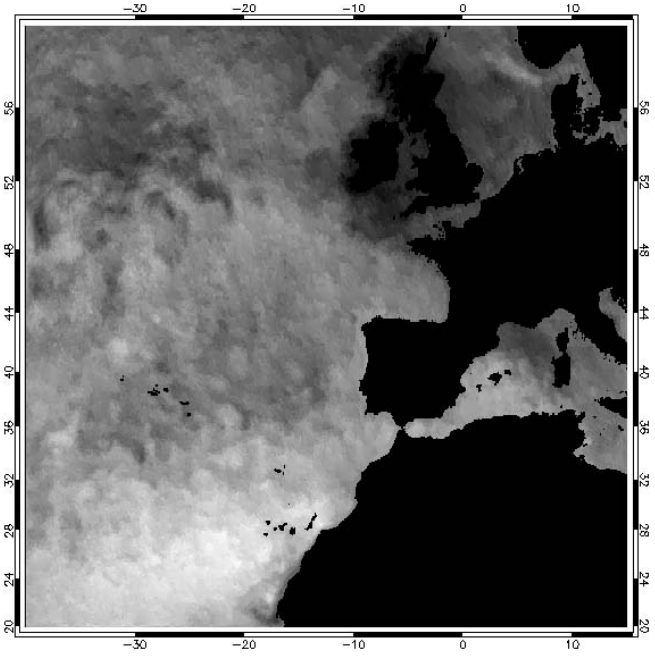

Fig. 4.3: Función de corriente máximo singular derivada.

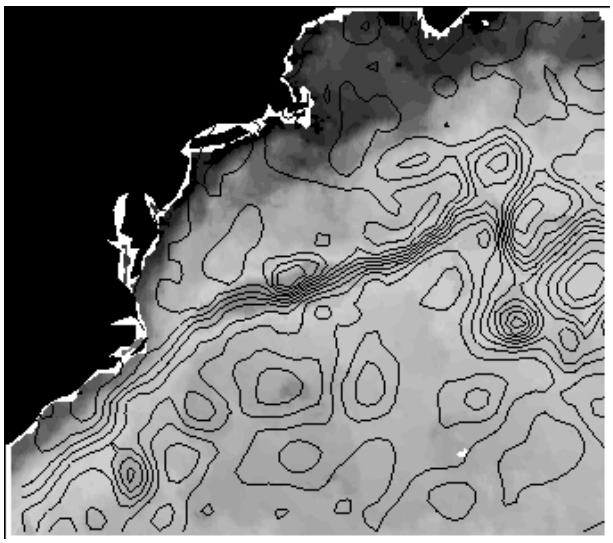

Fig. 4.4: Superposición de las curvas de nivel de un mapa altimétrico sobre la FCMS derivada de SST analizada en la zona de cabo Hatteras. La imagen de SST original fue obtenida el 31 de Diciembre de 2003.

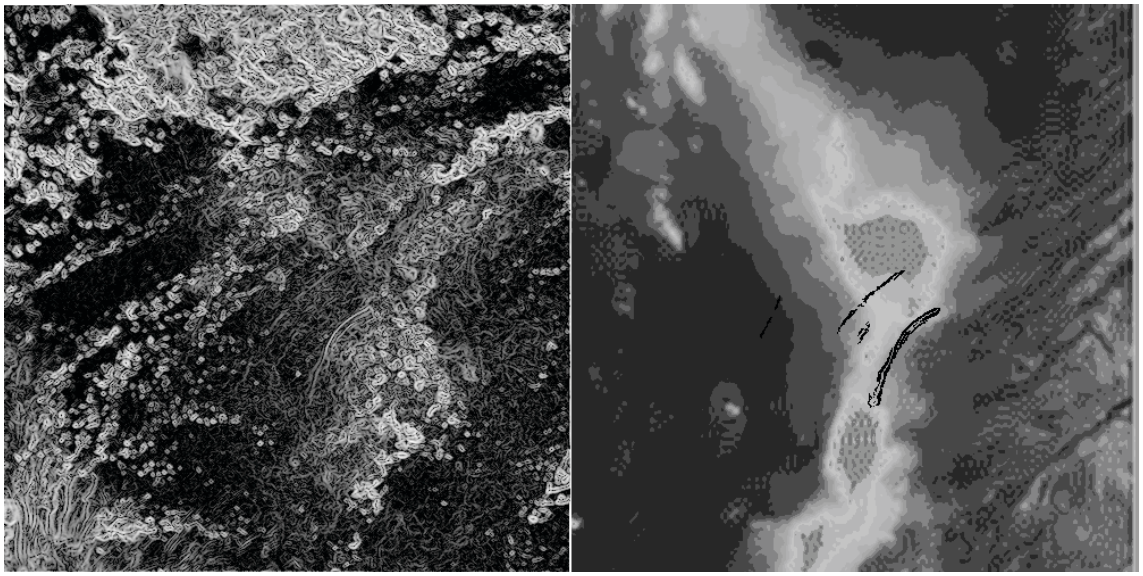

Fig. 4.5: Izquierda: Singularidades de una imagen del MeteoSat del 26 de Diciembre de 2004, en la cresta de Mascarene (NE de Madagascar; el área mostrada va de 57.5^oE a 62.5^oE en longitud, y de 14.75^oS a 8.25^oS en latitud). Las singularides frontales del centro de la imagen son frentes coherentes de ondas internas. Derecha: Superposición de los frentes sobre la batimetría. El frente se amplifica en el canal entre mesetas.

CHAPTER 5

Common turbulent signature in sea surface temperature and chlorophyll maps

...
everything withdraws
nothing remains
all flows
...
Heraclitus of Ephesus

Common turbulent signature in sea surface temperature and chlorophyll maps

ABSTRACT

Oceans and 2D turbulence present similar characteristics, as for instance the dominant role played by eddies in energy and matter transport. However, providing a complete justification of this analogy is difficult, as it requires knowledge of the ocean's dynamic state at different instants and over large scales. Recently, new techniques coming from the Microcanonical Multifractal Formalism have made it possible to infer the streamlines from the analysis of satellite images of some scalar variables. In this paper, we will show that this information is enough to characterize the scaling properties of the energy cascade, which is manifested as a multifractal signature; further, the multifractal signature is obtained at each location in a local basis. Different scalars obtained from satellite measurements such as Sea Surface Temperature or Surface Chlorophyll Concentration present essentially the same multifractal structure, which is interpreted as a consequence of the pervading character of the turbulent advection at the scales of observation.

Published in *Geophys. Res. Letters,* VOL. 34, L23602, doi:10.1029/2007GL030823, 2007.

V. Nieves, C. Llebot, A. Turiel, J. Solé, E. García-Ladona, M. Estrada, and D. Blasco

5.1 Introduction

The spatial variability of surface ocean tracers is characterized by patchy distributions, resulting from the interplay and balance between advection, diffusion and source and sink processes [42, 87]. Observational evidence of sea surface patterns has stimulated the investigation of which processes dominate and ultimately are the responsible for such complexity. For a tracer such as the Sea Surface Temperature (SST) it has been argued that stirring by the horizontal flow may account for the mesoscale surface signatures seen from satellite images [1]. At such scales ocean dynamics is almost two-dimensional, in quasi-geostrophic equilibrium with low values of the Rossby number (Rossby deformation radii from 10 to 100 km). Theoretical arguments on the stirring of tracers by 2-dimensional time-dependent flows have led to explanations of many of the observed features in SST patterns [139]. In the particular case of chlorophyll pigments, some studies on the spatial variability of remote sensing images did not find significant differences between the spectra of CZCS and SST from AVHRR images [24]. This fact led to the conclusion that phytoplankton cells in dynamic areas such as upwelling systems behave largely as passive scalars. Similar trends were found by studying SeaWiFS imagery [26], although recent analyses of MODIS images in the Arabian Sea have shown that the variability of SST and Chlorophyll are different [79].

Analysis of variance or second order moments poorly characterizes the variability of intermittent fields, so multifractal analysis is much more appropriate [76, i.e]. Very recently the introduction of the Microcanonical Multifractal Formalism (MMF), and in particular the application of singularity analysis to SST images has confirmed the existence of a multifractal structure of surface spatial patterns over a range of scales that includes the mesoscale [129]. One of the most relevant results of this analysis is the observed correspondence between the multifractal patterns in SST and the flow structure at these scales [55]. The correspondence is a consequence of the establishment of a multiplicative cascade of the scalar, analogous to the energy cascade of the flow owing to the fully developed turbulence regime [105]. In fact, a passive scalar for which advection dominates should inherit the multifractal character of the flow [129].

In this paper, we will present some new experimental confirmation of the correspondence of the multifractal structure of scalars with the one coming from the flow. We will show that, as for SST, surface Chlorophyll Concentration (CC) maps also exhibit multifractality over a range of scales including the mesoscale. More importantly, the geometrical and statistical structure of the multifractal singularities in CC maps is very close to that of SST images. Further, when different regions are considered the spectra of singularities are coincident. This is evidence that, at the scales resolved by the data, common underlying mechanisms account for the spatial variability of both tracers, and hence their intrinsic dynamics is decoupled from their structure at those scales.

5.2 Data employed in this study

For the present work, 47 couples of satellite images derived from Aqua-MODIS ocean color sensor have been processed. MODIS (Moderate Resolution Imaging Spectroradiometer) is a key instrument on board the Terra (EOS AM) and Aqua (EOS PM) satellites from NASA. Two different geographical regions were considered. The first one,"North Atlantic Area", extends from 65 to 30 degrees W in longitude, and from 45 to 60 degrees N in latitude. The second region, "South Africa Area", extends from 5 to 25 degrees E in longitude and from 40 to 10 degrees S in latitude. North Atlantic Area includes part of the Labrador peninsula and of East and West Greenland currents; in addition, on its Southeast side it encompasses a portion of the limit of the North Atlantic gyre delimited by the North Atlantic Current, which transports warm waters from the Gulf Stream poleward. South Africa Area covers the Benguela current, which is the eastern boundary current of the South Atlantic subtropical gyre advecting cool waters to the tropics; it is a region characterized by a richly productive marine ecosystem due to an important upwelling coastal system [45]. At each time and location, Aqua-MODIS images of two different types have been considered: chlorophyll concentration (CC) and daytime sea surface temperature (SST) images, spatially averaged (Level 3 products) over a 4x4 km^2 pixel grid (resolution at the equator). Processing details can be found here:

http://oceancolor.gsfc.nasa.gov/DOCS/modis_sst/.

We have processed daily-derived SST images only, in order to have SST and CC images as simultaneous as possible. The images are affected by noise and are spatially discontinuous due to several effects, including cloud cover, aerosol corruption, orbital gaps and aberrant values in the SST/CC algorithms. A single image can be the result of the merging of two or m, so evidencing that singularity analysis serves to isolate a universal mechanismore satellite passes, which partially diminishes errors and data loss; however, the merging process also blurs to some extent the sharpest transitions and tends to produce slightly mislocated singularity fronts. This blurring does not equally affect both types of images, so any image comparison should be based on regional comparisons instead of point to point comparisons. For each area, we tried to generate two ensembles with similar numbers of coupled SST-CC images, selecting those images with as few lost data as possible. We thus chose twenty-four images corresponding to South Africa Area, captured during 2005 and twenty-three images from the North Atlantic, captured in a period extending from 2003 to 2006 and almost evenly representing all seasons.

5.3 Singularity analysis

Recently [129, 55], a new approach to turbulence analysis, based on the explicit geometrical organization of the flows, has arisen. This approach intends to characterize local scaling properties at each point (geometrical or microcanonical approach), instead of global properties of the statistical ensemble (statistical or canonical approach).

In MMF, the key concept is that of the singularity exponent: each point in the flow can be characterized by a singularity exponent, which is a dimensionless, scale-invariant measure of the regularity or irregularity of the flow in the neighborhood of that point [129]. The local singularity exponent $h(\mathbf{x})$ of a given field $s(\mathbf{x})$ at the point $\mathbf{x}$ can be obtained, for any vector $\mathbf{r}$ small enough, from the following scaling

$$\frac{1}{r}|s(\mathbf{x}+\mathbf{r}) - s(\mathbf{x})| \ \sim \ r^{h(\mathbf{x})} \tag{5.1}$$

where r is a given resolution scale. The singularity exponent $h(\mathbf{x})$ is a measure of the degree of regularity of s at $\mathbf{x}$: negative values correspond to sharp transitions (brighter colors in the figures), while positive exponents represent smooth, regular structures (darker colors in the figures). The values of $h(\mathbf{x})$ typically fall in the range (-1,2) [129, 55]. Expressions such as Equation (5.1) are generically known as Singularity Analysis for the function $s(\mathbf{x})$ [129]. The scaling properties of the velocity field are in general difficult to quantify, but they can be connected to the scaling properties of related variables much more accessible and easier to observe. A typical case is that of scalar variables. If a multifractal hierarchy sensu Parisi & Frisch [105] is evidenced for a given scalar, we will accept that its most plausible origin is the turbulent flow driving the scalar. That is, the flow transmits its singularity exponents to any scalar for which advection is strong enough [1, 129]. As a consequence, the obtaining of singularity exponents starting from any scalar quantity reveals properties of the flow motion. Experimental evidences [1, 129] indicate that singularities are advected by the flow. Hence, the spatial distribution of singularities should trace the instantaneous streamlines of the motion and therefore, the velocity field can in principle be retrieved [129].

Equation (5.1) is very appealing and easy to relate to the properties of the flow. However, long-range correlations can mask the largest singularity exponents [129]. Thus, $s(\mathbf{x})$ has to be filtered. Continuous wavelet transforms, defined as projections of the signal at different resolutions, are appropriated to filter multiscaling functions without disturbing scale invariance properties. In addition, it is convenient to work with the

gradient modulus of the signal, $|\nabla s|(\mathbf{x})$, to improve the spatial resolution of the results [135]. Equation (5.1) has a wavelet-transformed counterpart:

$$T_\Psi|\nabla s|(\mathbf{x},r) \;\sim\; r^{h(\mathbf{x})} \tag{5.2}$$

where $T_\Psi|\nabla s|(\mathbf{x},r)$ is the wavelet projection of $|\nabla s|$ over the wavelet Ψ at the point $\mathbf{x}$ and the scale $r>0$, defined as:

$$T_\Psi|\nabla s|(\mathbf{x},r) \;\equiv\; \int d\mathbf{x}\;\; |\nabla s|(\mathbf{x}\,)\,\frac{1}{r^2}\Psi\left(\frac{\mathbf{x}-\mathbf{x}}{r}\right). \tag{5.3}$$

(see, for instance, [129]). A family of wavelets has been shown [129, 55] to be the most efficient to attain good discrimination and resolution capabilities, the Lorentzian family: $\Psi_\gamma(\mathbf{x}) = 1/(1+|\mathbf{x}|^2)^\gamma$, for $\gamma \geq 1$. We have used a numerical implementation of $\Psi_{\gamma=1}$ for the analyses shown in this paper.

5.4 Validity of MMF for SST and CC images

An extensive presentation of MMF is given in [55]. Let us summarize here the three conditions for MMF:

i) Each fractal component is scale-invariant: at any point $\mathbf{x}$, a well-defined local power-law scaling of exponent $h(\mathbf{x})$, according to Equation (5.2), must be observed for a large enough range of scales r. We have verified that the equation holds with good accuracy (using the criterion introduced in [55]) up to 149 pixels (596 km) for both SST and CC.

ii) The whole multifractal hierarchy is scale-invariant: the probability distributions of singularities obtained at different scales r lead to the same singularity spectrum curve $D(h)$. From the empirical histogram $\rho_r(h)$ obtained at the scale r we can obtain the singularity spectrum [135, 55], according to

$$D(h) \;=\; d \;-\; \frac{\log\left(\frac{\rho_r(h)}{\max\,\rho_r(h)}\right)}{\log r} \tag{5.4}$$

We have evaluated the histograms at the original resolution and after a reduction by a factor 4 (curves not shown). We conclude that this property is well satisfied by SST and CC images.

iii) The curve $D(h)$ is convex, which implies that the cascade is actually developed in the flow (see [55]). The curves shown in Figure 5.3 are convex, so validating this condition.

So, both SST and CC are multifractal signals in the sense of MMF. We hypothesize that this structure is a consequence of oceanic turbulence.

5.5 Comparison between SST and CC multifractal structures

In Figure 5.1 we show a couple of SST-CC Aqua MODIS images and their associated singularity exponents according to MMF in the South Africa Area. Singularity analysis puts in evidence main frontal regions with an unprecedented quality but also many subtle non-trivial structures, revealing the presence of eddies and flow lines that passed almost unnoticed in the original images. Remarkably enough, there is a good visual correspondence between the features detected in SST and CC, reinforcing the assumption of a common dynamical origin for the two multifractal structures.

The cascading processes associated to each type of scalar can be compared by studying the statistics of the corresponding singularity spectra; in this case, MMF allows a derivation of the structure of the turbulent cascade with relatively reduced datasets leading to experimental values of $D(h)$ with a typical uncertainty of about 0.05 [135]. As shown in Figure 5.3 a good correspondence of the turbulent cascades is found over the two regions under study for both scalars. All singularity spectra are defined on about the same range of values, and differences in $D(h)$ are less than 0.1, compatible with the experimental uncertainty. For both types of data, SST and CC, the good correspondence of the singularity spectra obtained for two distant geographical regions indicates that the underlying mechanisms which gave rise to the multifractal structures should be similar.

We arrive at the same conclusion when comparing the singularity spectra of SST and CC. Although theoretically granted if advection induces the multifractal structure, a point-by-point coincidence between singularities is hard to verify on data, as singularities appear slightly mislocated due to differences in acquisition processes and the own spatial and functional uncertainty of the singularity analysis. We will thus define a local degree

of closeness between the singularity maps. The proposed measure is given by a weighted local regression coefficient. Our measure of closeness between h_T and h_C is given by $\rho_{TC}(\mathbf{x}) = \frac{\sigma_{TC}(\mathbf{x})}{\sigma_T(\mathbf{x})\sigma_C(\mathbf{x})}$, where $\sigma_T^2(\mathbf{x}) = \langle h_T^2\rangle_{\mathbf{x}} - \langle h_T\rangle_{\mathbf{x}}^2$, $\sigma_C^2(\mathbf{x}) = \langle h_C^2\rangle_{\mathbf{x}} - \langle h_C\rangle_{\mathbf{x}}^2$ and $\sigma_{TC}(\mathbf{x}) = \langle h_T h_C\rangle_{\mathbf{x}} - \langle h_T\rangle_{\mathbf{x}}\langle h_C\rangle_{\mathbf{x}}$

At any point $\mathbf{x}$, we will define the weighted average of any function of h_T and h_C, $F(h_T, h_C)$, in the following way:

$$\langle F(h_T, h_C)\rangle_{\mathbf{x}} \equiv \frac{1}{N_{\mathbf{x}}} \sum_{\mathbf{x}'} \frac{F(h_T(\mathbf{x}\,), h_C(\mathbf{x}\,))}{b(h_T(\mathbf{x}\,))b(h_C(\mathbf{x}\,))}\, w(\mathbf{x} - \mathbf{x}\,) \tag{5.5}$$

where $N_{\mathbf{x}} = \sum_{\mathbf{x}'} \frac{1}{b(h_T(\mathbf{x}'))b(h_C(\mathbf{x}'))}\, w(\mathbf{x} - \mathbf{x}\,)$ is a normalization constant which takes into account the points $\mathbf{x}$ actually available; $b(h)$ is a positive function measuring the uncertainty in the value of h; and $w(\mathbf{x})$ is an appropriate weighting function, used to define the relative importance of the points on the region centered around $\mathbf{x}$. A reasonable choice for $w(\mathbf{x})$ is an isotropic function (that is, only depending on $|\mathbf{x}|$) that decays with distance. Good weighting functions are those in the scale-invariant family, namely: $w(\mathbf{x}) = \frac{1}{\mathbf{x}^{\alpha}}$ for $\alpha = 2$ in our case. With respect to the h-uncertainty, measured by the function $b(h)$, we have used an heuristic estimate, based on the observations reported in singularity analysis of images of different types [129]. We have used $b(h) = 0.1$ for $h \leq 0.1$ and $b(h) = h$ for $h > 0.1$.

As the distributions of h_T and h_C are identical (see Figure 5.3), the only possible linear transformation is $h_T = h_C$. Hence, when ρ_{TC} is close to 1, both types of singularity exponents can be considered as identical over that region. Due to all the processing effects, the coincidence is not perfect, although remarkable. Looking at the maps of local regression coefficients, Figure 5.2, we can confirm the closeness between the maps of SST and CC exponents, specially over free areas. This, together with the coincidence of spectra, evidences the existence of a similar turbulent-like cascading process acting on SST and CC. We conclude that we are certainly extracting information on a dominant mechanism, the advective mode of the flow acting on both scalars.

5.6 Conclusions

The evidence shown in this paper can be summarized by saying that over a rather broad range of scales, including the mesoscale, ocean turbulence has a strong influence on the geometrical arrangement of tracers of very different nature. This is supported by the remarkable similarity between the spectra of singularity exponents over distinct regions

for both tracers. Then the spatial arrangement for the most singular exponents, which basically identify the places with strong enough advection of the scalars, gives information on the streamlines. This has two relevant consequences. First, as an added value we are in fact inferring a large amount of instantaneous information on the dynamics of ocean flows. The obtaining of singularity exponents from images may allow to determine a first estimate of the instantaneous field of sea surface currents [129]. Systematic and extensive re-analysis of recent satellite imagery data bases, covering up to twenty years of SST and ten years of CC, opens the way to assess at a global scale the effects of climate variability and change over the past two decades. Furthermore, the local correspondence of SST and CC singularities due to the existence of a common cascade process may make it possible to use SST data (which are more abundant than CC data) for helping the inference of reasonable distributions of CC at those locations where CC data are lacking. On the other hand analyzing the areas in which the correspondence of both tracers fails may help to identify where the intrinsic dynamics of the tracer is in competition with flow advection which in turn would serve, in the case of CC, to improve our knowledge on ocean phytoplankton communities and improve our understanding of biological processes.

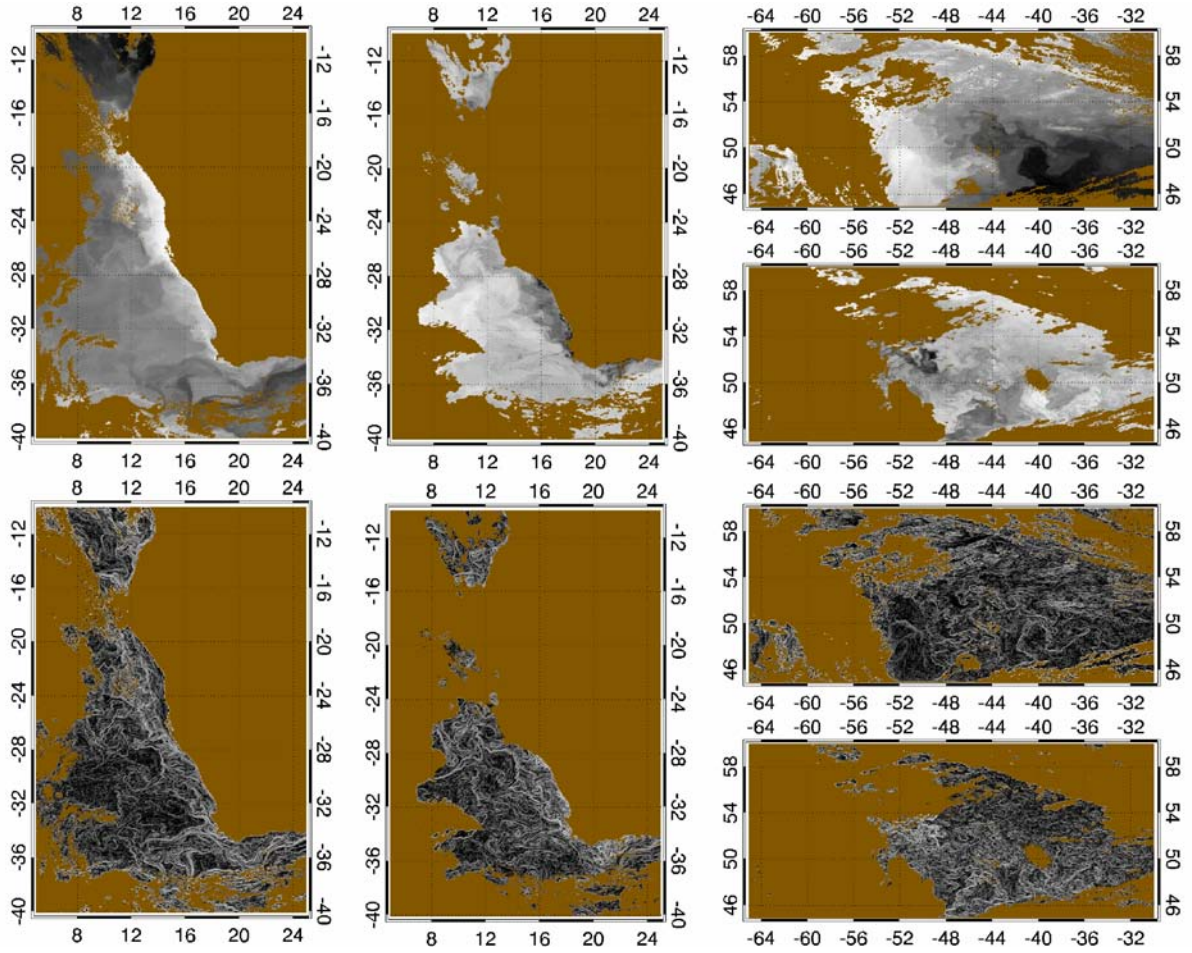

Fig. 5.1: Figures from left to right and from top to bottom. Vertical maps: data obtained in the South Africa Area in April 28, 2005, which correspond to SST and CC; singularity exponents associated to SST and CC images for the same area and period. Horizontal maps: images from North Atlantic Area in April 25, 2006, showing both scalars as well as their respective singularity exponents.

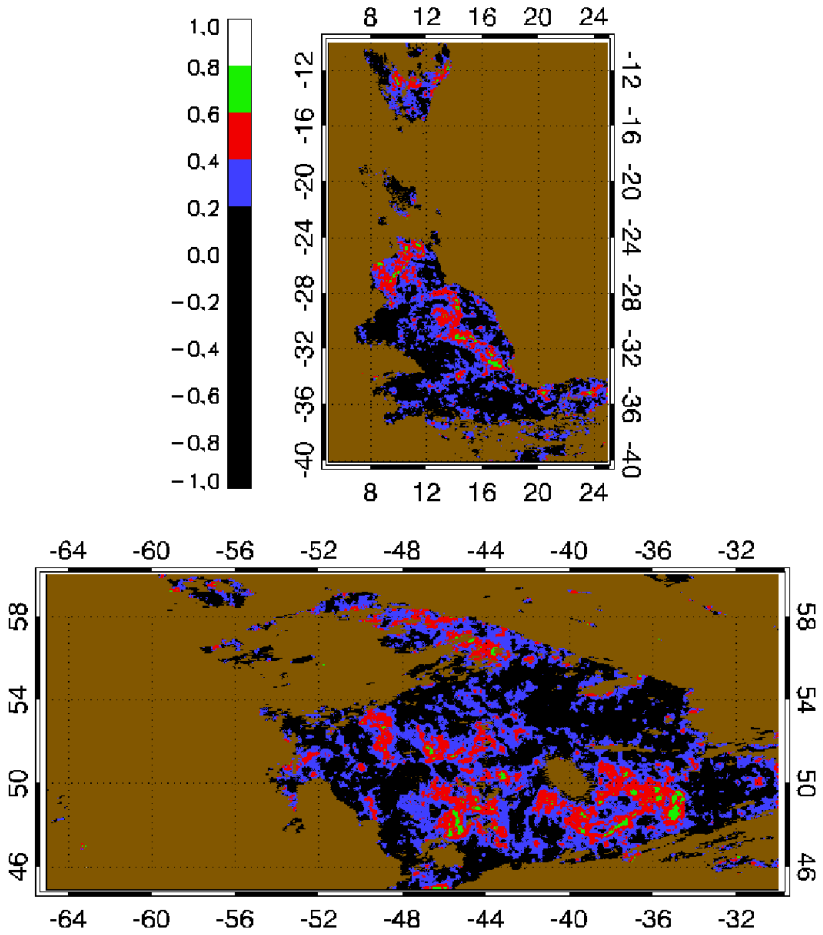

Fig. 5.2: Local correlation coefficients between SST and CC singularity exponents shown in Figure 5.1.

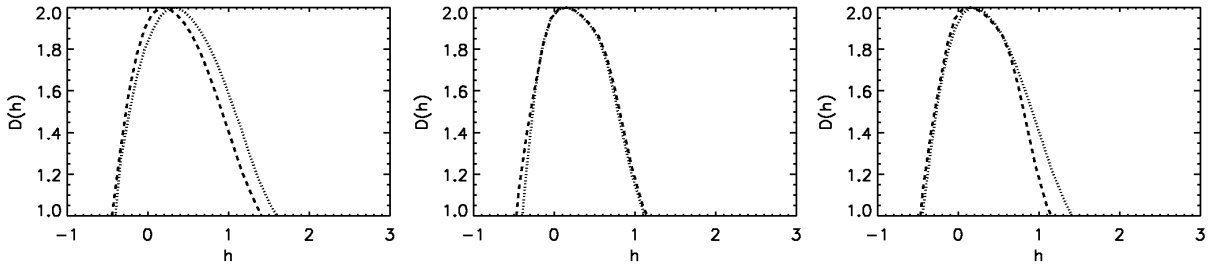

Fig. 5.3: From left to right: comparison of the singularity spectra $D(h)$ derived from SST in the North Atlantic (dotted line) and the South Africa Area (dashed line); the same for the spectra derived from CC, with identical conclusions; comparison of singularity spectra obtained from the whole dataset of SST images (dotted line) and CC images (dashed line).

CHAPTER 6

Analysis of ocean turbulence using adaptive CVE on altimetry maps

It is better to be "roughly" right
than to be "precisely" wrong.
Albert Einstein

Analysis of ocean turbulence using adaptive CVE on altimetry maps

ABSTRACT

It has been often argued that oceanic turbulence is similar to 2D turbulence; they share many properties and more particularly they seem to be driven by the dynamics of coherent vortices over large scales. For this reason, the application of techniques based on the extraction of coherent vortices as the Coherent Vortex Extraction (CVE) seems a natural choice for the description of ocean data. In this paper we will discuss on the properties of oceanic turbulence under the perspective of the Microcanonical Multifractal Formalism (MMF), specifically for the description of altimetry data. We will see that MMF gives a good description of the geometry and statistical properties of altimetry data. We will show that a direct application of CVE on altimetry data has a rather low performance in comparison to other systems, which we justify as a consequence of the inhomogeneous character of ocean turbulence. We also show that a MMF-based separation criterion improves the standard CVE and allows to mitigate these problems. The results are discussed in the perspective of a cascade-based description of ocean turbulence.

Accepted in *Journal of Marine Systems*.
V. Nieves and A. Turiel

6.1 Introduction

Since the early years of remote sensing significant developments in the understanding of ocean processes at the mesoscale have been made; however, there is still a considerable room to improve our processing capability of satellite observations. So far, our insight on ocean dynamics has been gained mainly through the assessment of simple quantities with dynamic meaning either using altimeter-derived data [70, 107, 52, 53, 106] or some estimates of surface currents derived from sequential SST imagery [31, 141, 16]. Nevertheless, these techniques cannot be used to explain ocean behavior from an instantaneous image and at different scales, in contrast with other approaches that are embedded in the framework of turbulence like the Microcanonical Multifractal Formalism (MMF) [55].

Mainly due to the difficulties to obtain precise estimates of the velocity fields in experimental situations, there are quite few accurate characterizations of the scaling properties of velocity fields and related quantities at mesoscale [4]. This is particularly problematic for ocean data [103, 90, 140, 4, 18]. In spite of this fact, during last decades there have been some advances in the understanding of the complexity of ocean turbulence, based on relating the scaling properties of the velocity field with the scaling properties of other variables that are more accessible by means of satellite data such as tracers [75, 79, 67]. As evidenced in statistical studies, ocean dynamics at the mesoscale and 2D turbulence have similar characteristics [91, 57, 54]. MMF uses this resemblance, and gives a step forward going from the classical statistical approach to a geometrical characterization. MMF provides an estimation of the spatial arrangement of any scalar for which advection is important enough. It has been shown that the organization of a turbulent flow presents a hierarchy of fractal sets [105, 4, 129]. By extracting these fractal components from tracer data it is possible to infer sea surface currents from satellite images of some scalar variables such as surface temperature or chlorophyll concentration [129, 55]. Moreover, we can obtain information of the energy injection process from the largest to the smallest scales and the opposite - which explains the production of the hierarchy of eddies [92, 90, 76]. Now, with MMF we can go beyond and prove that Sea Level Anomaly (SLA) maps have a multifractal structure own to Fully Developed Turbulence (FDT). This is precisely one of the goals of the present work.

Another goal is to provide a compact description of oceanic turbulence by means of an appropriate multiscale representation which mimics the known features of the multiplicative cascade. For doing so, we have taken a technique used to represent Direct Numerical Simulations (DNS) of 2D homogeneous turbulence, namely the Coherent Vortex Simulation technique (CVS). This technique analyzes vorticity fields by means of orthogonal wavelet filtering. Wavelets supply a description, which is both local and multiscale, so they are a good tool to describe 2D-turbulence signals. In this way, the flow is broken down into coherent regions (dominated by eddy-like vorticity parcels), and

incoherent regions of random movements. Turbulence causes the formation of eddies of many different length scales that interact with each other, although most of the kinetic energy and enstrophy of the turbulent motion is contained in the large scale structures. This is the reason why CVS is not only capable of recognizing the main ocean circulation patterns, but also of stressing those regions for which rotation is dominant [33, 13]. It has been reported that in DNS the modes corresponding to the coherent part represent only about 2% of the total number of modes, and they lead to a description which is accurate up to 99% of the total enstrophy of the flow. However, in a previous work it has been shown that CVS in the framework of physical oceanography - there named as Coherent Vortex Separation - is less efficient than on DNS [128]. This lower performance is thought to be a consequence of the way in which the method is conceived, namely, it is centered on some assumptions on the statistics of the flow (Donoho & Johnstone's criterion [27]) that are not accurate in the context of real, non-homogeneous turbulence. Some physical conditioning according to the properties of the underlying flow has to be introduced, as the statistics of general turbulent flows are strongly non-Gaussian, even for the incoherent part. The incoherent part cannot be considered as noise, but represents the unsolved scales. Once the multifractal character of altimetry images is demonstrated from the study shown in the first part of the article, these properties will be used to adapt CVS for satellite data and presented straight afterwards. From now on, to avoid misunderstandings, we will use CVE (Coherent Vortex Extraction) instead of CVS when no simulation is involved.

The outline of this paper is structured as follows. First, MMF and the consequences of having a multiplicative cascade established on scalar variables are described in the theoretical Section 6.2. Second, CVE technique is presented in Section 6.3. Then, a description of the data employed for the empirical part of this study is given Section 6.4. Section 6.5 is devoted to the presentation of the experimental validation of MMF on our data, while Section 6.6 discusses different implementations of CVE which take MMF into account. Finally, conclusions are given in Section 6.7.

6.2 Microcanonical Multifractal Formalism

MMF arises from the general theory of FDT and more specifically from Kolmogorov's theory, as a way to provide a precise geometrical representation of turbulence. In many statistical studies on turbulence, flow organization has been analyzed based on the characterization of its structure in terms of global quantities. They are statistical averages of some dynamical variables. This is generally performed with the study of the local structure functions of order p and size l, which is denoted by $S_p(l)$. These functions are just the order-p moments of an intermittent, positive, intensive variable $\epsilon_l(\vec{x})$, where $\vec{x}$

denotes a point in the domain space. Common choices for ϵ_l in the classic literature include linear increments of the modulus of the velocity along a given direction,

$$\epsilon_l(\vec{x}) \;=\; |v(\vec{x}) - v(\vec{x}+\vec{l})| \tag{6.1}$$

or local energy dissipation on balls of radius l,

$$\epsilon_l(\vec{x}) \;=\; \sum_{ij} \int_{B_l(\vec{x})} d\vec{x} \;\; (\partial_i v_j(\vec{x}\,) \;+\; \partial_j v_i(\vec{x}\,))^2 \tag{6.2}$$

but many other definitions are also possible. Of particular interest is the case of scalar variables (tracers) submitted to the action of a turbulent flow. It has been argued that the scaling properties of some scalars can be related to those of the underlying flow [66], although sometimes important differences may be found depending on the type of tracer considered [68]. For a tracer $s(\vec{x})$, the simplest type of tracer-derived scaling variable ϵ_l is given again by its linear increments,

$$\epsilon_l(\vec{x}) \;=\; |s(\vec{x}+\vec{l}) - s(\vec{x})| \tag{6.3}$$

However, linear increments are ill behaved in many practical situations due to the presence of noise (which would mask short-range scaling) and of long-range correlations (like sunglint or large area wind-effects, which would mask long-range scaling). For this reason, it is convenient to work with continuous wavelet projections of the tracer, which allow to filter out long-range correlations [5, 4] and to provide a stable interpolation scheme [132, 138]. Hence, the variable ϵ_l will be given by:

$$\epsilon_l(\vec{x}) \;=\; |T_\Phi s(\vec{x}, l)| \tag{6.4}$$

where the continuous wavelet transform $T_\Phi s(\vec{x}, l)$ of the tracer s projected on the wavelet Φ at the point $\vec{x}$ and the scale l is given by:

$$T_\Phi s(\vec{x}, l) \;\equiv\; \int d\vec{y}\; s(\vec{y}) \frac{1}{l^d} \Phi\left(\frac{\vec{x}-\vec{y}}{l}\right) \tag{6.5}$$

where d represents the dimension of the domain space ($d = 2$ in 2D scalars). In general, the wavelet Φ must verify some requirements in order to be valid to assess the scaling behavior of the system. This discussion exceeds the limits of this paper; the interested reader is referred to [5, 4, 132, 135] for the details. The use of tracers and, more specifically, of wavelet transforms of tracers in order to assess the scaling properties of a turbulent flow is the most common situation, because direct measurements of the velocity vector are difficult to obtain in general; in contrast, direct measurements of many tracers are usually available.

Once the variable ϵ_l of choice has been defined, its associated structure functions are given by:

$$S_p(l) \;=\; \langle \epsilon_l^p \rangle \tag{6.6}$$

According to Kolmogorov's theory [62, 61] in the inertial range these statistical stationary quantities must depend on the scale l as a power law. Assuming this relation, the multi-scaling exponents τ_p are defined according to the following relation:

$$S_p(l) \;\propto\; l^{\tau_p} \quad ; \quad l \ll 1 \tag{6.7}$$

Kolmogorov also pointed out that all the scaling exponents τ_p must have a linear dependence on the order p, the *linear scaling*:

$$\tau_p \;=\; H\, p \;+\; \beta \tag{6.8}$$

where the coefficient H is given by the scaling properties of the maximum of ϵ_l,

$$\max_{\vec{x}} \; \epsilon_l(\vec{x}) \;\propto\; l^H \quad ; \quad l \ll 1 \tag{6.9}$$

and the coefficient β is related to the behavior of the support of ϵ_l (*i.e.*, the set where ϵ_l is different from zero), in the way:

$$l^\beta \;\propto\; S_0(l) \;=\; \int d\vec{x} \;\; 1_{\epsilon_l(\vec{x}')=0} \tag{6.10}$$

According to Kolmogorov's model of linear multi-scaling exponents, all the energy is concentrated in a set, of fractal character, to which all the points contribute exactly the same amount of energy, namely l^H. It follows that for any two scales $l < L$, the variable ϵ_l results from:

$$\epsilon_l \doteq \eta_{\frac{l}{L}}\, \epsilon_L \tag{6.11}$$

where the symbol $\doteq$ means that both sides have the same distribution, and the factor $\eta_{\frac{l}{L}}$ works at a constant rate that depends on the ratio of scales $\frac{l}{L}$: $\eta_{\frac{l}{L}} = (\frac{l}{L})^H$.

The process in which there are energy transfers from larger toward smaller scales is called the down-scaling cascade, while in the other sense we can speak about up-scaling cascade process. We will concentrate our discussion on the down-scaling process, but the mechanisms that describe the up-scaling process are essentially the same. They only depend on the convexity of τ_p [44].

Equation (6.10) implies that the support of ϵ_l must have a fractal character; in fact, we can easily relate the scaling exponent β with the fractal dimension D of the support. When observed at a scale l, the fraction of space occupied by the support scales as l^{d-D} [32]. Hence, comparing with Equation (6.10) we have $D = d - \beta$. Hence, we conclude that Kolmogorov's linear scaling implies having a single fractal energy interface.

Unfortunately, Kolmogorov's linear scaling is not in accordance with experimental results. Experiments [6] show that in general τ_p presents *anomalous scaling* (in opposition to the *normal* Kolmogorov's regime) [2, 37]. The curvature of τ_p, as a function of p, can only be explained in terms of a multiple fractal model. In order to describe this curvature, the cascade variable $\eta_{\frac{l}{L}}$ cannot be any longer considered as a constant, but as a random variable independent from ϵ_L that follows a distribution completely defined by τ_p. In order to obtain a consistent definition, the cascade variable must verify the cascade relation, formulated as follows: for any arbitrary intermediate stages l , $l < l\ < L$, the following identity must hold:

$$\eta_{\frac{l}{L}} \doteq \eta_{\frac{l}{l'}} \eta_{\frac{l'}{L}} \tag{6.12}$$

This means that the cascade process leads to the same result independently of the number of intermediate stages taken to go from scale L to scale l. In essence, Equation (6.12) implies that all the scales involved by the cascade must be in dynamical equilibrium.

Thanks to Parisi & Frisch's contribution in 1985 we can now interpret the scaling of the cascade in turbulence in terms of a composite of scaling fractal objects with more physical meaning. Parisi and Frisch [105] established a link between the statistical formalism and an underlying geometrical arrangement of multiple fractal components. Their key hypothesis is that the points in the support of the studied dynamical variable do not share a single value of scaling exponent H as in Kolmogorov's theory. Instead, the support has to be broken in different singularity components F_h, each one associated to a particular value h of scaling exponent. These components (also called *fractal manifolds*) will have different (Hausdorff) fractal dimensions $D(h)$. When the dimensions $D(h)$ of the components are represented as a function of h, we will talk about the *singularity spectrum* of the multifractal. The singularity spectrum $D(h)$ can be easily calculated from the distribution of scaling exponents h obtained when the variable ϵ_l is processed at a given scale l [32]:

$$\rho_l(h) \;\propto\; l^{d-D(h)} \tag{6.13}$$

According to Parisi and Frisch's derivation, the multiscaling exponents τ_p are immediately related to the singularity spectrum, in the way:

$$\tau_p \;=\; \inf_h \{ph \;+\; d \;-\; D(h)\} \tag{6.14}$$

The multiplicative cascade given by $\eta_{\frac{l}{L}}$ is a consequence of the existence of a hierarchy of fractal components, which is described by its singularity spectrum. Assuming that $D(h)$ is convex, the Legendre transform in Equation (6.14) can be inverted and the singularity spectrum is calculated from the multi-scaling exponents; namely:

$$D(h) \;=\; \inf_p \{ph \;+\; d \;-\; \tau_p\} \tag{6.15}$$

Although geometrically appealing, Parisi and Frisch's derivation is in fact a statistical derivation and hence it is at the root of many statistical studies on the multifractal properties of different systems [96, 8, 7, 97]. All these approaches can be included in the so-called Canonical Multifractal Formalism (CMF). MMF supposes an important step forward, as it offers a way to assign to each point $\vec{x}$ in the domain space a value of local scaling exponent $h(\vec{x})$ of a given scaling variable $\epsilon_l(\vec{x})$, in the way:

$$\epsilon_l(\vec{x}) \;=\; A(\vec{x})\, l^{h(\vec{x})} \;+\; o\left(l^{h(\vec{x})}\right) \tag{6.16}$$

where the notation $o\left(l^{h(\vec{x})}\right)$ means a term which is negligible in comparison to $l^{h(\vec{x})}$ when l goes to zero. Not all the possible definitions of $\epsilon_l(\vec{x})$ would lead to a local singularity exponent, as the one given in Equation (6.16), and so an appropriate definition must be searched. This is one of the requirements of MMF; let us enunciate here the three requirements for having MMF in a system [55, 138]:

i) Each fractal component is scale-invariant: for any point $\vec{x}$, Equation (6.16) is verified over a large enough range of scales l.

ii) The whole multi-fractal hierarchy is scale-invariant: the distribution of singularities at any valid scale l follows Equation (6.13), for the same function $D(h)$.

iii) The function $D(h)$ derived from Equation (6.13) is convex. So that, Equation (6.14) can be inverted to retrieve $D(h)$ and so the Canonical approach is also valid. We can thus conclude that the multiplicative cascade is developed in the flow. This would validate the hypothesis of a turbulent origin flow driving the scalar.

We will show the validity of MMF on our dataset in Section 6.5.

6.3 Coherent Vortex Extraction

Coherent Vortex Simulation, CVS, is a method developed by Marie Farge and co-workers [33, 35, 34, 13] for analyzing FDT flows and describing them in a compact manner. To do so, the vorticity field is split into two contributions: a coherent part, which own to the organized flow, and a incoherent part that is associated to a random background flow. This method is based on the vortex extraction algorithm, CVE. The vorticity field is appropriate to detect areas of strong gradients - that are associated to the non-linear interactions - as well as for its topological and Galilean invariance properties. The separation is done in terms of wavelet coefficients in which the vorticity field is decomposed. A multi-scale scheme is necessary to extract all the active scales of coherent structures. A wavelet basis, optimal for the particular data under study, must be chosen.

In order to decompose vorticity in terms of a multiscale, wavelet representation, vorticity has been represented in a 2D dyadic orthonormal basis of mother wavelets $\{\psi_r\}_{r=1,2,3}$:

$$\omega(\vec{x}) \;=\; \sum_{r=1,2,3}\sum_{j=1}^{J}\sum_{\vec{k}} \alpha_{rj\vec{k}}\;\psi_{rj\vec{k}}(\vec{x}) \tag{6.17}$$

where $\psi_{rj\vec{k}}(\vec{x}) = 2^{-j}\psi_r(2^{-j}\vec{x} - \vec{k})$, r is the index which characterizes the orientation of the mother wavelet, 2^j is the dyadic scale (measured in pixels or resolution points), $2^j\vec{k}$ represents the spatial location with $\vec{k} = (k_1, k_2)$; and j, k_1, k_2 are integer numbers. The sum on scales goes from the finest, best resolving scale $j = 1$ to the coarsest, worse resolving integral scale $j = J$. As the wavelet basis is assumed to be orthonormal, the wavelet coefficients are obtained by simple projection $\alpha_{rj\vec{k}} = \langle\psi_{rj\vec{k}}, \omega\rangle$ [23].

The computation of CVE is centered on the selection of those coefficients retained according to Donoho & Johnstone's criterion [27], which are supposed to represent those regions with the most significant vorticity values. The threshold value Θ is established as:

$$\Theta \;=\; 2\sqrt{ZlnN} \tag{6.18}$$

with Z the total enstrophy, $Z = \frac{1}{2}\langle\omega, \omega\rangle$ and N is the number of data points at the studied resolution (the total number of pixels).

Once Θ is known, the vorticity field can be broken in two terms, the coherent part ω_c and the incoherent one ω_i:

$$\omega \;=\; \omega_c \;+\; \omega_i \;=\; \sum_{\alpha_{rj\vec{k}} > \Theta} \alpha_{rj\vec{k}}\;\psi_{rj\vec{k}}(\vec{x}) \;+\; \sum_{\alpha_{rj\vec{k}} \leq \Theta} \alpha_{rj\vec{k}}\;\psi_{rj\vec{k}}(\vec{x}) \tag{6.19}$$

Farge et al. reported that for DNS of homogeneous 2D turbulence the coherent part only contains a small number of degrees of freedom of the system (less than 2%). This way, the compression is noteworthy and the computational cost is significantly reduced. On the other hand, the effect of the discarded modes comprised in the incoherent part was observed to be statistically distributed according to a Gaussian PDF with small standard deviation, and thus they were regarded as negligible.

By construction, as a consequence of the orthogonality of the wavelet basis, the vorticity field becomes divided into two orthogonal components, i.e., $\langle \omega_c, \omega_i \rangle = 0$. Due to Parseval's identity, the total enstrophy can be also separated in the same way as the vorticity: $Z = Z_c + Z_i$.

The associated coherent and incoherent velocity fields can be retrieved by applying Biot & Savart's kernel:

$$\vec{v} = \nabla \times (\Delta^{-1}\omega) \tag{6.20}$$

The decomposition of the velocity field is only approximately orthogonal because Biot & Savart's kernel projected on an orthonormal wavelet basis is almost diagonal. Then, we have $\langle v_c, v_i \rangle \neq 0$ despite the fact that $v = v_c + v_i$. Thus, the coherent and incoherent energies are not additive: $E \neq E_c + E_i$, where $E = \frac{1}{2}\langle v^2 \rangle$, $E_c = \frac{1}{2}\langle v_c^2 \rangle$ and $E_i = \frac{1}{2}\langle v_i^2 \rangle$.

CVE was initially applied to filter DNS data, for instance, of a 2D turbulent homogeneous and isotropic flow [33, 13]. However, only recently CVE has been applied to altimetric data [128] with significant results. The reason supporting the application of CVE to geophysical data is the frequently argued similitude of 2D and geophysical turbulence. Notice that CVE has also been applied to laboratory data, e.g., [112], and the results confirm the adequacy of this approach as well. In [33, 13], different Reynolds numbers were considered depending on the number of retained modes. By using 256×256 grid points and a kinematic viscosity of about $10^{-5} m^2 s^{-1}$, the Reynolds number does not take values larger than few thousands. In those experiences, around 99% of the total energy and enstrophy are represented by selecting only 2% of the total wavelet modes for the coherent field. However, in the more realistic case of a altimetry-derived ocean vorticities, about 1/3 of the energy and 15% of the enstrophy were lost. In this context, 36×36 grid points (separated about 1/3 of degree) were used and Reynolds numbers was about 10^8. This number is obtained after assuming characteristic velocities and lenght scales of $0.1 m s^{-1}$ (open ocean) and 40 km (1/3 of degree), respectively, as well as a kinematic fluid viscosity of $10^{-6} m^2 s^{-1}$. The lost of energy and enstrophy is mainly due to the fact that coherent structures are defined as local condensations of the vorticity field, and vortices are something more than vortex cores. Vorticity concentrations cannot be just considered as simple separable 'atoms'. Vortices are sometimes elongated - stretched and folded - during the interaction with other structures. Therefore, there is a significant part of the eddy field that is contained in the incoherent component. Furthermore, by only taking vortices, we are loosing some other coherent structures like streams and filaments that are not directly related to eddies. This is consistent with the observation that the presumed incoherent background field does not present a Gaussian distribution in the case of altimetry-derived oceanic flows for any percentage of selected modes in the coherent part [128]. In sum-

mary, there is a part of ocean motion that cannot be explained by the naive CVE picture.

It is hence evident that some aspects in CVE need to be developed in order to better approximate the particularities of SLA maps. First of all, an improvement of the criterion to fix the threshold used in the separation is mandatory, taking into account the strong deviation from Gaussianity of oceanic flows [54]. A criterion with physical significance should be implemented. Another point that requires some study concerns the influence of boundary conditions represented by coastlines, which produce sharp transitions in data. In order to avoid this problem, open sea areas have been chosen for the present study, but coastal regions will be analyzed in future works. Finally, the performance of the different wavelet bases are not the same, so we have tested different representation bases in order to decide which wavelet basis best adapts to the particularities of oceanographic data.

6.4 Data description

In this study we have used about 50 Delayed-Time maps of Sea Level Anomaly from TOPEX/Poseidon altimeter corresponding to several months in 1997 produced at intervals of 10 days by CLS, Toulouse, and available through AVISO server (http://las.aviso.oceanobs.com/las/servlets/dataset). These images are regularly produced by subtracting a temporal average (1993-1999) and gridded into $1/3 \times 1/3$ degrees by using a suboptimal space/time objective analysis that considers long wavelength errors [72]. They have been pre-processed including usual corrections (sea-state bias, tides, inverse barometer, etc.) and improved in combination with ERS orbits, which has a repeat cycle of 35 days. Data are also filtered using a 35 km median filter and a Lanczos filter with 42 km of cutoff to reduce noise. Filtering data is convenient in order to obtain regularly shaped maps, but can cause a lost of information. There is a limitation in the capabilities of our study to describe the cascade toward smaller scales despite SLA maps are really useful to determine mesoscale structures and their spatio-temporal variability. We will discuss this issue in the next section.

If we denote by h the SLA map, the velocity field has been estimated from these data under the geostrophic approximation:

$$u = -\frac{g}{f}\frac{\partial h}{\partial y},\ v = \frac{g}{f}\frac{\partial h}{\partial x} \tag{6.21}$$

where g the gravity and f the Coriolis parameter. The vorticity $\vec{\omega}$ associated to the velocity field is then:

$$\vec{\omega} \;=\; \nabla \times \vec{v} \tag{6.22}$$

with only one non-null component $\omega \equiv \omega_z = \partial_x v - \partial_y u$ in a 2D flow.

For the purposes of the present study, we have concentrated on an open sea area in the North Atlantic. The scenario under study is located surrounding the Gulf Stream area, which covers from 60 to 17.5 degrees West in longitude, and from 9.5 to 46 degrees North in latitude. Due to the limited resolution of SLA data, this defines a relative small grid of 128 $\times$ 128 points.

6.5 MMF on altimetric data

To verify the validity of MMF on altimetric data, the three conditions presented in Section 6.2 must be checked. Our local intensive variable ϵ_l will be defined as the wavelet transform of SLA-derived vorticity, according to Equations (6.4) and (6.5) where s is substituted by ω. We will not consider all the possible continuous wavelet projections of ω, but just those given by the pyramidal dyadic scheme. This is, $l = 2^j$ pixels and $\vec{x} = 2^j\vec{k}$, where j, k_1, k_2 are integer numbers. According to the notation introduced in Section 6.3, these projections correspond to the variables $\alpha_{rj\vec{k}}$ defined in eq. (6.17). Notice, however, that in order to apply the formulas presented in Section 6.2 we need to express all the distances and scales in physical units, not in resolution-dependent (*i.e.*, pixel) units. Conventionally assigning a unit physical scale to the scale J (which represents the integer scale in our system), we have that $l = 2^{-(J-j)}$ and $\vec{x} = 2^{-(J-j)}\vec{k}$ when expressed in physical units.

Due to the limited resolution of SLA data and the small size of the studied areas, having a large enough range of scales to determine the accuracy of condition i) is very difficult in our case. This problem can easily be evidenced by the power spectrum of the vorticity. As the vorticity is the derivative of the velocity, if the power spectrum of the velocity scales with the spatial wave number k as k^{-2+} (where $\in = 1/3$ in fully developed turbulence), then the power spectrum of the vorticity must scale as k . In Figure 6.1 we present three log-log plots of the velocity and the vorticity power spectra. As intended, the plot scales linearly for small frequencies, but at high frequencies (small scales) the spectrum decays very fast. This is a consequence of the low-pass filtering applied to the data, which makes the effective resolution of the data coarser than the nominal one. So,

as discussed, we are limited to very few scales. In addition, the interpolation scheme applied to the maps seem to have also affected the slope at low frequencies, so $\in= 1$ in contrast with the $\in= 1/3$ predicted for turbulence.

Due to this constraint, we have preferred to obtain punctual estimates of the singularity exponents h at each location, following previous works [135, 109]. Punctual estimates are obtained by taking logarithms on Equation (6.16) and neglecting the terms on the right hand side other than $h(\vec{x}) \log l$. So that, we define the punctual estimate of the singularity exponent $h_{rj\vec{k}}$ along the orientation r at the scale j and position $\vec{k}$ as:

$$h_{rj\vec{k}} \;=\; \frac{\log\left(\frac{\alpha_{rj\vec{k}}}{\alpha_{rj\cdot}}\right)}{(j-J)\log 2} \tag{6.23}$$

where $\langle \alpha_{rj\cdot} \rangle$ means the average of $\alpha_{rj\vec{k}}$ across all the possible values of $\vec{k}$ with fixed orientation r and scale j obtained from a given vorticity field ω. As punctual estimates are obtained considering a single scale only, they are less affected by the upper and lower cutt-offs of the inertial range. However, the validity of Equation (6.23) lies on having a scale $l = 2^{-(J-j)}$ small enough so that the correcting terms could be neglected; besides, the validity of Equation (6.16) cannot directly be verified. So, we must plainly accept that i) is verified as far as the other two conditions are verified.

To verify ii) and iii), we will obtain an estimate of the singularity spectrum at each scale j, as in [135, 109]. Let $\rho_{rj}(h)$ be the distribution of singularity exponents $h_{rj\vec{k}}$ for the orientation r and scale j. Given that there is always a fractal component F_{h_1} of maximal dimension d, it corresponds to the maximum of $\rho_{rj}(h)$. Hence, normalizing the distribution by its maximum value $\rho_{rj}(h_1)$ and applying Equation (6.13), we can derive an estimate for the singularity spectrum as:

$$D_{rj}(h) \;=\; d \;-\; \frac{\log\left(\frac{\rho_{rj}(h)}{\rho_{rj}(h_1)}\right)}{(j-J)\log 2} \tag{6.24}$$

As shown in Figure 6.2, the functions $D_{rj}(h)$ obtained for the different orientations r, scales j and wavelet bases correspond to the same convex function $D(h)$. For a given orientation and wavelet basis and varying j, the fact that the different $D_{rj}(h)$ give rise to the same function $D(h)$ proves that condition ii) holds. Besides, as $D(h)$ is convex, condition iii) also holds. The fact that the different orientations lead to the same $D(h)$ evidences that the multiplicative process is isotropic. We have also tried different wavelets bases (Daubechies $p = 3$, Daubechies $p = 6$, Haar, Coiflet $p = 1$, Symmlet

$p = 4$, and Battle-Lemarié $p = 3$). However, any of them leads to the same $D(h)$, what proves that this function is a universal property. The parameter p here refers to the degree of derivability or the interpolation order of the wavelet. Notice that projecting on Haar bases is equivalent to taking finite increments. Thus, the correspondence of spectra obtained with this basis implies that the results using more classical approaches, as structure functions [37], are equivalent to those obtained with more sophisticated wavelets.

From here on, it can be concluded that SLA verify all the requirements of the micro-canonical multifractal formalism in a good extent.

Having demonstrated the existence of a multifractal hierarchy, the cascade expression, Equation (6.11) can be used to relate the wavelet coefficients of the signal from the different scales. For the discretized dyadic coefficients this relation reads [133]

$$\alpha_{rj\vec{k}} \doteq \eta_{rj\vec{k}}\, \alpha_{r,j+1,\left[\frac{\vec{k}}{2}\right]} \tag{6.25}$$

where the notation $\left[\frac{\vec{k}}{2}\right]$ means the vector with components the integer part of those of $\frac{\vec{k}}{2}$. The wavelet coefficients $\alpha_{r,j+1,\left[\frac{\vec{k}}{2}\right]}$ represent the contribution to the wavelet projection at the immediately coarser scale $j+1$ and about the same position as that of coefficient $\alpha_{rj\vec{k}}$; it is hence called the *father coefficient* [19] associated to $\alpha_{rj\vec{k}}$, which it is one of its children coefficients. In 2D, each father has four children; see Figure 6.3.

Although Equation (6.25) is only a statistical equality and hence does not imply a point-by-point correspondence, in general, it can be assumed that such a correspondence is a good approximation for many wavelets. We will then define the ratio between a child and its father $\eta_{rj\vec{k}}$ by simply isolating in Equation (6.25), as if it holds point-by-point,

$$\eta_{rj\vec{k}} = \frac{\alpha_{rj\vec{k}}}{\alpha_{r,j+1,\left[\frac{\vec{k}}{2}\right]}} \tag{6.26}$$

This will be a good approximation for the purpose of this study if the wavelet chosen is almost optimal. Notice that the scale ratio l/L is always $1/2$ for any two compared scales. This implies that all the variables $\eta_{rj\vec{k}}$ must be equally distributed. They should also be independent from the variables $\alpha_{r,j+1,\left[\frac{\vec{k}}{2}\right]}$. In fact, this property will be only approximate except for a particular wavelet, known as optimal wavelet, if it exists [133]. We will apply this knowledge in order to improve the results from CVE in the oceanographic context.

6.6 Adaptive CVE on SLA maps

In Section 6.3 we have seen that a direct application of CVE for the analysis of ocean dynamics, and particularly on altimetry maps, is rather unsatisfactory. As discussed, although D&J's threshold is objective because it only depends on the total enstrophy and the resolution, this has to be improved so that it could take into account some physical properties of the flow. Our attempt will be centered on the implementation of a new criterion based on the multiplicative cascade and thus adapted to the local properties of the flow

For either of the methods we are going to introduce, we have used Battle-Lemarié basis because this wavelet basis is the best adapted to altimetry data, as shown in [128], although it has not a compact support and some unwanted neighborhood influence could occur. Anyway this basis behaves particularly well for data that need to be smoothly interpolated, e.g., altimetric products. Notice that the same choice was made in [33] and in [128]. Let us also remark that the main methodological improvement of this work is not related to the kind of wavelet we choose, but to the adaption of the threshold to local variability. The key point is finding a threshold adapted to the local properties of vorticity and physically meaningful. The global criterion does not work in systems in which the vortices are presented in a wide range of scales, so a local criterion must be searched.

6.6.1 Global and local thresholds

According to the standard formulation of the CVS technique [33], the incoherent part should be a random, Gaussianly distributed field. As a refinement, if D & J's criterion leads to a non-Gaussian incoherent part the threshold may be reduced until the obtained incoherent part verifies some tests proving its Gaussian character [13]. However, as was shown in [128], when considering altimetry-derived vorticity fields the incoherent part is never Gaussian, so the threshold would decrease to zero and no coherent-incoherent separation will be produced. This means that, disregarding the value of the threshold, dynamics is never well described for a moderate number of modes in the coherent part. To avoid this problem and at the same time to fix a reference able to compare the different methods, we have decided to fix the amount of number of wavelet modes to be kept with the different methods. Hence, we have fixed the fraction f of retained wavelet modes for each method.

The simplest extension of D & J's criterion under this constraint is to search for a constant threshold θ^f such that a fraction f is kept. As usual, only those wavelet

coefficients $\alpha_{rj\vec{k}}$ which are greater in absolute value than θ^f will be selected by the coherent part. We call this criterion *Global Threshold*. The value $f = 0.01$ roughly corresponds to the value of D & J's threshold, and so similar percentages of enstrophy and kinetic energy are obtained. However, a Global Threshold has the same global character as D & J's threshold and hence it does not take the local influence of structures into account; as a consequence, at some areas deviations are important.

To define a local criterion is a bit more complex. For each fixed scale j, orientation r, and fraction of selected modes f, a local threshold $\theta^p_{rj\vec{k}}$ must be obtained at each position $\vec{k}$. In this way, it is taken into account the influence of the neighbour wavelet coefficients leading to the given fraction f of selected wavelet coefficients. We take a local surrogate of D & J's threshold as starting point: for each position $\vec{k}$ at the layer of scale j and orientation r, we define a local neighbourhood of size N_{jr} and we evaluate the local enstrophy $Z_{rj\vec{k}}$ on it. In analogy to the standard D & J's criterion, we take the value $2\sqrt{Z_{rj\vec{k}} \ln N_{rj}}$ as reference for that point. The local threshold $\theta^f_{rj\vec{k}}$ is defined as:

$$\theta^f_{rj\vec{k}} \;=\; \lambda^f \, 2\sqrt{Z_{rj\vec{k}} \ln N_{rj}} \tag{6.27}$$

where λ^f is a global variable with the appropriate value such that only a fraction f of wavelet coefficients is selected. Recall that a wavelet coefficient $\alpha_{rj\vec{k}}$ will be selected as coherent if $|\alpha_{rj\vec{k}}| > \theta^f_{rj\vec{k}}$.

We have defined two different types of local threshold. We call the first one *Windowed Threshold*. With this criterion we take the window of size $(2\Delta + 1) \times (2\Delta + 1)$ centered around each point $\vec{k}$ in the layer of scale j and orientation r, and the local enstrophy $Z_{rj\vec{k}}$ is obtained by a uniform weighting of all the points in the window:

$$Z_{rj\vec{k}} \;=\; \frac{1}{(2\Delta+1)^2} \sum_{m_1,m_2=-\Delta}^{\Delta} \frac{\alpha^2_{rj,\vec{k}+\vec{m}}}{2} \tag{6.28}$$

and the value of N_{rj} to be substituted in eq. (6.27) corresponds to the window size, $N_{rj} = (2\Delta + 1)^2$.

The expression above can be generalized to the case in which a non-uniform weighting is introduced. As before, we take a $(2\Delta + 1) \times (2\Delta + 1)$ window centered around each

point $\vec{k}$ in the layer of scale j and orientation r, and the local enstrophy $Z_{rj\vec{k}}$ is obtained by a weighting of all the points in the window, in the way

$$Z_{rj\vec{k}} = \frac{1}{A} \sum_{m_1,m_2=-\Delta}^{\Delta} w_{\vec{m}} \frac{\alpha^2_{rj,\vec{k}+\vec{m}}}{2} \tag{6.29}$$

where A is the normalization factor,

$$A = \sum_{m_1,m_2=-\Delta}^{\Delta} w_{\vec{m}} \tag{6.30}$$

and the weights $w_{\vec{m}}$ are non-negative values. We have studied a particular case of weighting, similar to the one used in [43]: the multiscale weighting, given by

$$w_{\vec{m}} = \frac{1}{|\vec{m}|^2} \tag{6.31}$$

when $\vec{m} \neq 0$, and $w_0 = 0$. We have implemented the local threshold associated to this weighting that we have called *Multiscale Threshold*.

In Figure 6.4 we show examples of the application of the Global Threshold, Windowed Threshold, and Multiscale Threshold, for $f = 0.10$ using a $p = 3$ Battle-Lemarié basis and 31-pixel wide windows for the two local thresholds. The coherent enstrophies and energies, expressed as percentages of the total enstrophy and energy, are presented in Table 6.1. Results for windowed and multiscale thresholds show slightly smaller percentages of explained energies and enstrophies than global threshold. However, looking at Figure 6.4 we can notice how small scales are better represented with the local definitions.

6.6.2 Singularity threshold

The next step was to design a criterion related to the existence of a cascade and to the pertinence of MMF to describe SLA data. In both algorithms the separation is done iteratively scale by scale and differentiating each orientation (the horizontal, vertical and diagonal details).

It has been argued that the most singular events in the multifractal hierarchy (*i.e.*, smallest values, which correspond to the greatest values of $\alpha_{rj\vec{k}}$ due to the sign inversion in Equation (6.23)) carry enough information to retrieve the signal completely [118, 119]; in fact, an explicit geometric algorithm to reconstruct a signal from the set of most singular points was designed in [126], with good performance in practical situations [129, 127]. Hence, we have designed a threshold intended to retain only the most singular punctual singularity exponents $h_{rj\vec{k}}$. To select these exponents, a threshold exponent h_θ must be chosen; hence, this kind of threshold acts similarly to the global D & J's threshold. However, as follows from Equation (6.23), the value of the exponent is normalized at each scale and orientation with respect to its average reference level, and the absolute value of the singularity decays when the resolution increases, i.e., when j decreases. This gives a more balanced interplay among the different scales.

The *Singularity Threshold* criterion is defined as follows: a wavelet coefficient $\alpha_{rj\vec{k}}$ will be selected for the coherent part if the associated value of singularity $h_{rj\vec{k}}$ is *smaller* than a threshold value h^f; as before, the value of h^f is fixed according to the fraction f of wavelet modes that will be selected. Results of the application of this criterion are shown in Table 6.1 and Figure 6.5.

In Figure 6.6 a comparison of the global performances of all the presented methods for different values of f is given. Global Threshold gives the best global results. Nevertheless, it is not based on any physical criterion or gives a balanced representation of the fields. Only the strongest structures are well represented and many areas with important structures of medium intensity appear empty. Local thresholds (Windowed and Multiscale) give the best balanced geometrical representation of the fields, but at the cost of noticeably diminishing the global performances: the global enstrophies and energies of the coherent parts obtained with this methods are always below those of the global threshold. Only the Singularity Threshold attains a good local representation of structures and a global performance almost as good as the one by Global Threshold, except for very small values of f in which the global enstrophy is considerably lowered. We hence conclude that the singularity threshold is the method with the best balanced performance.

6.6.3 Beyond locally orthogonal criteria

All the methods presented so far lead to coherent and incoherent parts that are orthogonal in a strong sense, i.e., for each r, j and $\vec{k}$ we have:

$$\alpha^c_{rj\vec{k}} \cdot \alpha^i_{rj\vec{k}} = 0 \tag{6.32}$$

which is quite obvious, because if a wavelet coefficient is included in the coherent part it is not included in the incoherent part and vice-versa. Consequently the coherent and incoherent vorticities are mutually orthogonal:

$$\langle \omega_c, \omega_i \rangle \;=\; \int d\vec{x}\; \omega_c(\vec{x})\omega_i(\vec{x}) \;=\; \sum_{r=1,2,3} \sum_{j} \sum_{\vec{k}} \alpha^c_{rj\vec{k}} \,.\, \alpha^i_{rj\vec{k}} \;=\; 0 \tag{6.33}$$

Although orthogonality between the coherent and the incoherent parts is a desirable property of a properly designed separation scheme, it could be formulated as a weaker property. It is not necessary that the coherent and the incoherent wavelet modes are orthogonal at each r, j and $\vec{k}$, but just as a combination. A separation of this kind will also be more physically reasonable, because if the incoherent part behaves like noise it should affect all wavelet modes equally and hence attributing the whole wavelet mode to the coherent part, while there is a contribution by noise, can be justified if the amplitude of the "noise" is small enough. However, if the noise-like incoherent component is not of so-small amplitude or has significant spatial correlations or we want to extract relatively weak coherent structures which may become stronger later on, we need to improve the separation scheme and just retain the part of the wavelet mode which can exactly be attributed to the coherent part.

The separation scheme could be based on the properties of the multiplicative cascade discussed in Section 6.2 and its explicit realization in a wavelet representation presented in Section 6.5. The idea will be trying to filter the variables $\eta_{rj\vec{k}}$ associated to the coherent contributions and substituting the others by some trivial proxy values. The idea is selecting the $\eta_{rj\vec{k}}$ with greatest value, reasoning out in a similar way to what was done in the previous criterion. The new variables associated to the coherent cascade, $\eta^c_{rj\vec{k}}$ will be given by:

$$\eta^c_{rj\vec{k}} \;=\; \begin{cases} \eta_{rj\vec{k}} & ; \quad |\eta_{rj\vec{k}}| \geq \eta_\theta \\ \bar{\eta}\; sign(\eta_{rj\vec{k}}) & ; \quad |\eta_{rj\vec{k}}| < \eta_\theta \end{cases} \tag{6.34}$$

where the proxy value $\bar{\eta}$ must be defined in order to produce a coherent part with an energy as close as possible to that of the original signal, and ensuring that the cascade process is stable. Notice that the coherent wavelet modes $\alpha^c_{rj\vec{k}}$ can be retrieved from

the cascade variables by the recurrent application of Equation (6.25); in fact, all the coefficients can be derived through a cascade from the integral wavelet modes α_{rJ0},

$$\alpha_{rj\vec{k}} = \prod_{j'=j}^{J} \eta_{rj'\left[2^{j-j'}\vec{k}\right]}\, \alpha_{rJ0} \tag{6.35}$$

Once the coherent wavelet coefficients $\alpha^c_{rj\vec{k}}$ are generated using the expression above, we build the coherent vorticity $\omega_c(\vec{x})$. The incoherent vorticity is derived by subtracting it from the original field: $\omega_i = \omega - \omega_c$. This criterion is simple, takes profit of the cascading processes in oceanic turbulence and is physically sound. However, determining the correct value of the proxy $\bar{\eta}$ is a hard task. The coherent part represents the main component of the total vorticity, but not the whole. For this reason, $\bar{\eta}$ cannot be adjusted just requiring that the coherent enstrophy equals the total enstrophy, because that choice of $\bar{\eta}$ leads to divergent cascades and an infinite coherent vorticity. Otherwise, too small values of $\bar{\eta}$ lead to decaying cascades which tend to produce vanishing coherent parts. Maybe the determination of $\bar{\eta}$ could be directed by enforcing the orthogonality between the coherent and the incoherent part. Additionally, assuming that the wavelet representation leads to an explicit cascade is just an approximation, as discussed in Section 6.5. In addition, due to the low-pass filters applied to SLA data the obtaining of the cascade variables $\eta_{rj\vec{k}}$ using Equation (6.26) may lead to divergences which should be treated. Work in these directions is still in progress.

6.7 Conclusions

In this article we have shown that the influence of ocean turbulence on SLA maps guarantees the validity of many symmetries which allow to simplify their study. All these properties, related to scale invariance and the existence of underlying cascade processes, can be summarized under the Microcanonical Multifractal Formalism (MMF). When an appropriate multiscale representation of SLA data is applied, as with wavelet decompositions, the microcanonical multifractal properties can be easily expressed in terms of equations relating the behavior of the wavelet modes across the different scales.

We have also reviewed the fundamentals of the Coherent Vortex Extraction technique, introduced to describe the behavior of homogeneous turbulence. In previous works [128] the standard CVE applied to oceanic turbulence, and particularly to altimetry data, was shown to have a considerably lower performance than for the study of laboratory experiments and computer simulations [33, 34, 13]. We have shown that the properties derived from the study of MMF on SLA maps can be combined with CVE, so giving

rise to new adaptive schemes in which some of the problems of standard CVE can be mitigated.

The essence of CVE consists in separating the vorticity field associated to a turbulent flow in two parts: the coherent part, dominated by the presence of mesoscale structures, and the incoherent part, in which no distinguished feature is observed and which behaves like noise. The coherent part is constructed by selecting the wavelet modes with an amplitude larger than a given threshold. The separation scheme is linear, so the total vorticity field can be retrieved as the sum of its coherent and incoherent parts. However, as oceanic turbulence is not homogeneous, it seems that a significant part of unsolved coherent modes are arbitrarily assigned to the incoherent part when the standard CVE is applied. In fact, even for low values of the threshold the problem persists and the incoherent part never becomes noise-like, what is evidenced for instance by the study of their PDFs, which are never Gaussian. These non-Gaussian components found using CVE are also not surprising considering that the data is low resolution, which implies underesolved Reynolds number, and that filtering and interpolation are applied. The new separation schemes, on the contrary, take into account the importance of local structures despite the poor quality of the data. For the more sophisticated of these criteria the value of a purely microcanonical multifractal variable, the local singularity, is used to determine if the wavelet mode should be considered coherent or incoherent. Results show that singularity-based thresholds attain the best balance between global and local description of flows within CVE. In this way, we could gather better the complexity of ocean turbulence, and describe circulation patterns with few degrees of freedom and using universal parameters.

The research line developed in this article opens the way to new studies on oceanic processes. For instance, CVE method could be applied to other kind of satellite data, even if they cannot be dynamically interpreted as straightforwardly as vorticity. Other satellite products such as Sea Surface Temperature (SST) or Chlorophyll Concentration (CC) offer the advantage of having higher resolution and greater accuracy. This means, dealing with variables less affected by filtering problems we could explore the information over a wider range of scales.

The strategy we expose is interesting to obtain valuable oceanographic information from satellite images. Nevertheless, this new methodology is also of application to other types of data as, for instance, numerical models of the ocean circulation. In fact, although our wavelet-based approach has been focused on satellite images, the proposed methods are flexible and valid for a 3D scope. Further analysis should be done in the future, and results could be compared with, for instance, 3D mixing layers [113]. All this combined could possibly help to effectively localize the most active parts of the main oceanic gyres, so simplifying our perception of the majority of the mechanisms taking

place in the ocean that control the physical-biologic processes and that at the same time respond to and affect the climatic system.

Criterion	D & J	Global	Windowed	Multiscale	Singularity
% Zc	58.41	94.33	81.85	77.12	81.24
% Ec	49.69	95.37	77.76	76.81	95.48

Table 6.1: Percentages of global coherent enstrophies and coherent energies obtained with the different criteria for the January 1$^{\text{st}}$ SLA map.

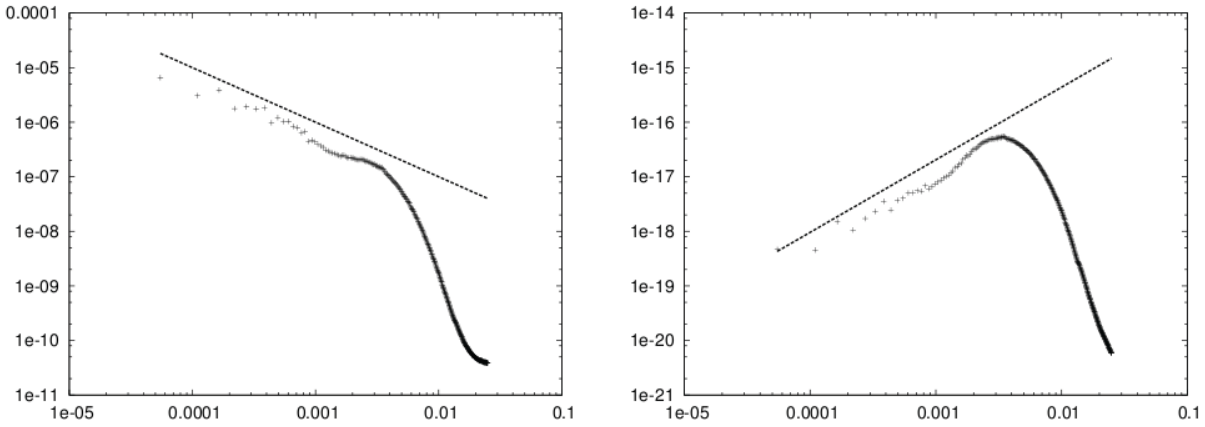

Fig. 6.1: **Left:** Velocity spectrum; **Right:** Vorticity spectrum. Both spectra are radial averages, and they have been obtained after processing all the dataset of SLA maps. The horizontal axes are given in inverse of wavelengths, expressed in km^{-1}; the vertical axes are given in m^2/s^2 for the velocity spectrum and in s^{-2} for the vorticity spectrm. The slopes of the guide straight lines are -1 and +1, respectively.

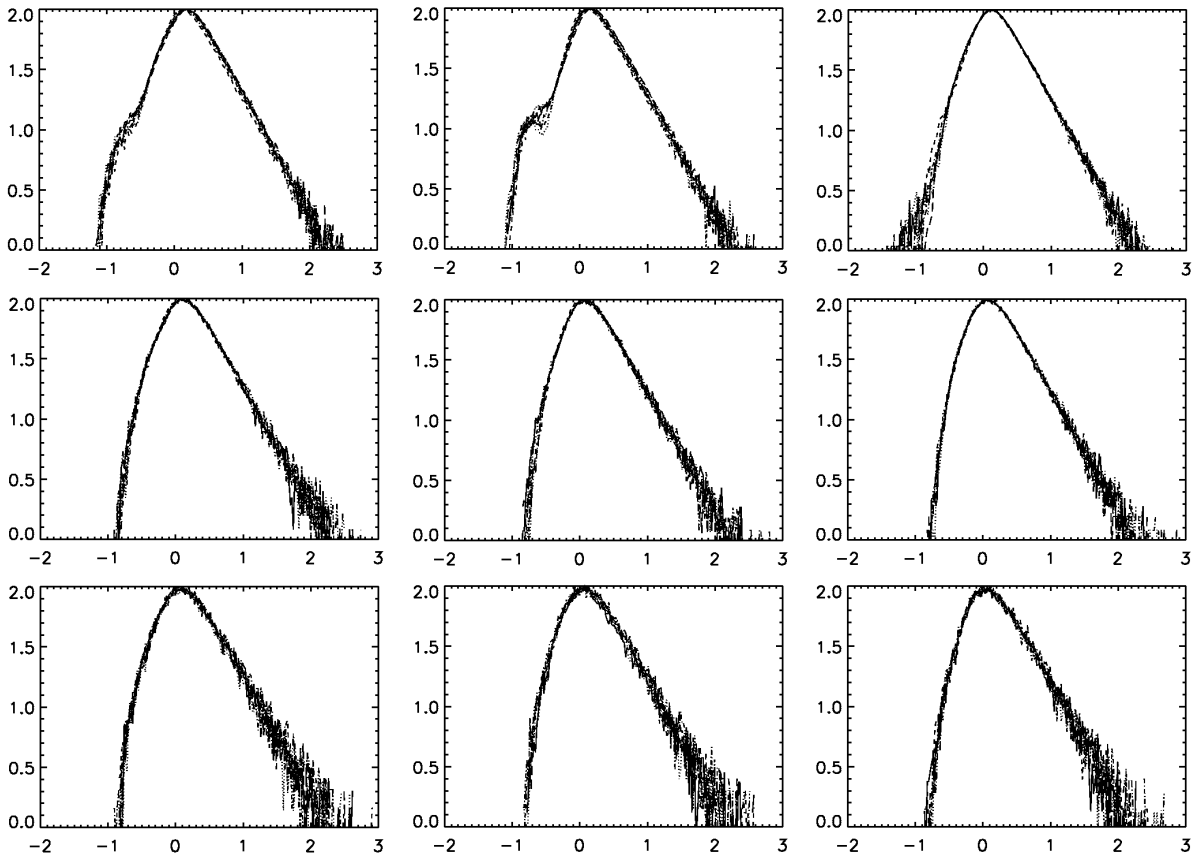

Fig. 6.2: Singularity spectra derived from the wavelet coefficients at the different scales and orientations. From left to right: Horizontal, Vertical, and Diagonal orientations. From top to bottom: $j = 1$, $j = 2$ and $j = 3$. The lines correspond to Daubechies $p = 3$ (solid), Daubechies $p = 6$ (dotted), Haar (dashed), Coiflet $p = 1$ (dash dot), Symmlet $p = 4$ (dash dot dot), and Battle-Lemarié $p = 3$ (long dashes).

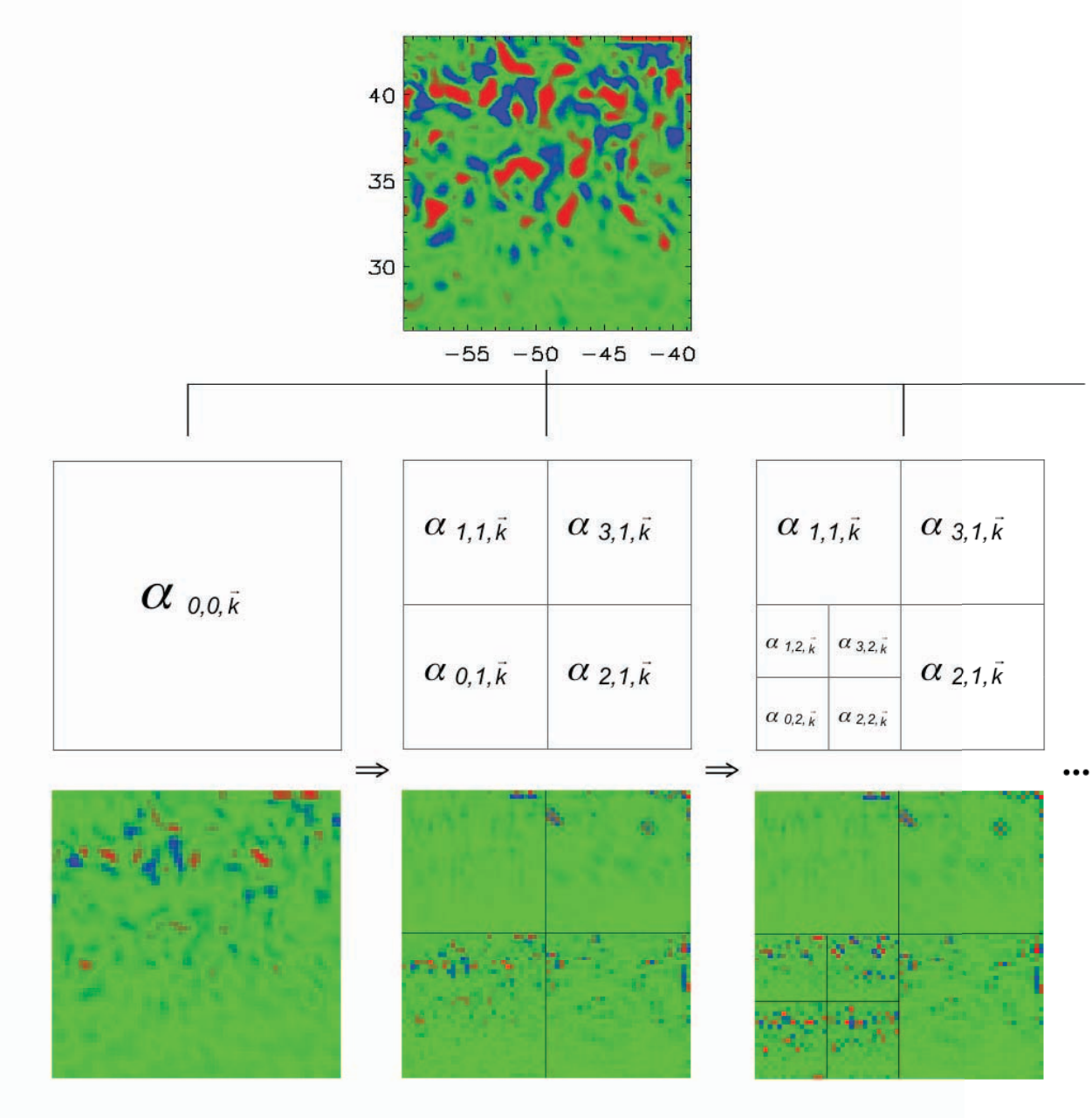

Fig. 6.3: Wavelet multi-resolution decomposition of the vorticity-derived field from SLA map (January 1st, 1997, 64 × 64 pixels) decomposed on 2 levels ($j = 1, 2$), distinguishing vertical ($r = 1$), horizontal ($r = 2$), and diagonal ($r = 3$) details. The orientation $r = 0$ corresponds to the approximation of the image at each scale j. The wavelet used in this case was order 3 Battle-Lemarié basis.

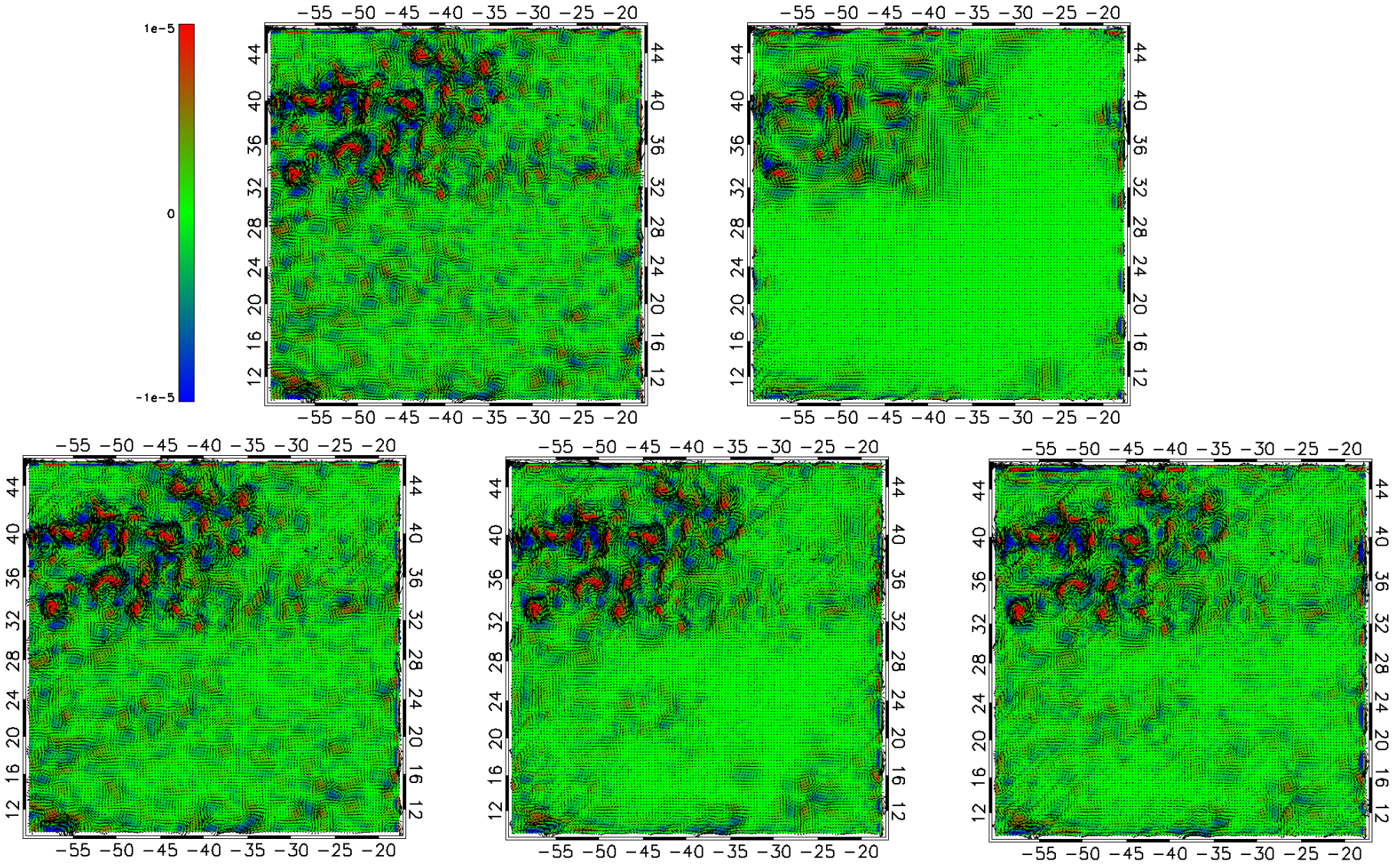

Fig. 6.4: Results of the different thresholds on a map (January 1$^{\text{st}}$, 1997). Vorticity fields given as background color. **Top:** Original field (left) and coherent field for D&J's threshold (right). **Bottom:** Coherent fields retaining 10% of wavelet modes using $p = 3$ Battle-Lemarié basis. Figures correspond to Global Threshold (left), Windowed Threshold (middle), and Multiscale Threshold (right).

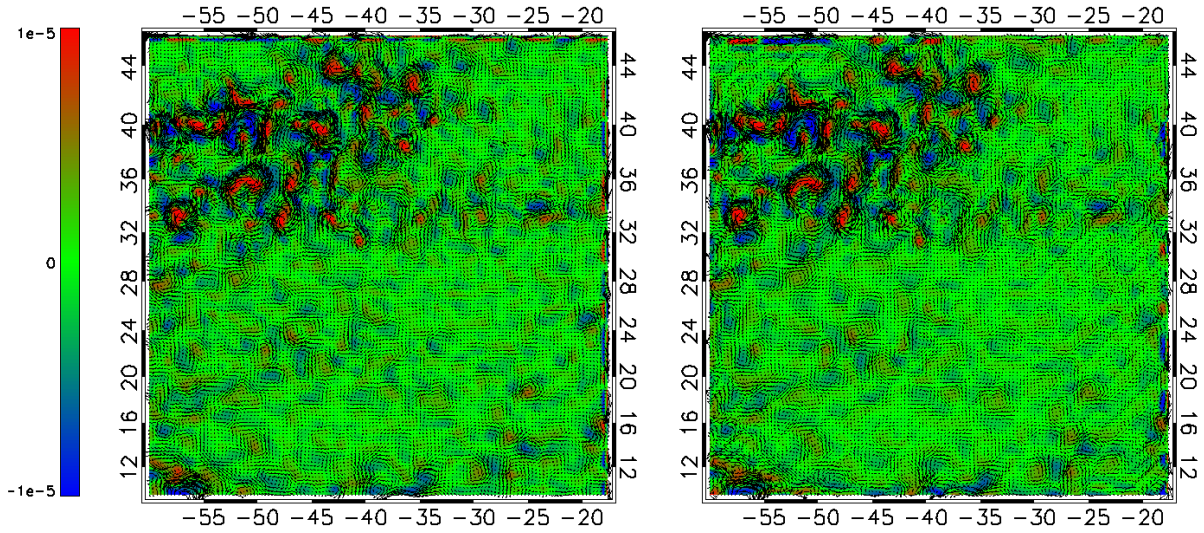

Fig. 6.5: Results of the application of singularity threshold on the January 1$^{\text{st}}$, 1997 map using $p = 3$ Battle-Lemarié basis. Vorticity fields are represented in the same way as in Figure 6.4. **Left:** Original vorticity and velocity fields. **Right:** Coherent vorticity and velocity fields for 10% of the wavelet modes.

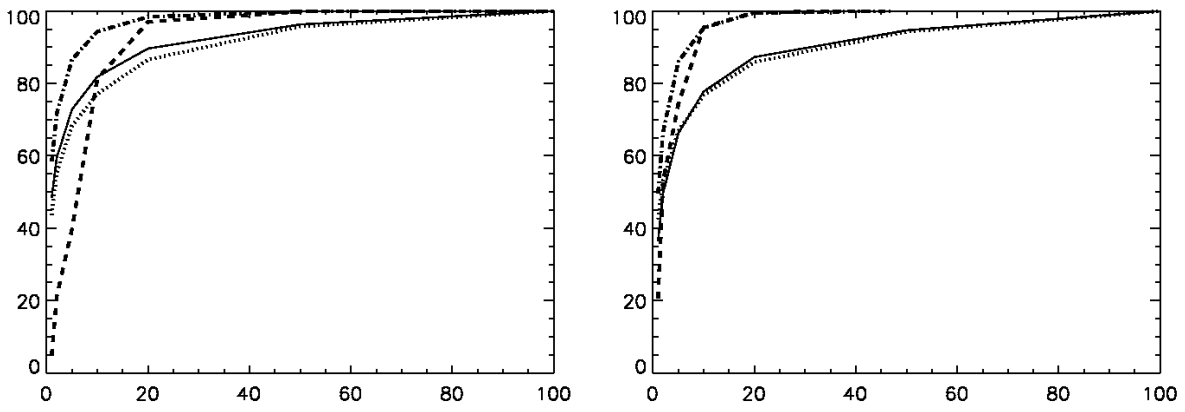

Fig. 6.6: **Left:** Coherent enstrophy percentages vs f for the January 1$^{\text{st}}$,1997 map. **Right:** The same for the coherent kinetic energy. In both cases, lines represent the Global Threshold (dash dot), Windowed Threshold (solid), Multiscale Threshold (dotted), and the Singularity Threshold (dashed).

CHAPTER 7

Discussion

In this chapter, a discussion about the results from my ongoing research on ocean dynamics through Microcanonical Multifractal Formalism is presented using the same publication order described in Section 1.1.

In "Tracking oceanic currents by singularity analysis of MicroWave Sea Surface Temperature images" [136] we investigated how to effectively use MMF and local wavelet-based Singularity Analysis to extract physically significant structures from MicroWave Sea Surface Temperature images. It has been found that SA is useful in structure recognition from satellite-derived variables. In addition, the behavior of such structures has been shown to be connected to the known global picture of ocean circulation, but offering a much richer description than the usual oceanic circulation scheme. Hence, it has been possible to extract the streamlines that delineate ocean dynamics. Among other uses, SA-based pattern extraction is useful in order to measure and track mesoscale structures. SA behaves like a sophisticated edge detector, but it provides physical information about current waves, filaments or eddies. These structures are active parts of the mechanisms that control ocean and climate variability. From the standpoint of its application, the chief advantage of using MW SST images lies in their almost global coverage. Typical limiting factors, as clouds, orbital gaps, aerosol corruption, etc. do not interfere in this case. However, there are some drawbacks due to interpolation algorithms applied to this kind of data: spatial resolution is reduced, and some singular values may be smoothed.

Two of my published works, "Obtaining and monitoring of global oceanic circulation patterns by multifractal analysis of MicroWave Sea Surface Temperature images" [137] and "Técnicas multifractales para la extracción de la función de corriente a partir de imagines de la superficie del mar" [131], sketch the possibility of obtaining a dynamical stream-function applying SA to satellite images. Typically, the most direct estimation

of velocity fields from satellite variables is achieved by using altimetry products [70, 107, 52, 53, 106] and the geostrophic approximation. Thus, we were previously able to detect only structures limited to 30 km and to a time resolution of 10 days. However, a better spatio-temporal resolution is guaranteed employing SA. Some techniques based on tracking SST patterns from sequences of images, e.g., Maximum Cross Correlation (MCC), succeeded deriving surface velocity fields [31, 38, 30, 141, 16]. Yet, MCC suffers two limitations in contrast with SA: the spatial resolution is still coarse, and it does not offer estimates of surface currents from an instantaneous image or at different scales. Alternatively, Surface Quasi Geostrophy theory can be applied on the bases of MW SST images [48, 114, 115, 51]. However, their validity is restricted to specific regions and strong SST gradients conditions. Considering that the analyzed data shows a chaotic structure defined by Fully Developed Turbulence, high Reynolds numbers, turbulence-based theories seem to be also very appropriate to explain flow organization. In this context, finite-size and finite-time Lyapunov exponents can be employed to characterize ocean dynamics, but for this purpose velocity field must be known [39, 139]. Differently, singularity exponents can be obtained from any quantity dragged by the flow. Despite the above-mentioned advantages of using SA, the obtained fields should be locally re-analyzed, as the supplied velocities are dimensionless. From a single image, SA does not provide a valid estimation on the velocity modulus or the flow sense, but the flow direction at each point is known precisely.

The key goal in "Common turbulent signature in sea surface temperature and chlorophyll maps" [98] was to show that scalars dominated by advection should inherit the multifractal properties of the flow. Once the singularity maps obtained by applying SA to SST images were validated with altimetry data in the first work, in this study the same method was applied to different satellite products in order to measure the degree of correspondence of their multifractal structures [129]. SST has been previously used as a tracer of sea surface patterns [139]. Other studies also analyzed the passive behavior of chlorophyll pigments in very dynamic areas [24, 26]. Thus, we undertook a comparison between SST and Chlorophyll Concentration patterns. In this study we show that there is a tight fitting between the two, in spite of all limitations associated to these images and the intrinsic uncertainty of the SA. This result reinforces the assumption that there is common dynamical mechanism acting on the different scalars. Additionally, we analyzed if there was the same statistical turbulent signature in both of the images through the singularity spectrum. Once more, we found evidence that there is a connection between the multifractal properties of such variables and the turbulent advection of the flow. The latter is the underlying cause of flow complexity. A major finding of my research is that the close matching between image processing and physics is independent of the particularities of any scalar tracer and at any scale or specific region of study. These conclusions open the way to complement CC maps with SST ones, which offer a wider coverage, at those points where CC information is missing. This analysis offers the appealing perspective to understand, e.g., the biology of phytoplankton communities.

After demonstrating the geometrical organization of some satellite scalars as SST and CC, it was natural to apply the same kind of analysis to Sea Level Anomalies (SLA) to investigate the possibility of using their multifractal properties for an improved description of mesoscale ocean circulation. In "Analysis of ocean turbulence using adaptive CVE on altimetry maps" [99], Coherent Vortex Extraction technique was applied to SLA maps and improved by means of a multifractal scheme [19, 132, 133] to get dynamical information about the ocean in a more realistic way. An essential result is that this adaptive version of CVE was physically more meaningful, and anyway able to separate coherent and incoherent parts of the flow in such a way that lower scales were better resolved and the coherent contribution was defined by using a reduced number of degrees of freedom. In this way, the compression is noteworthy and the computational cost is significantly reduced. By using the standard global threshold of separation [27] and 10% only of the retained modes for the coherent part, around 60% of the total enstrophy and 50% of the total energy can be effectively represented. This threshold does not consider the local structures of the flow at each point. In fact, there is still a relevant part of the eddy field that is contained in the incoherent part after decomposition. This limitation was overcome by introducing geometrical properties of the flow after proving the existence of a multifractal hierarchy in SLA maps. This novel procedure using 10% only of the coherent modes allows recovering 81% of the total enstrophy and 95% of the total energy. Moreover, we show that smaller scales are better represented with this method.

The research presented shows that a 2D turbulent flow, as it is the case of the ocean, can be described by satellite-derived scalars characterized by multifractal properties and/or by those structures that are self-organized in coherent vortices after complex flow evolution. These structures are subjected to the velocity field - due to long-range interactions, each vortex feels the influence of the mean field due to many others - and they play an important role in ocean dynamics.

CHAPTER 8

Conclusions

Microcanonical Multifractal Formalism offers a new perspective of turbulent flow events far from the mechanicistic view that has been dominating our models to capture flow organization. In a world in which phenomena cannot be completely understood in terms of causal relations, different theories are required. From this need, MMF in conjunction with wavelet analysis has emerged to achieve the goal of predicting scenarios and behavior of real flows using more reliable approximations. To successfully deal with the application of multi-resolution analysis to satellite products, techniques such as Singularity Analysis and Coherent Vortex Extraction have been used.

Instead of starting from the evolution equations of microscopic entities, i.e., water packages in the Navier-Stokes equations, these novel techniques start from macroscopic entities (mesoscale eddies, fronts, jets, zonal gyres, etc.) that, by means of validated and more realistic equations, are easier to be observed and described. The flow can be partitioned into a part that is coherent and a remainder that is incoherent. This up-down approach is particularly convenient for short-term mesoscale prediction (operational models) and experimental data assimilation purposes. On the contrary, down-up simulations are affected by the noise at small scales, so that numerical dissipation needs to be introduced. In this way, mesoscale structures of low amplitude are somehow removed; but these structures should be considered to avoid distorting the real picture of ocean circulation, as these structures are the best ones defining oceanic behavior because of their energy and mass transport capacity. Furthermore, by using the methods proposed in this document the evolution of the system can be followed with lower number of degrees of freedom, which implies a reduced computational cost with respect to numerical models. There is, however, a lot to be gained by exhaustively comparing results from MMF on satellite data with results obtained in the traditional and classical mechanics framework. Since these new methods are scale-invariant, their results can be adapted to

a given resolution scale, and results obtained from data at other resolutions are directly comparable. Progress has been steadily advancing concerning different theoretical and numerical approaches. However, there are still fundamental questions that cannot be answered, and turbulence is far from being fully understood. Thus, combination of both models will help to reach an even better dynamical description of non-linear systems and also of their causal relations. Further studies on this issue will be fundamental.

These new techniques not only apparently succeeded in obtaining a new picture of today's ocean system and a better understanding of the processes taking place in the ocean; but these techniques also have allowed to tackle turbulence problems realistically, in spite of all problems associated with satellite imagery. In particular, it has been possible to infer a large amount of instantaneous information on the spatial multiscale view of ocean flows, e.g., satellite-derived detailed velocity maps for the ocean surface at any location and time, which are not a valid estimation of the velocity field but instead identify correctly the flow direction at each point. What is more, it has been shown that, according to the principles of turbulent cascading, the distribution of singularity exponents derived at a given scale is in equilibrium with the distribution of exponents as observed at any other scales. This implies that kinetic energy and/or enstrophy is distributed in such a way that it guarantees a continuous transfer between larger and smaller scales. The multiplicative cascade of the scalar is analogous to the energy cascade of the flow owing to the Fully Developed Turbulence regime. Studying the statistics of the corresponding singularity spectra, one can compare the cascading processes associated to each type of scalar. It has been proved that the singularity spectra of different satellite-derived scalar tracers coincide at any scale or specific region under study. The cascade is also preserved when discrete-wavelet representations are used, as they are scale-invariant by construction. On the bases of a well-adapted wavelet-based method, CVE has been also improved over real data to extract coherent structures for all available scales - going from the children coefficients to the parent coefficient in the pyramidal wavelet decomposition.

These contributions open the way to many operational and reanalysis applications as well as to future merging and interpolation techniques. The recovery of flow structures where information is lacking should be possible by examining adequate scalars and calculating their singularity exponents. In this way, as the local information is available for almost all the scales from an instantaneous image, spatial and temporal resolutions of those maps of poor quality could be improved. Despite the fact that the proposed methods have been applied to satellite images, they are flexible as well as valid for other type of data, and for a 3D scope. Moreover, the application range of these techniques is not restricted to the ocean; they comprise many dynamical systems with non-linear coupling. This obviously includes turbulent and chaotic flows in general, and more globally dynamical systems with non-linear and scale-invariant character. In any of the presented

studies, scale invariance symmetry of satellite scalars has been the key point and this evidences the dominant role of turbulence in oceanic flows.

List of Figures

List of Tables

Bibliography

[1] E.A. Abraham and M.M. Bowen. Chaotic stirring by a mesoscale surface-ocean flow. *Chaos*, 12(2):373–381, 2002. doi:10.1063/1.1481615.

[2] F. Anselmet, Y. Gagne, E.J. Hopfinger, and R.A. Antonia. High order velocity structure functions in turbulent shear flows. *Journal of Fluid Mechanics*, 140:63–89, 1984.

[3] J.R. Apel. *Principles of Ocean Physics*, volume 38. International Geophysics Series, 1987.

[4] A. Arneodo. Wavelet analysis of fractals: from the mathematical concepts to experimental reality. In G. Erlebacher, M. Yousuff Hussaini, and L.M. Jameson, editors, *Wavelets. Theory and applications*, page 349. Oxford University Press. ICASE/LaRC Series in Computational Science and Engineering, Oxford, 1996.

[5] A. Arneodo, F. Argoul, E. Bacry, J. Elezgaray, and J. F. Muzy. *Ondelettes, multifractales et turbulence*. Diderot Editeur, Paris, France, 1995.

[6] A. Arneodo, C. Baudet, F. Belin, R. Benzi, B. Castaing, B. Chabaud, R. Chavarria, S. Ciliberto, R. Camussi, F. Chilla, B. Dubrulle, Y. Gagne, B. Hébral, J. Herweijer, M. Marchand, J. Maurer, J. F. Muzy, A. Naert, A. Noullez, J. Peinke, F. Roux, P. Tabeling, W. vandeWater, and H. Willaime. Structure functions in turbulence, in various flow configurations, at reynolds number between 30 and 5000, using extended self-similarity. *Europhysics Letters*, 34(6):411–416, 1996.

[7] A. Arneodo, J.-F. Muzy, and D. Sornette. "direct" causal cascade in the stock market. *European Physical Journal B*, 2:277–282, 1998.

[8] J. Arrault, A. Arneodo, A. Davis, and A. Marshak. Wavelet-based multifractal analysis of rough surfaces: application to cloud models and satellite data. *Phys. Rev. Lett.*, 79:75–79, 1997.

[9] AVISO User Handbook. *Corrected Sea Surface heights products*. Collecte Localisation Satellite, France, 2.0 edition, November 1996. AVI-NT-011-311-CN.

[10] N. Ayoub, P.Y. LeTraon, and P. De Mey. A description of the Mediterranean surface variable circulation from combined ERS-1 and TOPEX/POSEIDON altimetric data. *Journal of Marine Systems*, 18:3–40, 1998.

[11] G.K. Batchelor. Diffusion in a field of homogeneous turbulence.II. The relative motion of particles. *Proc. Camb. Phil. Soc.*, 48:345–362, 1952.

[12] D. Béréziat, I. I. Herlin, and L. Younes. A generalized optical flow constraint and its physical interpretation. In *Proceedings of Computer Vision and Pattern Recognition, CVPR'00*. IEEE, June 2000.

[13] C. Beta, K. Schneider, and M. Farge. Wavelet filtering to study mixing in 2d isotropic turbulence. *Comm. in Nonlin. Sci. and Num. Sim.*, 8:537–545, 2003.

[14] O. Boebel and Ch. Barron. A comparison of in-situ float velocities with altimeter derived geostrophic velocities. *Deep-Sea Research II*, 50:119–139, 2003.

[15] O. Boebel, T. Rossby, J. Luterharms, E. Zenk, and Ch. Barron. Path and variability of the alghulas return current. *Deep Sea Research II*, 50:35–56, 2003.

[16] M. Bowen, W.J. Emery, J.L. Wilkin, P.C. Tildesley, I. Barton, and R. Knewtson. Extracting multiyear surface currents from sequential thermal imagery using the maximum cross-correlation technique. *Journal of Atmospheric and Oceanic Technology*, 19(10):1665–1676, 2002.

[17] A. Bracco, J. LaCasce, and A. Provenzale. Velocity probability density functions for oceanic floats. *J. Phys. Ocean.*, 20:461–474, 2000.

[18] A. Bracco, J. von Hardenberg, A. Provenzale, J.B. Weiss, and J.C. McWilliams. Dispersion and mixing in quasigeostrophic turbulence. *Phys. Rev. Lett.*, 92(8):doi: 10.1103/PhysRevLett.92.084501, February 2004.

[19] R. W. Buccigrossi and E. P. Simoncelli. Image compression via joint statistical characterization in the wavelet domain. *IEEE Transactions in Image Processing*, 8:1688–1701, 1999.

[20] B. Castaing. The temperature of turbulent flows. *Journal de Physique II*, 6:105–114, 1996.

[21] Dudley B. Chelton. Report of the high-resolution ocean topography. Technical report, Science Working Group Meeting Report, 2001.

[22] S. Côté and A.R.L. Tatnall. The hopfield neural network as a tool for feature tracking and recognition from satellite sensor images. *International Journal of Remote Sensing*, 18(4):871–885, 1997.

[23] I. Daubechies. *Ten lectures on wavelets*. CBMS-NSF Series in App. Math. Capital City Press, Montpelier, Vermont, 1992.

[24] K. L. Denman and M. A. Abbott. Time scales of pattern evolution from cross-spectrum analysis of advanced very high resolution radiometer and coastal zone color scanner imagery. *J. Geophys. Res.*, 99(C4):7433–7442, 1994.

[25] C. M. Domingues, G. A. Goncalves, R. D. Ghisolfi, and C.A.E. Garcia. Advective surface velocities derived from sequential infrared images in the southwestern atlantic ocean. *Remote Sensing of the Environment*, 73(2):218–226, 2000.

[26] S. Doney, D. M. Glover, S. J. McCue, and M. Fuentes. Mesoscale variability of seawifs satellite ocean color: Global patterns and spatial scales. *J. Geophys. Res.*, 108:6.1–6.15, 2003.

[27] D. Donoho and I. Johnstone. Ideal spatial adaptation by wavelet shrinkage. *Biometrika*, 81(3):425–455, 1994.

[28] B. Dubrulle. Intermittency in fully developed turbulence: Log-poisson statistics and generalized scale covariance. *Physical Review Letters*, 73:959–962, 1994.

[29] N. Ducet, P.Y. LeTraon, and G. Reverdin. Global high-resolution mapping of ocean circulation from TOPEX/Poseidon and ERS-1 and -2. *J. Geophys. Res.*, 105:19477–19498, 2000.

[30] W.J. Emery, C. Fowler, and C. A. Clayson. Satellite-image-derived gulf stream currents compared with numerical model results. *Journal of Atmospheric and Oceanic Technology*, 9:286–304, 1992.

[31] W.J. Emery, A.C. Thomas, M.J. Collins, W.R. Crawford, and D.L. Mackas. An objective method for computing advective surface velocities from sequential infrared satellite images. *Journal of Geophysical Research*, 91:12865–12878, 1986.

[32] K. Falconer. *Fractal Geometry: Mathematical Foundations and Applications*. John Wiley and sons, Chichester, 1990.

[33] M. Farge, N. Kevlahan, V. Perrier, and K. Schneider. Turbulence analysis, modelling and computing using wavelets. In J. van den Berg, editor, *Wavelets and Physics*, pages 117–200. Cambridge University Press, 1999.

[34] M. Farge and K. Schneider. Coherent vortex simulation (cvs): a semi-deterministic turbulence model. *Flow Turbul. Combust.*, 66:393–426, 2001.

[35] M. Farge, K. Schneider, and N. Kevlahan. Non-gaussianity and coherent vortex simulation for two-dimensional turbulence using an adaptative orthogonal wavelet basis. *Physics of Fluids*, 11(8):2187–2201, 1999.

[36] P. Flament and L. Armi. The Shear, Convergence, and Thermohaline Structure of a Front. *Journal of Physical Oceanography*, 30:51–66, 2000.

[37] U. Frisch. *Turbulence*. Cambridge Univ. Press, Cambridge MA, 1995.

[38] C.A.E. García and I.S. Robinson. Sea surface velocities in shallow seas extracted from sequential coastal Zone Color Scanner satellite data. *Journal of Geophysical Research*, 94(C9):12681–12691, 1989.

[39] A. Garcia-Olivares, J. Isern-Fontanet, and E. Garcia-Ladona. Dispersion of passive tracers and finite-scale Lyapunov exponents in the Western Mediterranean Sea. *Deep Sea Research I*, 54:253–268, 2007.

[40] S.T. Gille and S. Llewellyn Smith. Velocity probability density functions from altimetry. *Journal of Physical Oceanography*, pages 125–136, 2000.

[41] S.T. Gille, M.M. Yale, and D.T. Sandwell. Global correlation of mesoscale ocean variability with seafloor roughness from satellite altimetry. *Geophys. Res. Lett.*, 27:1251–1254, 2000.

[42] J.F.R. Gower, K.L. Denman, and R.J. Holyer. Phytoplankton patchiness indicates the fluctuation spectrum of mesoscale oceanic structure. *Nature*, 288:157–159, 1980.

[43] J. Grazzini, A. Turiel, and H. Yahia. Analysis and comparison of functional dependencies of multiscale textural features on monospectral infrared images. In *Proc. of IGARSS*, volume 3, pages 2045–2047, 2003.

[44] V.K. Gupta and E.C. Waymire. Multiscaling properties of spatial rainfall and river flow distributions. *Journal of Geophysical Research*, 95(D3):1999–2009, 1990.

[45] J. Gyory, A.J. Mariano, and E.H. Ryan. The benguela current. Ocean surface currents. Technical report, 2005.

[46] R. Hallberg and A. Gnanadesikan. The role of eddies in determining the structure and response of the wind-driven southern hemisphere overturning: Results from the modeling eddies in the southern ocean (MESO) project. *J. Phys. Oceanogr.*, 36:2232–2252, 2006.

[47] G. Haller. An objective definition of a vortex. *Journal of Fluid Mechanics*, 525:1–26, 2005.

[48] I. Held, R.T. Pierrehumbert, S.T. Garner, and K.L. Swanson. Surface quasi-geostrophic dynamics. *J. Fluid Mech.*, 282:1–20, 1995.

[49] I. Herlin, I. Cohen, and S. Bouzidi. Image processing for sequences of oceanographic images. *The journal of Visualization and Computer Animation*, 7:169–176, 1996.

[50] P. Holmes, J.L. Lumley, and G. Berkooz. *Turbulence, Coherent Structures, Dynamical systems and Symmetry.* Cambridge University Press, Cambridge MA, 1996.

[51] J. Isern-Fontanet, B. Chapron, G. Lapeyre, and P. Klein. Potential use of microwave sea surface temperatures for the estimation of ocean currents. *Geophysical Research Letters*, 22:L24608, 2006.

[52] J. Isern-Fontanet, E. García-Ladona, and J. Font. Identification of marine eddies from altimetry. *J. Atmos. Oceanic Technol.*, 20:772–778, 2003.

[53] J. Isern-Fontanet, E. García-Ladona, and J. Font. The vortices of the Mediterranean sea: an altimetric perspective. *Journal of Physical Oceanography*, 36:87–103, 2006.

[54] J. Isern-Fontanet, E. García-Ladona, J. Font, and A. García-Olivares. Non-gaussian velocity Probability Density Functions: an altimetric perspective of the Mediterranean sea. *J. Phys. Oceanogr.*, 36:2153–2164, 2006.

[55] J. Isern-Fontanet, A. Turiel, E. Garcia-Ladona, and J. Font. Microcanonical multifractal formalism: application to the estimation of ocean surface velocities. *Journal of Geophysical Research*, 112:C05024, 2007.

[56] J. Jeong and F. Hussain. On the identification of a vortex. *J. Fluid Mech.*, 285:69–94, 1995.

[57] J. Jiménez. Algebraic probability density tails in decaying isotropic two dimensional turbulence. *J. Fluid Mech.*, 313:223–240, 1996.

[58] K. A. Kelly and P.T. Strub. Comparison of velocity estimates from advanced very high resolution radiometer in the coastal transition zone. *Journal of Geophysical Research*, 97:9653–9668, 1992.

[59] P. Kestener and A. Arnéodo. Three-dimensional wavelet-based multifractal method: The need for revisiting the multifractal description of turbulence dissipation data. *Phys. Rev. Lett*, 91(19):194501, November 2003.

[60] K.A. Kilpatrick, G.A. Podestá, and R. Evans. Overview of the NOAA/NASA advanced very high resolution radiometer Pathfinder algorithm for the sea surface temperature and associated matchup database. *J. Geophys. Res.*, 106:9179–9197, 2001.

[61] A. N. Kolmogorov. Dissipation of energy in a locally isotropic turbulence. *Dokl. Akad. Nauk. SSSR*, 32:16–18, 1941.

[62] A. N. Kolmogorov. The local structure of turbulence in an incompressible fluid with very large reynolds number. *Dokl. Akad. Nauk. SSSR*, 309:301–305, 1941.

[63] A. N. Kolmogorov. A refinement of previous hypotheses concerning the local structure of turbulence in a viscous incompressible fluid at high reynolds number. *J. Fluid Mech.*, 13:82–85, 1962.

[64] R.H. Kraichnan. Intermittency in the very small scales of turbulence. *Physics of Fluids*, 10:2080–2082, 1967.

[65] R.H. Kraichnan. Small-scale structure of a scalar field convected by turbulence. *Physics of Fluids*, 11(5):945–963, May 1968.

[66] R.H. Kraichnan. Anomalous scaling of a randomly advected passive scalar. *Physical Review Letters*, 72(7):1016–1020, February 1994.

[67] J. LaCasce and A. Mahadevan. Estimating subsurface horizontal and vertical velocities from sea-surface temperature. *Journal of Marine Research*, 64:695–721, 2006.

[68] G. Lapeyre, B.L. Hua, and P. Klein. Dynamics of the orientation of active and passive scalars in two dimensional turbulence. *Physics of Fluids*, 13(1):251–264, January 2001.

[69] G. Larnicol, N. Ayoub, and P.Y. LeTraon. Major changes in Mediterranean Sea level variability from 7 years of TOPEX/Poseidon and ERS-1/2 data. *Journal of Marine Systems*, 33:63–89, 2002.

[70] G. Larnicol, P.Y. LeTraon, N. Ayoub, and P. De Mey. Mean sea level and surface circulation variability of the Mediterranean Sea from 2 years of TOPEX/POSEIDON altimetry. *Journal of Geophysical Research*, 100(C12):25163–25177, 1995.

[71] C. Lentini, D. Olson, and G. Podestá. Statistics of brazil of current rings observed from avhrr: 1993 to 1998. *Geophys. Res. Lett.*, 29(1811):10.1029/2002GL015221, 2002.

[72] P.Y. LeTraon, F. Nadal, and N. Ducet. An improved mapping method of multi-satellite altimeter data. *J. Atmos. Oceanic Technol.*, 15(2):522–534, 1998.

[73] P.Y. LeTraon and F. Ogor. ERS-1/2 orbit improvement using TOPEX/POSEIDON: the 2cm challenge. *Journal of Geophysical Research*, 103(C4):8045–8057, 1998.

[74] X. Lou, W. Huang, A. Shi, and B. Fu. An improved front-following algorithm for oceanic front measurement with AVHRR SST imagery. In *Proceedings of the IEEE International conference on Transactions on Geoscience and Remote Science. IGARSS '05*, volume 4, pages 2629–2631, 2005.

[75] S. Lovejoy, W.J.S. Curri, Y. Tessier, M.R. Claereboudt, E. Bourget, J.C. Roff, and D. Schertzer. Universal multifractals and ocean patchiness: phytoplankton, physical fields and coastal heterogeneity. *J. Plankt. Res.*, 23(2):117–141, 2001.

[76] S. Lovejoy, D. Schertzer, Y. Tessier, and H. Gaonac'h. Multifractals and resolution-independent remote sensing algorithms: the example of ocean colour. *International Journal of Remote Sensing*, 22(7):1191–1234, 2001.

[77] J.R.E. Lutjeharms and R. C. Van Ballegooyen. The retroflection of the alghulas current. *J. Phys. Oceanogr.*, 18:1570–1583, 1988.

[78] J.R.E. Lutjeharms and H.R. Valentine. Eddies at the subtropical convergence south of africa. *J. Phys. Oceanogr.*, 18:761–774, 1988.

[79] A. Mahadevan and J.W. Campbell. Biogeochemical patchiness at the sea surface. *Geophysical Research Letters*, 29:1926, 2002.

[80] S. Mallat and W. L. Huang. Singularity detection and processing with wavelets. *IEEE Trans. in Inf. Th.*, 38:617–643, 1992.

[81] S. Mallat and S. Zhong. Wavelet transform maxima and multiscale edges. In Mary Beth Ruskai et al, editor, *Wavelets and their applications*. Jones and Bartlett, Boston, 1991.

[82] S. Mallat and S. Zhong. Characterization of signals from multiscale edges. *IEEE Trans. on Pattern Analysis and Machine Intelligence*, 14:710–732, 1992.

[83] Stéphane Mallat. *A Wavelet Tour of Signal Processing*. Academic Press, 2nd Edition, 1999.

[84] B. Mandelbrot. Intermittent turbulence in self-similar cascades: divergence of high moments and dimension of the carrier. *J. Fluid Mech.*, 62:331–358, 1974.

[85] B. Mandelbrot. *Fractals: Form, Chance and Dimension*. Freeman & Co, 1977.

[86] A.P. Martin. Phytoplankton patchiness: the role of lateral stirring and mixing. *Progress in Oceanography*, 57:125–174, 2003.

[87] A.P. Martin, K.J. Richards, A. Bracco, and A. Provenzale. Patchy productivity in the open ocean. *Global Biogeochemical Cycles*, 16:449, 2001.

[88] A.M. Martins and J.L. Pelegrí. CZCS chlorophyll patterns in the South Atlantic Bight during low vertical stratification conditions. *Continental Self Research*, 26:429–457, 2006.

[89] C. R. McClain, M.L. Cleave, G.C. Feldman, W.W. Gregg, S.B. Hooker, and N. Kuring. Science quality seawifs data for global biosphere research. *Sea Technology*, 39:10–14, 1998.

[90] J. McWilliams. The vortices of two-dimensional turbulence. *Journal of Fluid Mechanics*, 219:361, 1990.

[91] J.C. McWilliams. The emergence of isolated coherent vortices in turbulent flow. *J. Fluid Mech.*, 146:21–43, 1984.

[92] C. Meneveau and K.R. Sreenivasan. Simple multifractal cascade model for fully developed turbulence. *Physical Review Letters*, 59:1424–1427, 1987. 10.1103/PhysRevLett.59.1424.

[93] B. K. Mignone, J. L. Sarmiento, R. D. Slater, and A. Gnanadesikan. Sensitivity of sequestration efficiency to mixing processes in the global. *Energy*, 29:1467–1478, 2004.

[94] R. Morrow, F. Birol, D. Griffin, and J. Sudre. Divergent pathways of cyclonic and anti-cyclonic ocean eddies. *Geophysical Research Letters*, 31:doi:10.1029/2004GL020974, 2004.

[95] W. Munk. Oceanography before, and after, the advent of satellites. In D. Halpern, editor, *Satellites, Oceanography and Society*, pages 1–4. Elsevier Oceanography Series, Elsevier, 2000.

[96] J. F. Muzy, E. Bacry, and A. Arneodo. Wavelets and multifractal formalism for singular signals: Application to turbulence data. *Physical Review Letters*, 67:3515–3518, 1991.

[97] J.-F. Muzy, D. Sornette, J. Delour, and A. Arneodo. Multifractal returns and hierarchical portfolio theory. *Quantitative Finance*, 1:131–148, 2001.

[98] V. Nieves, C. Llebot, A. Turiel, J. Solé, E. García-Ladona, M. Estrada, and D. Blasco. Common turbulent signature in sea surface temperature and chlorophyll maps. *Geophysical Research Letters*, 34:L23602, 2007.

[99] V. Nieves and A. Turiel. Analysis of ocean turbulence using adaptive cve on altimetry maps. accepted in *Journal of Marine Systems*.

[100] E. A. Novikov. Infinitely divisible distributions in turbulence. *Physical Reviev E*, 50:R3303, 1994.

[101] A.M. Obukhov. Spectral energy distribution in a turbulent flow. *Izv. Akad. Nauk SSSR Ser. Geogr. Geofiz.*, 5:453–466, 1941.

[102] A.M. Obukhov. Some specific features of atmospheric turbulence. *J. Fluid Mech.*, 13:77–81, 1962.

[103] A. Okubo. Ocean diffusion diagramas. *Deep Sea Research*, 18:789–802, 1971.

[104] A. H. Orsi, T. Whitworth, and W.D. Nowling. On the meridional extent and fronts of the antarctic circumpolar current. *Deep Sea Research, Series I*, 42:641–673, 1995.

[105] G. Parisi and U. Frisch. On the singularity structure of fully developed turbulence. In M. Ghil, R. Benzi, and G. Parisi, editors, *Turbulence and Predictability in Geophysical Fluid Dynamics. Proc. Intl. School of Physics E. Fermi*, pages 84–87, Amsterdam, 1985. North Holland.

[106] A. Pascual, Y. Faugere, G. Larnicol, and P.Y. LeTraon. Improved description of the ocean mesoscale variability by combining four satellite altimeters. *Geophys. Res. Lett*, 33(2):611, 2006. doi:10.1029/2005GL024633.

[107] A. Pascual, B.B. Nardelli, G. Larnicol, M. Emelianov, and D. Gomis. A case of an intense anticyclonic eddy in the Balearic Sea (western Mediterranean). *Journal of Geophysical Research*, 107:3183, 2002.

[108] J. Pedlosky. *Geophysical fluid dynamics*. Springer-Verlag, 1987.

[109] O. Pont, A. Turiel, and C. Pérez-Vicente. Application of the microcanonical multifractal formalism to monofractal systems. *Physical Review E*, 74:061110, 2006.

[110] R.W. Reynolds and T.M. Smith. Improved global sea surface temperature analyses using optimal interpolation. *Journal of Climate*, 7:929–948, 1994.

[111] P. Rhines. Geostrophic turbulence. *Annual Review of Fluid Mechanics*, 11:401–441, 1979.

[112] J. E. Ruppert-Felsot, O. Praud, E. Sharon, and H. L. Swinney. Extraction of coherent structures ina a rotating turbulent flow experiment. *Physical Review E*, 72:016311, 2005.

[113] K. Schneider, M. Farge, G. Pellegrino, and M.M. Rogers. Coherent vortex simulation of three-dimensional turbulent mixing layers using orthogonal wavelets. *Journal of Fluid Mechanics*, 534:39–66, 2005.

[114] K. Shafer-Smith and G.K. Vallis. The scales and equilibration of midocean eddies: Freely evolving flow. *Journal of Physical Oceanography*, 31:554–571, 2001.

[115] K. Shafer-Smith and G.K. Vallis. The scales and equilibration of midocean eddies: Forced-dissipative flow. *Journal of Physical Oceanography*, 32:1699–1720, 2002.

[116] A. G. P. Shaw and R. Vennell. A front-following algorithm for avhrrsst imagery. *Remote Sensing of Environment*, 72:317–327, 2000.

[117] A. G. P. Shaw and R. Vennell. Measurements of an oceanic front using a front-following algorithm for avhrr sst imagery. *Remote Sensing of Environment*, 75:47–62, 2001.

[118] Z. S. She and E. Leveque. Universal scaling laws in fully developed turbulence. *Physical Review Letters*, 72:336–339, 1994.

[119] Z. S. She and E. C. Waymire. Quantized energy cascade and log-poisson statistics in fully developed turbulence. *Physical Review Letters*, 74:262–265, 1995.

[120] R. Simó and C. Pedrós-Alió. Role of vertical mixing in controlling the oceanic production of dimethyl sulphide. *Nature*, 402:396–399, 1999.

[121] D. Stammer. Global characteristics of ocean variability estimated from regional topex/poseidon altimeter measurements. *J. Phys. Oceanogr.*, 27:1743–1769, August 1997.

[122] W. Takahashia and H. Kawamurab. Detection method of the kuroshio front using the satellite-derived chlorophyll-a images. *Remote Sensing of Environment*, 97:83–91, 2005.

[123] H. Tennekes and J.L. Lumley. *A First Course in Turbulence*. The Massachusetts Institute of Technology, 1973.

[124] R. Tokmakian, P.T. Strub, and J. McClean-Padman. Evaluation of the maximum cross-correlation method of estimating sea surface velocities from sequential satellite images. *Journal of Atmospheric and Oceanic Technology*, 7(6):852–865, 1990.

[125] A. Turiel. Relevance of multifractal textures in static images. *Electronic Letters on Computer Vision and Image Analysis*, 1(1):35–49, 2003.

[126] A. Turiel and A. del Pozo. Reconstructing images from their most singular fractal manifold. *IEEE Trans. on Im. Proc.*, 11:345–350, 2002.

[127] A. Turiel, J. Grazzini, and H. Yahia. Multiscale techniques for the detection of precipitation using thermal IR satellite images. *IEEE Geoscience and Remote Sensing Letters*, 2(4):447–450, October 2005. doi:10.1109/LGRS.2005.852712.

[128] A. Turiel, J. Isern-Fontanet, and E. García-Ladona. Wavelet filtering to extract coherent vortices from altimetric data. *Journal of Atmospheric and Oceanic Technology*, 24:2103–2119, 2007.

[129] A. Turiel, J. Isern-Fontanet, E. García-Ladona, and J. Font. Multifractal method for the instantaneous evaluation of the stream function in geophysical flows. *Physical Review Letters*, 95(10):104502, September 2005. doi:10.1103/PhysRevLett.95.104502.

[130] A. Turiel, J. Isern-Fontanet, E. Garcia-Ladona, and J. Young. Detection of wave fronts in the Indian Ocean from geostationary sunglint satellite imagery. *International Journal of Remote Sensing*, 28:3953–3962, 2007.

[131] A. Turiel, V. Nieves, and E. Garcia-Ladona. Tecnicas multifractales para la extraccion de la funcion de corriente a partir de imagenes de la superficie del mar. *Rev. Teled., Núm. Esp.: Oceanografía y Teledetección*, 25:134–138, 2006. ISSN: 1133–0953.

[132] A. Turiel and N. Parga. The multi-fractal structure of contrast changes in natural images: from sharp edges to textures. *Neural Computation*, 12:763–793, 2000.

[133] A. Turiel and N. Parga. Multifractal wavelet filter of natural images. *Physical Review Letters*, 85:3325–3328, 2000.

[134] A. Turiel and C. Pérez-Vicente. Multifractal geometry in stock market time series. *Physica A*, 322:629–649, May 2003.

[135] A. Turiel, C. Pérez-Vicente, and J. Grazzini. Numerical methods for the estimation of multifractal singularity spectra on sampled data: a comparative study. *Journal of Computational Physics*, 216(1):362–390, July 2006.

[136] A. Turiel, J. Solé, V. Nieves, J. Ballabrera-Poy, and E. García-Ladona. Tracking oceanic currents by singularity analysis of micro-wave sea surface temperature images. *Remote Sensing of Environment*, 112:2246–2260, 2008.

[137] A. Turiel, J. Solé, V. Nieves, and E. García-Ladona. Obtaining and monitoring of global oceanic circulation patterns by multifractal analysis of microwave sea surface temperature images. *IGARSS, IEEE International*, pages 1895–1898, 2007.

[138] A. Turiel, H. Yahia, and C. Pérez-Vicente. Microcanonical multifractal formalism: a geometrical approach to multifractal systems. Part I: Singularity analysis. *Journal of Physics A*, 41:015501, 2008.

[139] D. Waugh, E.R. Abraham, and M.M. Bowen. Spatial variations of stirring in the surface ocean: A case study of the Tasman sea. *J. Phys. Oceanogr.*, 36:536–542, 2006.

[140] J. Weiss and J. McWilliam. Temporal scaling behaviour of decaying two-dimensional turbulence. *Physics of Fluids*, 5(3), March 1993.

[141] J.L. Wilkin, M.M. Bowen, and W.J. Emery. Mapping mesoscale currents by optimal interpolation of satellite radiometer and altimeter data. *Ocean Dynamics*, 52:95–103; doi: 10.1007/s10236–001–0011–2, 2002.